*J. Fluid Mech.* (2024), *vol*. 980, A56, doi:10.1017/jfm.2024.39

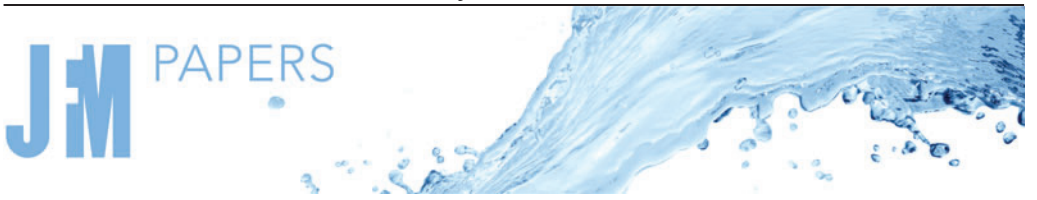


# Flow and aerodynamic noise control of a circular cylinder by local blowing

**Reza Maryami**[1], **Elias J.G. Arcondoulis**[1,2] **and Yu Liu**[1,3,†]

[1]Department of Mechanics and Aerospace Engineering, Southern University of Science and Technology, Shenzhen, Guangdong 518055, PR China

[2]School of Civil Aerospace and Design Engineering, University of Bristol, Bristol BS8 1TR, UK

[3]Guangdong Provincial Key Laboratory of Turbulence Research and Applications, Southern University of Science and Technology, Shenzhen, Guangdong 518055, PR China

(Received 24 March 2023; revised 10 October 2023; accepted 24 December 2023)

In this experimental study, the impact of symmetric local blowing on suppressing the vortex-induced noise of a circular cylinder was investigated. A highly instrumented cylinder with pressure taps and a series of blowing chambers was used to inject air along the span (seven times the cylinder diameter) at circumferential angles $\theta_b = \pm 41^\circ$, $\pm 90^\circ$ and $\pm 131^\circ$ corresponding to the boundary layer, shear layers on the cylinder and separated shear layers, respectively. The investigation aimed to understand the noise reduction mechanism of local blowing by conducting near-field pressure and far-field noise measurements in synchronisation with flow field velocity measurements. Near-field pressure was measured around the circumference of the cylinder using a remote-sensing technique and planar particle image velocimetry was implemented to measure the velocity of the wake flow field at a diameter-based Reynolds number of $Re = 7 \times 10^4$. The results revealed that the interaction of the rolling up separated shear layers, under the influence of high-momentum fluid travelling from the free stream to the wake, induced significant vertical flow movement in the vortex-formation region. This movement led to strong alternating surface pressure fluctuations at the cylinder's shoulders, contributing to the scattering of noise. It was demonstrated that local blowing delayed vortex shedding for all cases, except at $\theta_b = \pm 90^\circ$, which elongated the shear layers and pushed the high-momentum transfer area farther downstream. The application of local blowing at $\theta_b = \pm 41^\circ$ was particularly effective in increasing the vortex formation size due to reduced entrainment of fluid-bearing vorticity.

**Key words:** aeroacoustics, vortex shedding

† Email address for correspondence: liuy@sustech.edu.cn

## 1. Introduction

A circular cylinder placed in uniform flow generates vortex shedding (Roshko 1955), which can cause serious structural vibrations, an aerodynamic noise (i.e. Aeolian tone) and unsteady lift and mean drag forces (Strouhal 1878; von Kármán 1912; Curle 1955; Etkin, Korbacher & Keefe 1957). These phenomena are exhibited in many engineering applications such as cylindrical sections of high-speed train pantographs, wind turbine pylons, aircraft landing gears, electrical power lines and long-span cable-stayed bridges. Regardless of whether the incident flow is laminar or turbulent, novel and efficient flow control methods were developed to alleviate the vortex shedding of cylindrical bodies. As reviewed by Zdravkovich (1981) and Choi, Jeon & Kim (2008), the flow control methods can be divided into active and passive categories. Generally, active techniques can offer superior performance to passive methods, but energy input is needed to sustain efficient operation (Hartwich *et al.* 2014). Active techniques are controllable for manipulating dynamic and complex processes during system operation. Rashidi, Hayatdavoodi & Esfahani (2016) and Chen *et al.* (2022) have given a comprehensive review of many types of cylinder active flow control techniques: synthetic jets, electromagnetic forcing, rotation, forced oscillation, thermal effects, acoustic excitation, moving surfaces, feedback control strategies and suction/blowing (the latter is the focus of this study).

The use of air blowing to effectively control the boundary layer separation and wake of the cylinder has been ongoing for over a hundred years. As early as 1904, Prandtl used steady blowing to modify the boundary layer of a circular cylinder (Schlichting & Gersten 2003). Blowing-based control schemes have been widely adopted as spatially continuous blowing (CB) and localised blowing (LB). While the application of CB may be limited to air sources in some situations and not a promising flow control method in terms of energy consumption in comparison with LB, its effects on wake dynamics, mean drag and lift fluctuations, and even aerodynamic noise, is worth investigating. For example, in a numerical study, Mathelin, Bataille & Lallemand (2002) observed that CB through the whole surface of a cylinder within the Reynolds number range of $Re = 20$–$3900$ has a tendency to increase the boundary layer thickness, promote its separation and decrease the vortex-shedding frequency and the viscous drag induced. Following this idea, Angland, Zhang & Goodyer (2012) implemented experimentally CB through the surface of a cylinder upstream of an H-beam to reduce the interaction noise for the Reynolds number between $Re = 1.4 \times 10^5$ and $2.7 \times 10^5$. They showed a tonal noise reduction of 9.2 dB at a Strouhal number $St \approx 0.2$ and a broadband noise reduction of 3 dB averaged over the range of $St = 0.05$–$5$. The use of CB through a porous-coated cylinder was also investigated by Fransson, Konieczny & Alfredsson (2004) and more recently Guo *et al.* (2022) who demonstrated that the recirculation region is enlarged and pushed downstream. The Reynolds number in these experiments was $Re = 8500$ and $10^4$, respectively. Fransson *et al.* (2004) argued that the increase in vortex formation size may be directly coupled to the forward motion of the separation point. In addition, turbulence intensity decreases especially close to the cylinder, which may be due to the increase in the size of large-scale vortices and thus less mixing near the cylinder, or alternatively due to the low-velocity fluid through the surface. As a means to effectively suppress vortex-induced vibrations of a circular cylinder, Dong, Triantafyllou & Karniadakis (2008) employed continuous suction on the windward side and CB on the leeward side of the cylinder. Their study focused on two Reynolds numbers, specifically $Re = 500$ and 1000. The findings revealed that the controlled wake generally exhibited a reduction in structures compared with the uncontrolled case. Furthermore, it was observed that the streamwise braids in the near wake were significantly diminished and appeared to cluster at specific spanwise locations.

Among many possibilities to control the near-wake structure of the bluff body by steady or unsteady LB, fluid injection from the base of the body has attracted attention over the years. The application of this type of blowing is commonly associated with flow–structure interaction, and its effects were extensively studied in the pioneering experimental work by Wood (1964, 1967) and Bearman (1967). These researchers introduced the concept of base blowing, which involved modifying the wake of a two-dimensional (2-D) bluff body with a blunt trailing edge. Through their experiments, they demonstrated that substantial modifications could be achieved in the wake characteristics by employing base blowing. Wong (1985) investigated the effect of base blowing on a cylinder over a range of Reynolds numbers from $Re = 2000$ to 3000 by applying blowing through slits extending along the span at a position 180° from the front stagnation point. They found that this blowing configuration significantly reduces the flow-induced oscillations. The use of base blowing was also studied by Williams & Amato (1989) who employed pulsating jets through closely spaced, very small holes along the base of the cylinder at $Re = 370$. Their findings demonstrated that this technique has the capability to suppress vortex shedding and reduce the primary momentum deficit in the wake. In 2-D numerical simulation of a blowing applied at the base of a cylinder, Delaunay & Kaiktsis (2001) also observed that even a small amount of blowing can stabilise the wake by reducing backflow, specifically for Reynolds numbers greater than 47. Although base blowing has been shown to induce a change in the large-scale wake structure, the underlying reasons for this alteration remain unclear. In a recent study conducted by Deng *et al.* (2021), it was demonstrated that symmetric jet vortices, produced through a slot installed at the base of the cylinder, interact with the separated shear layers at a Reynolds number of $Re = 2.17 \times 10^4$. The occurrence of these vortices in the wake of the cylinder was also observed in previous studies by Gao *et al.* (2019) and Gao *et al.* (2021) at the Reynolds numbers of $Re = 3.33 \times 10^4$ and $1.67 \times 10^4$, respectively. These studies utilised a technique similar to the one introduced by Dong *et al.* (2008), where suction and blowing were applied simultaneously at the front and rear stagnation points, respectively. The reported dynamical interactions between the blowing vortices and shear layers result in the stretching of the shear layers, causing the alternating vortex shedding to occur farther downstream. This phenomenon is consistent with a reduction in sectional drag and the amplitudes of fluctuating dynamic loads on the cylinder.

However, the precise process by which the interaction between the blowing vortices and shear layers leads to their elongation along the streamwise direction is still not fully understood. Additionally, while the mechanism described above explains the suppression of near-wake instabilities, particularly when base blowing is applied through a slot with a short spanwise length of one cylinder diameter, $D$ (m), as noted by Deng *et al.* (2021) or a small number of holes distributed over $3D$ (Gao *et al.* 2019), it may not be sufficient to explain how base blowing can effectively control global instabilities. It is well known that vortex shedding is a result of temporal global instability (Provansal, Mathis & Boyer 1987; Sreenivasan, Strykowski & Olinger 1987). Chomaz, Huerre & Redekopp (1988) demonstrated that the presence of an absolute instability is necessary but not sufficient for self-sustained oscillations. A sufficiently large region of absolute instability is required for the global instability that leads to self-sustained oscillations. This understanding aligns with Norberg (2003), where it was demonstrated that the spanwise correlation length of a circular cylinder decreases approximately from $12D$ to $1.5D$ as the Reynolds number increases from $Re \approx 300$ to $3 \times 10^5$. Williams, Mansy & Amato (1992) reported that it is difficult to determine precisely how blowing interacts with near-wake structures because the forcing field affects a large region of the flow. In addition, when attenuation occurs under the influence of blowing, it expands along the span (Lin, Towfighi &

Rockwell 1995). Therefore, further research is necessary to comprehensively understand the main mechanism of blowing when applied over a large span length of the cylinder.

A better understanding of the wake oscillation mechanism can be obtained by introducing disturbances at specific, well-defined locations. According to Williams *et al.* (1992), the mode of the near-wake vortex formation at Reynolds numbers of $Re = 470$ can be substantially altered by the proper development of unsteady blowing or suction through two spanwise rows of holes located upstream of the boundary layer separation at $\pm 45^\circ$. A computational study of the feedback control of vortex shedding behind a circular cylinder was undertaken by Park, Ladd & Hendricks (1994). The control actuators were a pair of blowing/suction slots located at $\pm 50^\circ$, $\pm 65^\circ$ and $\pm 110^\circ$ asymmetrically with respect to the centreline to control the vortex shedding mode which is antisymmetrical. With the actuators at $\pm 50^\circ$ and $\pm 65^\circ$, vortex shedding suppression was not obtained yet a complete suppression of parallel vortex shedding was achieved for slots at $\pm 110^\circ$ slightly ahead of the separation points of the unforced wake. It should be noted that the vortex shedding suppression was reported only when the Reynolds number ($Re = 60$) is approximately 27 % higher than the critical Reynolds number for the onset of vortex shedding ($Re = 47$). At $Re = 80$, it was shown that the complete suppression of vortex shedding does not occur. Kim & Choi (2005) also studied a forcing scheme numerically at $Re = 100$ for cylinder drag reduction by blowing or suction of fluid through two slits with locations from $\pm 45^\circ$ to $\pm 135^\circ$. It was observed that the in-phase forcing produces the maximum phase mismatch at $\pm 90^\circ$ along the spanwise direction in the vortex shedding, weakens the strength of vortical structures in the wake, and thus reduces the drag. In a recent study (Wu & Choi 2021), steady and periodic LB was applied near the separation point ($\pm 90^\circ$) of a circular cylinder at $Re = 2.1 \times 10^4$ using either a slit (uniform blowing) or holes (discrete blowing) along the spanwise direction. The findings revealed that steady discrete blowing significantly reduced drag compared with steady uniform blowing. The optimal discrete blowing configuration induced counter-rotating vortices, transforming Kármán vortex cores into weakened three-dimensional (3-D) vortices.

As reviewed above, the use of air blowing has equally important ramifications in the areas of aerodynamic noise, vortex-induced vibrations and unsteady forces acting on the cylinder. Blowing was proved to strongly affect the boundary layers, increasing their thickness and lowering the dynamic gradient by injecting some low-momentum fluid (Mathelin *et al.* 2002; Fransson *et al.* 2004). In addition, blowing has an impact on the near-wake instabilities by pushing the vortex-formation region farther downstream (Fransson *et al.* 2004; Guo *et al.* 2022), yet it was unclear how LB acts to enlarge the vortex formation region when it is applied along the entire span of the cylinder. Previous studies have been limited in terms of a short spanwise length, which leads to 3-D flow effects from the blowing section ends. The circumferential location of LB is a critical factor for vortex shedding suppression. The LB was found to be inefficient in terms of flow control when blowing is provided too far away from the cylinder separation point (Park *et al.* 1994; Kim & Choi 2005). Employing asymmetric blowing configurations as emphasised in these earlier studies, might not be optimal for efficiently suppressing vortex shedding and mitigating lift fluctuations and acoustic noise. In addition, most studies have been carried out at low Reynolds numbers that bear little aeroacoustic relevance. Hence, much work is needed to understand the impact of symmetric LB applied to the boundary and/or separated shear layer on wake dynamics and the resultant Aeolian tone at high Reynolds numbers. By varying the circumferential angle at which LB is applied over an extensive spanwise length, the vortex shedding mechanism can be elucidated and the LB

angle that has the greatest potential to reduce the adverse effect of vortex shedding can be determined.

The near-field pressure in flow around a circular cylinder is affected by the vortex roll-up (Norberg 1986; Casalino & Jacob 2003; Oguma, Yamagata & Fujisawa 2013) and vortex shedding is the main mechanism of far-field noise (Strouhal 1878; von Kármán 1912; Curle 1955). In addition, the interaction between blowing and the vortex formation mechanism primarily occurs on the surface of the cylinder (Williams *et al.* 1992). Therefore, it is essential to analyse the correlation between near-field pressure, far-field noise and the hydrodynamic velocity field in the wake to gain a comprehensive understanding of the noise reduction mechanism associated with air blowing. To date, no experimental studies have provided this information that correlates near-field pressure suppression with far-field noise reduction, which results in a gap in the literature. The primary objective of this comprehensive experimental study is to bridge this research gap by conducting simultaneous measurements of surface pressure fluctuations, far-field noise and velocity fields in the wake. To achieve this, a circular cylinder equipped with remote-sensing pressure taps was utilised to measure pressure fluctuations on the cylinder surface. These measurements were synchronised with far-field noise measurements and particle image velocimetry (PIV) measurements of the flow field. Notably, to the best of the authors' knowledge, no similar experimental studies have been conducted to investigate cylinder wake flows, with or without LB, while simultaneously capturing these three essential field measurements.

This paper is organised as follows. The cylinder and LB system design, remote-sensing method and PIV set-up are presented in § 2. The effects of LB on far-field noise and near-field pressure are discussed in § 3. A detailed analysis of wake development and coherence studies are discussed in § 4. A proposed explanation of the vortex shedding process is provided in § 5, and is related to previous results of aeroacoustic and flow field to explain the noise reduction mechanism. Finally, § 6 concludes the paper and summarises our findings concerning the application of LB for aerodynamic and aeroacoustic applications.

## 2. Experimental set-up

### 2.1. *Wind tunnel and test section*

The measurements were carried out in a low-speed, open-jet anechoic wind tunnel at the Southern University of Science and Technology (SUSTech) (Yang *et al.* 2021), as shown in figure 1(*a*). The closed-loop wind tunnel has a rectangular cross-section nozzle with a width of 600 mm and a height of 550 mm. The inner dimensions of the anechoic chamber are $3.8\,\mathrm{m} \times 5.7\,\mathrm{m} \times 3\,\mathrm{m}$ and the walls are covered with a broadband compact absorber with a thickness of 35 mm to achieve anechoic performance for frequencies greater than 100 Hz at a distance of 1.9 m from the centre of the test section. The wind tunnel is capable of producing flow speeds up to $70\,\mathrm{m\,s^{-1}}$ with an incoming flow turbulence intensity of 0.15 %. The background noise level is 76 dBA at $70\,\mathrm{m\,s^{-1}}$, which was measured 1.5 m away from the wind tunnel centreline. The test section involving parallel endplates, i.e. the top and bottom laser-cut plates attached to the nozzle exit, has a length of 800 mm and the alignment of the rectangular endplates helps to maintain a nearly 2-D flow over the cylinder. According to the coordinate system with an origin located at the midspan of the cylinder, the nozzle exit is located at $x = -300$ mm. Therefore, the cylinder was properly placed within the potential core of the nozzle jet flow.

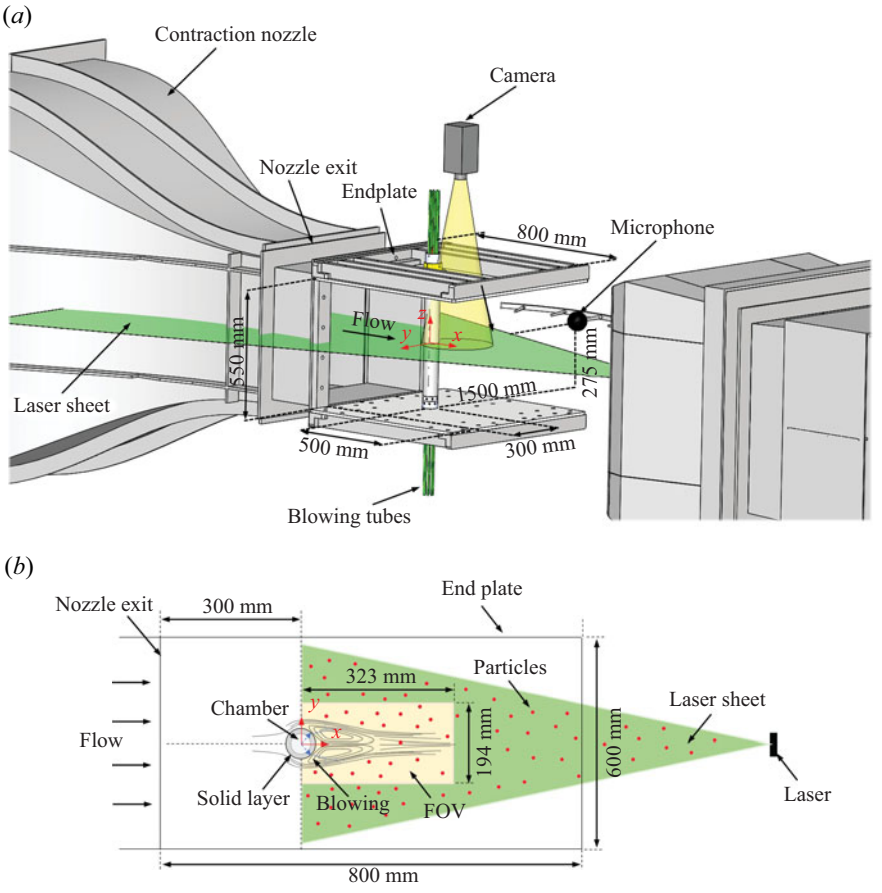


Figure 1. Schematic diagram depicting (*a*) the experimental set-up with a cylinder in the aeroacoustic wind tunnel and (*b*) the top view of the planar PIV configuration.

### 2.2. *Cylinder design*

A cylinder model with an outer diameter of $D = 64.7$ mm and a span of $L = 550$ mm was designed. The cylinder was composed of three different parts along its span, consisting of one middle section with pressure taps and chamber instrumentation and two side extension parts, as depicted in figure 2(*a*). Several factors were considered to determine the suitable value of the outer diameter of the cylinder. The limiting factors were the blockage ratio, aspect ratio and the effects of low-frequency background noise. By considering the outer diameter of 64.7 mm, the blockage was found to be less than 12 %. The cylinder had an aspect ratio of approximately 8.5, which indicates that any influence from the endplates can be ignored (Zdravkovich 1981).

By considering a balance between low background noise and high vortex-shedding frequency, the incoming flow velocity was set at $U_\infty = 20\,\mathrm{m\,s^{-1}}$, corresponding to $Re = 7 \times 10^4$. To assist the explanation of the cylinder design process, the $St = fD/U_\infty$ relationship is provided, where $f$ (Hz) is vortex shedding tonal frequency. If it is assumed that $St \approx 0.19$ for the anticipated Reynolds number range of a circular cylinder (Norberg 2003) then $f \approx 59$ Hz at $U_\infty = 20\,\mathrm{m\,s^{-1}}$ should be observed. From a previous experiment (Maryami *et al.* 2023*c*) conducted in the same wind tunnel at SUSTech in a flow speed

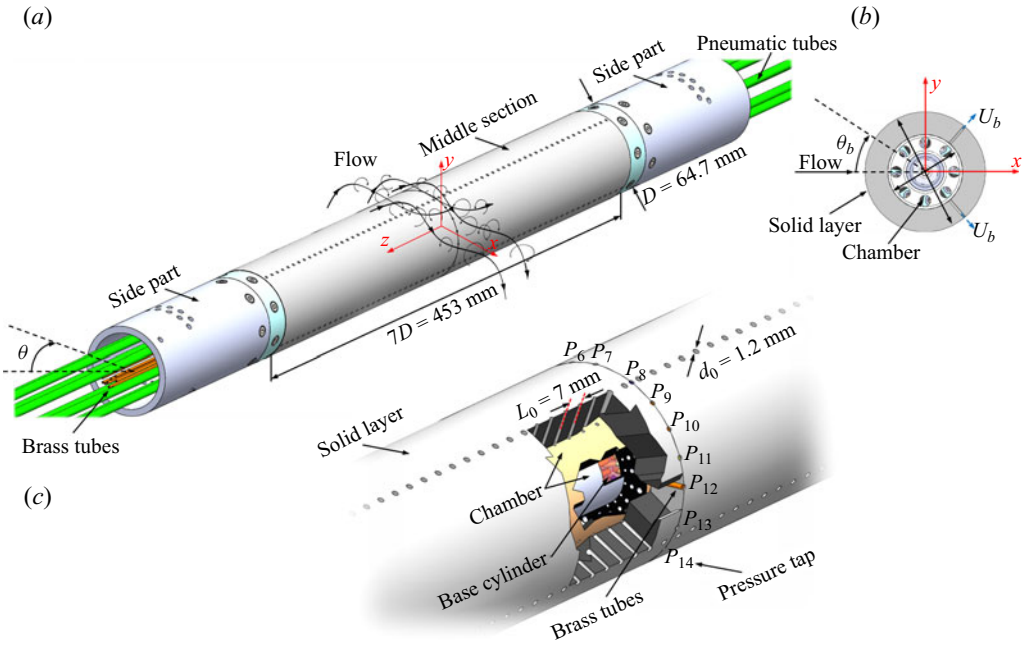


Figure 2. (*a*) Schematic of the cylinder design, (*b*) the *xy*-plane of the cylinder and (*c*) the sensing area on the cylinder equipped with pressure taps, $P_i$ ($i = 1 : 20$), distributed around the circumference of the cylinder at midspan. Note that only pressure taps $P_6$ to $P_{14}$ are visible in this diagram. The peripheral locations of all 20 pressure taps are listed in table 2.

range of $U_\infty = 15$–$50\,\mathrm{m\,s^{-1}}$, vortex shedding tones from the cylinder at this frequency typically protrude above the background noise by at least 10 dB. Note that the Reynolds number considered here is matched to the subcritical regime (Roshko 1955; Achenbach 1968), which is the flow conditions of typical aeroacoustic applications as stated in § 1. In addition, the PIV measurements at $U > 30\,\mathrm{m\,s^{-1}}$ are not recommended due to difficulties in stabilising the flow field. Therefore, the specific flow velocity of $U_\infty = 20\,\mathrm{m\,s^{-1}}$ was strategically selected to achieve an optimal particle seeding density, an accurate and reliable tracking of the particles within the fluid, and hence robust data of flow velocity.

The middle section of the cylinder was coated with a series of solid layers (cylinders with inner and outer diameters of $d = 40$ mm and $D = 64.7$ mm, respectively, see figure 2*b*) containing holes with a diameter of $d_0 = 1.2$ mm to allow distributed LB to be applied through the surface of the cylinder as shown in figure 2(*c*). In this experimental study, LB was implemented at circumferential angles of $\theta_b = \pm 41^\circ$, $\pm 90^\circ$ and $\pm 131^\circ$ in an open-loop control configuration. These cases are denoted as LB41, LB90 and LB131, respectively, representing the application of LB in the boundary layer, shear layers on the cylinder, and separated shear layers, respectively. Hence, the LB holes with a spanwise spacing of $L_0 = 7$ mm were distributed along two lines: one positioned on the top half and the other on the bottom half of the cylinder. The experimental data provided in the literature show that the spanwise correlation length of a circular cylinder extends to approximately $3.3D$ at $Re \approx 7 \times 10^4$ (Norberg 2003), yet there is a lack of fidelity experimental or numerical data to determine this length in the case of LB at a specific Reynolds number and air flow rate. Therefore, a total of 64 blowing holes were evenly

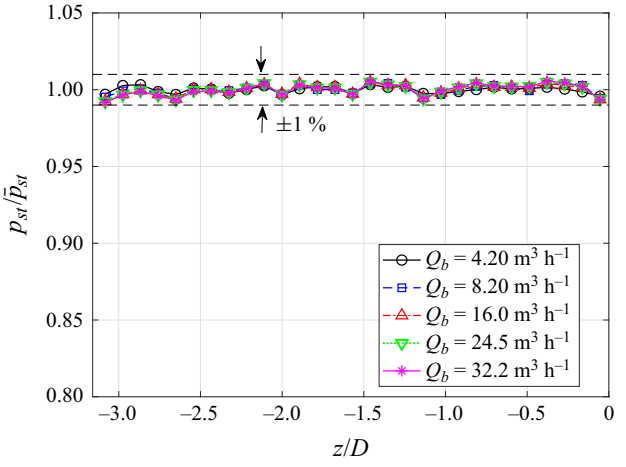


Figure 3. Static pressure, $p_{st}$, distribution along the half-span of the chamber normalised by the mean static pressure, $\bar{p}_{st}$, in the case of LB90.

distributed along each line, covering a span length of 7$D$, to ensure the development of a sufficient 3-D flow field along the cylinder span.

### 2.3. *Chamber design*

In the present study, the air supply system was composed of three main components: an air supply device (compressor), air preparation equipment (air filter, regulator, pressure gauge and flow meter) and an air flow chamber. All these components except the airflow chamber were located outside the anechoic chamber. Three 3-D printed chambers were designed similar to Maryami *et al.* (2022*b*); Maryami, Arcondoulis & Liu (2023*a*,*b*). Each chamber was installed firmly in the corresponding solid layer as shown in figure 2(*b*), so that the blowing holes of the chamber were aligned properly with those of the solid layer. The chamber was further divided at the half-span of the cylinder to allow for remote-sensing pressure taps to be embedded at the midspan. Therefore, LB was applied to both sides of the chamber, where each side was fed by eight inlets for tube connections (see figure 2*a*). The design of a series of chambers ensured a more uniform distribution of LB along the span. To check the uniformity of LB along the span, the static pressure distribution was measured through a total of 32 steel tubes with inner and outer diameters of 0.5 and 1 mm, respectively, inserted into the blowing holes of the test chamber. The steel tubes were connected to two 16-channel Model 9116 intelligent pressure scanners with a full-scale pressure range from 2.5 kPa to 5200 kPa by flexible tubes with an inner diameter of 0.5 mm and an outer diameter of 2 mm. The results showed that the pressure along the chamber span is nearly constant within ±0.1 % as presented in figure 3.

The LB flow rate was measured by a mass flow meter and was kept constant by using a regulator and pressure gauge. The equivalent momentum coefficient, $C_\mu$, which is the ratio of LB momentum flux at each hole to incoming flow momentum flux, was used to facilitate the research (Lin *et al.* 1995; Chen, Li & Hu 2014; Gao *et al.* 2019; Deng *et al.* 2021; Maryami *et al.* 2022*b*, 2023*a*,*b*) and is defined as follows:

$$C_\mu = \left(\frac{U_b}{U_\infty}\right)^2 \times \left(\frac{A_b}{DL_0}\right), \tag{2.1}$$

| $Q_b(\mathrm{m^3\,h^{-1}})$ | $U_b/U_\infty$ | $C_\mu$ |
|---|---|---|
| 12 | 1.15 | 0.007 |
| 20 | 1.90 | 0.018 |
| 28 | 2.70 | 0.036 |

Table 1. Blowing flow rate, $Q_b$, velocity ratio, $U_b/U_\infty$ and corresponding $C_\mu$ values calculated using (2.1).

where $U_b$ ($\mathrm{m\,s^{-1}}$) is the average LB velocity of each hole, $L_0$ (m) is the spanwise spacing between two neighbouring LB holes, and $A_b$ ($\mathrm{m^2}$) refers to the combined area of the two blowing holes, one located on the top side and the other on the bottom side of the cylinder. The experiments were also carried out for three air flow rates of $Q_b = 12$, 20 and $28\,\mathrm{m^3\,h^{-1}}$. The $Q_b$, $U_b/U_\infty$, and corresponding $C_\mu$ values of LB cases are presented in table 1. Please note that significant tonal noise reduction was achieved for all $C_\mu$ values within this $Q_b$ range. However, in this study, only the case with $C_\mu \approx 0.007$ ($Q_b = 12\,\mathrm{m^3\,h^{-1}}$) was specifically presented as it serves as an indicative example for all the investigated cases.

### 2.4. *Near-field pressure and acoustic measurements*

Near-field pressure measurements were performed using a remote-sensing technique and pressure taps installed in the middle section of the cylinder. The cylinder was equipped with 20 pressure taps distributed with non-uniform angular spacing as shown in figure 2(*c*) and their peripheral locations are summarised in table 2. The pressure taps are comprised of a brass tube with inner and outer diameters of 0.8 mm and 1.6 mm, respectively, fitted in a designated housing on the solid-layer surface. As shown in figure 4(*a*), the brass tubes were connected to the remote-sensing probes using brass and flexible polyurethane tubing with inner and outer diameters of 0.8 and 4 mm, respectively, similar to that used by Maryami *et al.* (2023*c*). Each remote probe consists of a microphone holder and a Panasonic WM-61A microphone with a circular sensing diameter of 2 mm attached to a pinhole with a diameter of 0.4 mm (see figure 4*b*). An extension tube of 2 m was connected to the microphone-holder brass tube to eliminate the spurious tones related to the standing waves in the flexible tubing. Panasonic WM-61A microphones have been used by many (Angland *et al.* 2012; Maryami *et al.* 2019, 2020; Vemuri *et al.* 2020; Maryami *et al.* 2022*a*, 2023*c*,*d*) to produce reliable pressure data over the frequency range of interest ($20\,\mathrm{Hz} \leq f \leq 10\,\mathrm{kHz}$).

*In situ* calibration was carried out for the remote-sensing probes to compensate for any possible amplitude damping within the small tubes and the lag produced by the remote probe extensions. A tube with a length of 110 mm and a diameter of 10 mm along with a cone connected to a high-quality loudspeaker was used for the calibration similar to Maryami *et al.* (2019). The reference microphone was a 1/2 inch Brüel & Kjær (B&K) free-field microphone Type 4966 that was calibrated using a B&K calibrator Type 4231. A transfer function between the remote and reference microphones was obtained using a white noise signal, following the procedure of Mish (2001). The coherence values between these pressure signals were smooth and near one for frequencies less than or equal to approximately 6 kHz. Note that this frequency corresponds to $St \approx 19.5$ at $U_\infty = 20\,\mathrm{m\,s^{-1}}$, which is sufficiently high for the frequency range of interest in this experimental investigation and is similar to the upper-frequency range of others (Garcia-Sagrado & Hynes 2011; Gruber 2012).

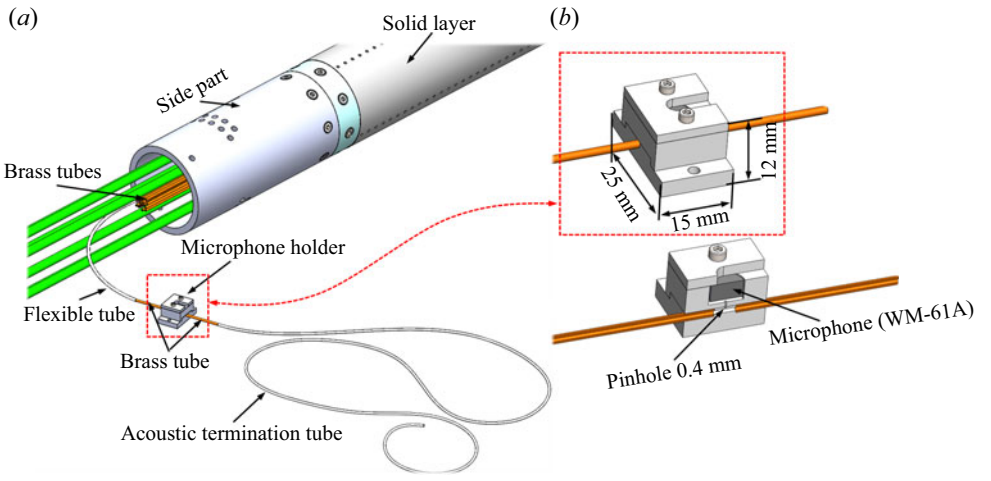


Figure 4. Schematic of the remote-sensing set-up for (*a*) the full view of the cylinder and (*b*) assembly view of the remote-sensing holder.

| Pressure taps | $\theta$ (deg.) | Pressure taps | $\theta$ (deg.) |
|---|---|---|---|
| $P_1$ | 0 | $P_{11}$ | 180 |
| $P_2$ | 17 | $P_{12}$ | −164 |
| $P_3$ | 41 | $P_{13}$ | −131 |
| $P_4$ | 57 | $P_{14}$ | −123 |
| $P_5$ | 74 | $P_{15}$ | −107 |
| $P_6$ | 90 | $P_{16}$ | −90 |
| $P_7$ | 107 | $P_{17}$ | −74 |
| $P_8$ | 131 | $P_{18}$ | −41 |
| $P_9$ | 147 | $P_{19}$ | −33 |
| $P_{10}$ | 164 | $P_{20}$ | −17 |

Table 2. Peripheral positions of the pressure taps, $P_i$ ($i = 1 : 20$), at $z/D = 0$.

The far-field noise was measured using a B&K free-field Type 4966 microphone located perpendicular to the flow and a distance of 1.5 m away from the cylinder axis as shown in figure 1. A National Instruments (NI) PXI-10420 chassis with two 24-bit synchronised NI PXI-4496 data acquisition (DAQ) cards were used to measure near-field pressure and far-field noise simultaneously at a sampling frequency of 51.2 kHz over 10 s. To convert the pressure–time data into the frequency domain, a fast Fourier transformation with Hamming windowing with 50 % overlap was used based on Welch's method, resulting in a frequency resolution of 2 Hz. These data were then converted into a power spectral density (PSD), namely $\phi_{pp,s}$ and $\phi_{pp}$ (dB Hz$^{-1}$) for near-field pressure and far-field noise, respectively, using a reference pressure of $p_0 = 20\,\mu$Pa.

### 2.5. *The PIV set-up*

Time-resolved planar PIV experiments were conducted in the leeward region of the cylinder and in the near wake, where the vortex shedding occurs and is generally accepted to constitute the sound source. The field of view (FOV) (approximately $32 \times 19\,\text{cm}^2$) covers the flow field with dimensions of $5D \times 3D$ in the $x$- and $y$-directions, respectively,

as shown in figure 1(*b*). The air in the tunnel was seeded with dioctyl sebacate particles with a mean diameter of 1 μm and illumination was provided by a Photonics Nd: YAG laser (50 mJ @ 10 kHz). The light sheet was directed from the wake towards the cylinder, facilitating particle illumination on both the top and bottom sides of the centreline. A Phantom VEO410L (1280 × 780 pixels, 12 bit, pixel pitch 20 μm, maximum frame rate 5.2 kHz) equipped with a Nikon Micro-Nikkor 60 mm objective was used at a focal ratio of $f/2.8$. Synchronisation of the laser pulses and image acquisition was accomplished using a LaVision programmable timing unit in combination with the LaVision DaVis 10.0 software package. Image pairs were acquired at a sampling frequency of 2.645 kHz over a duration of 2 s. All 5289 images were processed using an iterative multipass technique with a final window size of 32 × 32 pixels and an overlap factor of 75 %. To address the issue of surface reflections in the PIV process the cylinder surface was painted black and the angle of incidence of the laser light was adjusted to optimise the illumination of the flow. By carefully selecting this angle, the amount of light that was directly reflected into the camera was minimised, resulting in an improved image quality for PIV analysis.

The transistor–transistor logic signal from the Q-switch of the first laser was recorded simultaneously with the microphone signal to synchronise the PIV with the microphone measurements. Henning *et al.* (2008) reported that the leading edge of the transistor–transistor logic signal corresponds to the firing of the laser pulse and hence provides the time of the captured velocity field snapshot. The Q-switch signal was acquired with the same DAQ system as the microphone signal (NI PXI-4496), also sampled with a rate of 51.2 kHz. The NI PXI-4496 DAQ was also triggered by the programmable timing unit to ensure synchronous measurements of the PIV system and pressure data. As the PIV and pressure signals have different lengths and sampling rates, an antialiasing (low-pass) finite impulse response filter was used to resample the signals with the lower sampling rate during the resampling process. To compensate for any delay, the signals were aligned by the earliest signal.

## 3. Aeroacoustic characteristics

### 3.1. *Far-field noise spectra*

Far-field acoustic PSD, $\Phi_{pp}$ (dB Hz$^{-1}$), as a function of $St$ for each cylinder is presented in figure 5 and is calculated from

$$\Phi_{pp} = 10 \log_{10} \left( \frac{\phi_{pp}}{p_0^2} \right). \tag{3.1}$$

The results show the existence of a tonal peak at $St \approx 0.19$ for the baseline, which corresponds to the fundamental vortex shedding tone ($f_1$). This tonal peak falls within the published Strouhal number envelope for the tested Reynolds number according to Norberg (2003). The $f_1$-tone is also called the first harmonic, other harmonics with frequencies that are positive integer multiples of the fundamental frequency are known as higher harmonics ($f_2 = 2f_1, f_3 = 3f_1, f_4 = 4f_1, \ldots$). The results reveal that every LB case except LB90 is able to reduce the $f_1$-tone relative to the baseline. It is observed that LB41 possesses superior performance in terms of tonal noise reduction of 19 dB, yet presents an increase in broadband energy content beyond $St \approx 1$. The LB41 also shows the emergence of another vortex shedding peak at $St \approx 0.25$, indicating the existence of two types of vortical structures in the wake region. For LB90, an increase in both tonal and broadband energy contents is observed, indicating that the application of LB perpendicular to the free

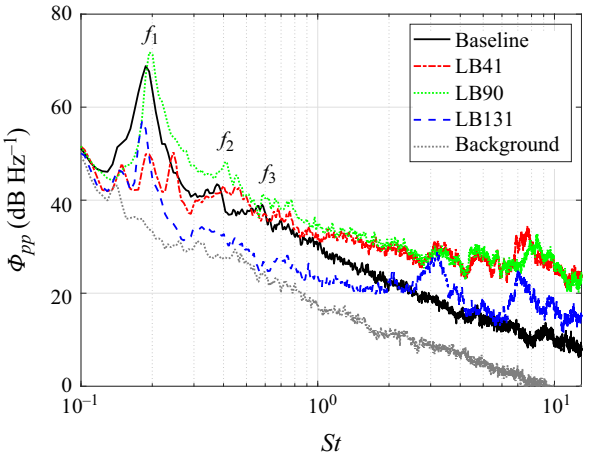


Figure 5. Acoustic PSD, $\Phi_{pp}$, plotted against $St$ for various LB cases. The labels $f_1$, $f_2$ and $f_3$ represent the fundamental vortex shedding tone (first harmonic), second and third harmonics, respectively.

stream near the boundary layer separation point, which is around 73.6° for the baseline as reported by Maryami *et al.* (2023*c*), promotes vortex shedding and is unfavourable to aerodynamic noise suppression. It is observed that LB131 reduces the $f_1$-tone by around 12 dB and reduces the broadband energy content within 8–10 dB up to $St \approx 2$. Note that the $f_1$-tone in the case of LB131 protrudes by approximately 23 dB above the broadband energy content, while this protrusion is of the order of 10 dB for LB41. It is observed that beyond $St \approx 2$, specifically within $St \approx 7$–9, broadband peaks are evident for all LB cases, which can potentially be attributed to the blowing self-noise phenomenon, as documented by Angland *et al.* (2012). It is difficult to determine which part of the blowing system (i.e. compressor, chamber or air jets) this noise may be linked to. Nonetheless, the ratio of vortex shedding noise to blowing self-noise is sufficiently high as reported by Guo *et al.* (2023) using the same air supply system at SUSTech and similar air flow rates. This finding is important in facilitating the study of the effects of LB on suppressing vortex shedding noise from a circular cylinder.

By integrating the far-field PSD over the whole frequency range of interest corresponding to $St \approx 0.13$–13, the overall sound pressure level (OASPL) is calculated as follows:

$$\mathrm{OASPL} = 10 \log_{10} \left( \frac{\int \phi_{pp} \, \mathrm{d}f}{p_0^2} \right), \tag{3.2}$$

and it is observed that the OASPL in the case of LB131 is lower in magnitude than that of LB41 by around 2.2 dB. Considering that the OASPL difference between LB41 and LB131 is not significant and the tonal noise is much more important in the case of bluff bodies, it can be argued that LB41 is still the better blowing method in terms of noise reduction.

### 3.2. *Near-field pressure spectra*

To gain further insights into the noise generation mechanism of the cylinder, the near-field pressure PSD, $\Phi_{pp,s}$ (dB Hz$^{-1}$), was calculated by (3.1) and the results at some angles, i.e. $\theta = 0°, 41°, 90°, 131°$ and 180°, are presented in figure 6. The $\Phi_{pp,s}$ spectra of the baseline show a dominant tonal peak at the $f_1$-tone frequency, consistent with the fundamental

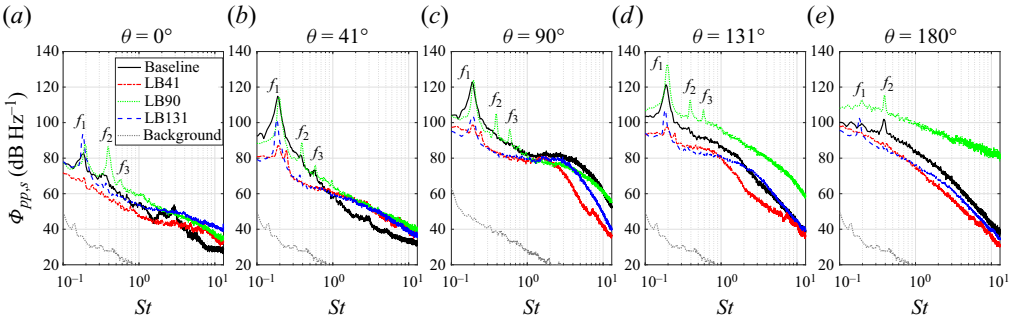


Figure 6. Near-field PSD, $\Phi_{pp,s}$, at $\theta = 0°$, 41°, 90°, 131° and 180°. The labels $f_1$, $f_2$ and $f_3$ represent the fundamental vortex shedding tone (first harmonic), second and third harmonics, respectively.

tone observed in figure 5. Therefore, the surface pressure fluctuations are clearly linked to vortex shedding and are responsible for sound source generation (Inoue & Hatakeyama 2002). Although the concept of the feedback signal (upstream influence) in the context of vortex shedding from a circular cylinder has already been observed in the experiments by Nishioka & Sato (1978) and Unal & Rockwell (1988); the precise mechanism by which vortex shedding affects the cylinder remains unclear. It is uncertain whether this effect is caused by the induced velocity field of the vortices or by upstream-travelling vorticity waves that originate from the initial global instability (Williams *et al.* 1992). In both cases, however, the vorticity dynamics in the wake modulates the boundary layer by providing initial spatiotemporal disturbances to the shear layers on the cylinder. These disturbances are then spatially amplified to a saturation level in the separated shear layers, leading to the formation of fully developed vortices in the wake region. These vortices produce a feedback signal to the cylinder, which influences the boundary layer and starts the cycle again.

The influence of vortex shedding on various peripheral locations around the cylinder, known as the feedback signal, is dependent on the distance between each location and the vortex formation region. As this distance increases, the strength of the feedback signal diminishes due to enhanced energy dissipation. This is further supported by the observations depicted in figure 6. It is observed that the $f_1$-tone (associated with lift fluctuations) with a magnitude of around 80 dB appears at $\theta = 0°$ and follows a gradually increasing trend with $\theta$ to reach a maximum of approximately 123 dB at $\theta = 90°$. This is because the distance between these measurement points and the vortex-formation region decreases, allowing for stronger interactions between the shed vortices and the nearby locations through feedback signal. For $\theta > 90°$ while the distance to the vortex-formation region continues to decrease with increasing $\theta$, the magnitude of the $f_1$-tone decreases until it becomes fully broadband at $\theta = 180°$. This difference can be attributed to the distinct roles played by surface pressure fluctuations on the leeward side of the cylinder compared with the windward side. Instead of contributing primarily to lift fluctuations, the surface pressure fluctuations on the leeward side of the cylinder have a greater impact on drag fluctuations, as will be depicted in figure 7. This shift in the characteristics of surface pressure fluctuations is evident in the magnitude of the $f_2$-tone, which increases as $\theta$ approaches 180° (Casalino & Jacob 2003; Maryami *et al.* 2019, 2020, 2022*a*, 2023*c*; Maryami & Ali 2023).

The variations in the size of the vortex-formation region influenced by local blowing cases have notable effects on the feedback signal and subsequently the near-field pressure

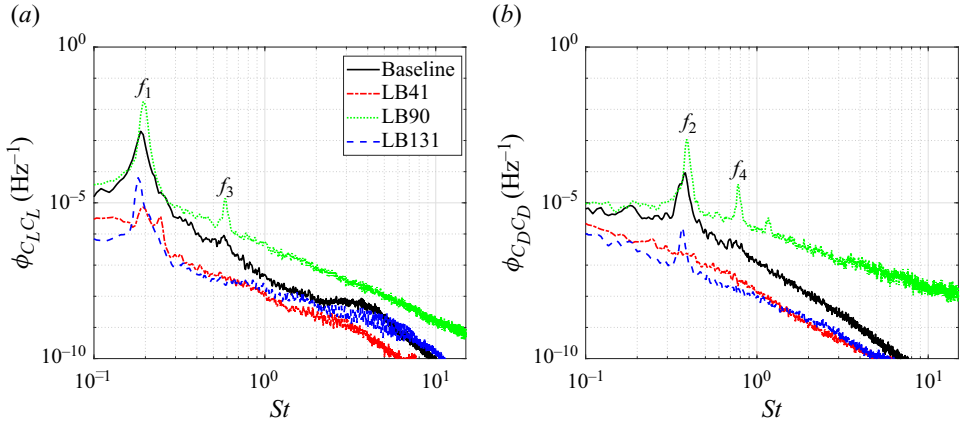


Figure 7. (*a*) Lift coefficient PSD, $\phi_{C_L C_L}$, and (*b*) drag coefficient PSD, $\phi_{C_D C_D}$, as a function of *St*. The labels $f_1$ and $f_3$ represent the odd harmonics, while $f_2$ and $f_4$ represent the even harmonics.

characteristics at the $f_1$- and $f_2$-tone frequencies. In the cases of LB41 and LB131, where the vortex formation region is larger compared with the baseline (refer to § 4), the near-field pressure at these frequencies becomes weaker in terms of energy content yet LB90 exhibits the opposite behaviour. This conclusion is generally valid, except in the case of LB131 at the stagnation point. Despite having a larger vortex-formation region similar to LB41, LB131 exhibits an increase of 11 dB in the magnitude of the $f_1$-tone from the baseline at the stagnation point. On the other hand, LB41 demonstrates a broadband behaviour at the $f_1$-tone frequency, suggesting a distinct vortex-shedding mechanism for LB131 compared with LB41 (refer to § 5.4). At $\theta = 0°$, LB90 reveals the $f_1$-tone with a magnitude of approximately 6 dB. In addition to the $f_1$-tone, the first two harmonics, i.e. the $f_2$- and $f_3$-tones, are observed for LB90 in which the even harmonic is stronger than the odd harmonic, indicating that LB90 increases drag fluctuations. It will be shown in figure 7 that lift and drag fluctuations occur at the odd $(f_1, f_3, \ldots)$ and even $(f_2, f_4, \ldots)$ harmonics, respectively, as documented by many (Etkin *et al.* 1957; Casalino & Jacob 2003; Qin 2004; Maryami *et al.* 2020, 2022*a*, 2023*c*; Maryami & Ali 2023).

Away from the stagnation point at $\theta = 41°$, 90° and 131° (see figure 6*b–d*), the $f_1$-tone appears for all LB cases and increases in magnitude with $\theta$, which is due to the shorter distance between these peripheral locations and the vortex-formation region. While LB41 shows the tonal peak of dual vortex shedding around the $f_1$-tone frequency as already observed in figure 5, it exhibits a remarkable reduction in the magnitude of the $f_1$-tone from the baseline, with a range of 23–30 dB, making it the most effective LB case. In contrast, LB90 demonstrates an increase in the magnitude of the $f_1$-tone compared with the baseline, reaching approximately 11 dB at $\theta = 131°$, indicating the presence of significant lift fluctuations. In the base region at $\theta = 180°$, as shown in figure 6(*e*), LB41 shows a broadband behaviour over the frequency range yet LB90 and LB131 present tonal peaks at the $f_2$- and $f_1$-tone frequencies, respectively, similar to the observations at $\theta = 0°$.

It is observed up to $\theta = 90°$ as shown in figure 6(*a–c*), that each LB displays a high broadband contribution at $St \gtrapprox 1$. For $\theta > 90°$, only LB90 increases the broadband energy content from that of the baseline. It can be argued that small-scale high-frequency fluctuations in the boundary layer that have moved up to the separation point contribute to the broadband components of the surface pressure. At $\theta = 41°$, it is notable that these structures appear to be independent of the size of the vortex-formation region.

Moreover, any external perturbation applied to the boundary layer (LB41), shear layer on the cylinder (LB90) or separated regions (LB131) does not contribute to an increase in their energy content. Beyond separation, the high-frequency broadband pressure spectrum is attributed to small-scale high-frequency fluctuations of turbulence in the near-wake region (Doolan 2009), whose energy content decreases with increasing vortex formation size.

### 3.3. *Lift and drag spectra*

In order to study how LB cases affect the unsteady forces, figure 7 presents the spectra of the lift and drag coefficients, i.e. $\phi_{C_LC_L}$ and $\phi_{C_DC_D}$ ($\mathrm{Hz}^{-1}$), respectively. The lift and drag spectra were calculated by integrating the surface pressure fluctuations around the circumference of the cylinder as done by others (Fage & Falkner 1931; Sadeh & Saharon 1982; Casalino & Jacob 2003; Norberg 2003; Maryami *et al.* 2020, 2022*a*, 2023*c*; Maryami & Ali 2023). Note that the contribution of the skin friction was neglected because it is less than 2 % of the total drag in the subcritical Reynolds number range (Fage & Falkner 1931; Achenbach 1968; Sadeh & Saharon 1982).

The results in figure 7 reveal dominant tonal peaks at the $f_1$- and $f_2$-tone frequencies in the $\phi_{C_LC_L}$ and $\phi_{C_DC_D}$ spectra, respectively, for the baseline, which is consistent with others (Casalino & Jacob 2003; Qin 2004; Maryami *et al.* 2020, 2022*a*, 2023*c*; Maryami & Ali 2023). The dominant tone frequency of $\phi_{C_DC_D}$ is twice that of $\phi_{C_LC_L}$, and thus the amplitude of fluctuating drag, which is significantly smaller than that of fluctuating lift (Bouak & Lemay 1998; Posdziech & Grundmann 2007), is dominated by fluctuating pressures that are in phase between the upper and lower sides of the cylinder. Interestingly, the dominant tonal peaks in the spectra of $\phi_{C_LC_L}$ and $\phi_{C_DC_D}$ are similar to those of the near-field spectra at $\theta = 90^\circ$ and $180^\circ$, respectively, (compare figures 6*c* and 6*e* with figures 7*a* and 7*b*, respectively). These observations are consistent with previous findings (Casalino & Jacob 2003; Maryami *et al.* 2020, 2022*a*, 2023*c*; Maryami & Ali 2023) and demonstrate that the alternating pressure fluctuations at the shoulders of the cylinder are lift fluctuations sources (Gerrard 1966), whose energy is concentrated to a band around the fundamental vortex-shedding frequency (Gerrard 1961; Ferguson & Parkinson 1967). The dominant sound correlates with the fundamental frequency of lift fluctuations in a dipole pattern with a dipole axis normal to the free stream (Gerrard 1955; Etkin, Korbacher & Keefe 1956).

Each LB case exhibits tonal peak characteristics similar to the baseline. Specifically, LB90 demonstrates odd harmonics ($f_1$ and $f_3$) and even harmonics ($f_2$ and $f_4$) in the $\phi_{C_LC_L}$ and $\phi_{C_DC_D}$ spectra, respectively, with magnitudes exceeding those of the baseline. The significant fluctuations in lift and drag are attributed to the presence of strong vortex shedding, characterised by closely rolling up shear layers near the cylinder and exhibiting a notable spanwise correlation (Norberg 2003). In contrast, LB41 shows the superior reduction; the double $f_1$-tone in the $\phi_{C_LC_L}$ spectrum in line with the near- and far-field pressures (see figures 5 and 6, respectively), is reduced by at least two orders of magnitude relative to the baseline. In addition, the $\phi_{C_DC_D}$ spectrum is quite broadband over the frequency range.

## 4. Wake flow field

### 4.1. *Time-averaged flow fields*

Contour plots of the normalised time-averaged $x$- and $y$-components of velocity, $\bar{u}/U_\infty$ and $\bar{v}/U_\infty$, respectively, are presented in figure 8. The baseline shows the emergence

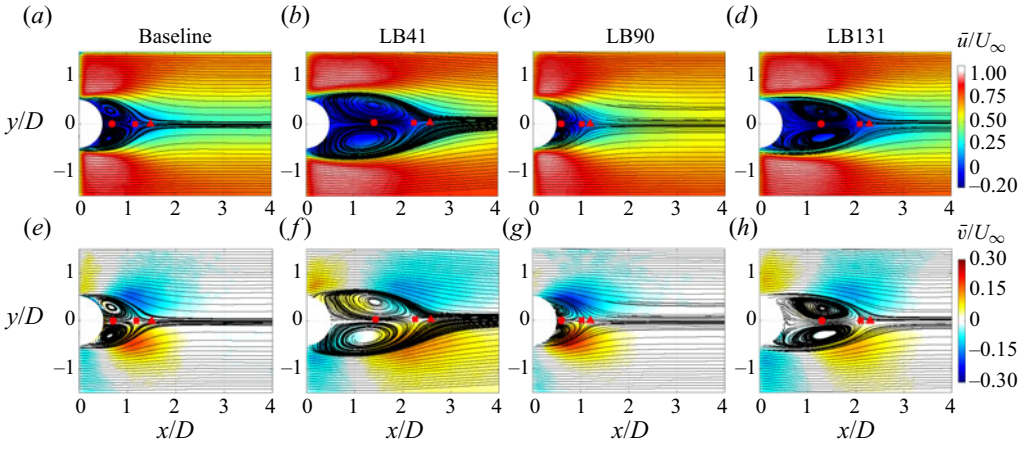


Figure 8. Normalised time-averaged $x$-and $y$-components of velocity, (*a–d*) $\bar{u}/U_\infty$ and (*e–h*) $\bar{v}/U_\infty$, respectively, superimposed by the time-averaged streamline. The solid red circle, square and triangle symbols represent the vortex core centre at $x \approx L_{vc}$, the end of the recirculation region at $x \approx L_r$ (saddle point) and the end of the vortex-formation region at $x \approx L_f$, respectively. The white contour region in $\bar{u}/U_\infty$ shows the flow acceleration area (FAA).

of a pair of counter-rotating vortices close to the base of the cylinder with an identical symmetric vortex core structure with respect to the centreline ($y/D = 0$). Vortex structures are evident in each LB case, indicating that none of the LB techniques investigated in this study are able to completely suppress the generation mechanism of vortex shedding. Despite this, some LB cases are more capable of expanding or shifting the recirculation region downstream in comparison with the baseline. The observations indicate that LB41 enables the shear layers to extend farther downstream before rolling up, resulting in a larger vortex-formation region. In contrast, LB90 reduces the size of the vortex-formation region compared with the baseline, suggesting an acceleration in the rolling up of the shear layers into the wake. The time-averaged flow fields along with the observations in figures 5–7 reveal that a delay in vortex shedding induces a weak near-field pressure with low-energy lift oscillations at the $f_1$-tone frequency and then a superior tonal noise reduction. A similar observation was made by Sueki *et al.* (2010) and Showkat Ali, Mahdi & Da Silva (2020) who demonstrated that a delay in flow recirculation using porous media as a form of passive flow control gives rise to more stable shear layers (relative to a baseline case) and noise reduction.

Figure 8 shows that in the cases of LB41 and LB90, the foreheads of the recirculation bubbles are observed at $x/D \approx 0.5$, whereas LB131 displays its forehead close to $x/D \approx 0.7$. This observation suggests that the vortex-shedding mechanism is primarily affected by the blowing applied on the windward and leeward sides of the cylinder and leads to a particular flow behaviour in the recirculation region. Furthermore, the forehead position of the recirculation bubble may help explain the mechanism of the increase in broadband spectral content in the cases of LB41 and LB90 compared with the baseline (see figure 5). According to Doolan (2009), the near-wake region of a circular cylinder is characterised by turbulent flow exhibiting 3-D velocity fluctuations across different frequencies and phases. These turbulent fluctuations directly influence the pressure fluctuations on the cylinder surface, contributing to its acoustic signature. In addition, the presence of a high-frequency broadband spectrum in both near-field pressure and far-field noise can be attributed to small-scale, high-frequency turbulence fluctuations occurring in the

near-wake region. Hence, the attachment of the recirculation bubbles forehead to the rear side of the cylinder in the cases of LB41 and LB90 is expected to generate small-scale high-frequency fluctuations with higher-energy content in the near-wake region. This phenomenon contributes to the observed high broadband spectral content in figure 5.

The emergence of a FAA is observed in figure 8(*a–d*), which can be related to the development of the recirculation region and the minimum pressure imposed in the vortex core. In particular, the depression region reaches its minimum value specifically in the zones where the time-averaged footprints of the von Kármán vortices are located (Greco *et al.* 2020). Showkat Ali, Mahdi & Da Silva (2018) emphasised that the pressure difference between the inside and outside of the vortex core creates a partial vacuum (suction), which facilitates the acceleration of flow in the near-wake region.

In figure 8(*a*), the FAA is observed for the baseline within $0 \lessapprox x/D \lessapprox 0.75$ and $\pm 0.5 \lessapprox y/D \lessapprox \pm 1$, followed by velocity overshoot near the separated shear layers. The LB41, however, presents a broader FAA within $0 \lessapprox x/D \lessapprox 1.5$ and $\pm 0.5 \lessapprox y/D \lessapprox \pm 1.2$ with much more streamlined behaviour than that of the baseline, which is consistent with the delay in vortex shedding. Therefore, LB41 restrains the entrainment of high-momentum fluid from the free stream into the wake near the base of the cylinder, resulting in lower momentum transfer and slower vertical flow movement, as shown in figure 8(*f*). On the other hand, LB90 exhibits the opposite behaviour, where higher momentum transfer and faster vertical flow movement occur (see figure 8*g*). The size of the FAA observed for LB131 is smaller compared with LB41; being $0 \lessapprox x/D \lessapprox 1.2$ and $\pm 0.5 \lessapprox y/D \lessapprox \pm 1$, suggesting that vortex-shedding mechanism should be different from that of LB41. Indeed, the discharge of flow into the shear layers in the case of LB131 resembles a vortex-shedding mechanism commonly observed in porous materials.

To more accurately categorise the vortex-formation regions, the vortex core length, $L_{vc}$, the circulation length, $L_r$, and the vortex formation length, $L_f$, marked by the circle, square and triangle symbols in figure 8, respectively, are estimated from the distributions of $\bar{u}/U_\infty$ and the r.m.s. of the vertical velocity fluctuations, $v'_{rms}/U_\infty$, along $y/D = 0$ as presented in figures 9(*a*) and 9(*b*), respectively. These locations for the baseline and LB cases are also provided in table 3. As demonstrated by Williamson (1996), $L_{vc}$ corresponds to the core position of the mean recirculation region, while $L_r$ is defined as the streamwise length of the saddle point, where the flow field from outside the wake crosses the centreline. As shown in figure 9(*a*), the $x$-position of the maximum velocity deficit, $\bar{u}_d/U_\infty$, or minimum (dip) $\bar{u}/U_\infty$ can be an estimate of $L_{vc}$. Therefore, a strong reverse flow occurs in the centre of main recirculation region (vortex cores) as previously observed in figure 8. For the baseline, it is observed that $L_{vc}$ is around $0.75D$ when $\bar{u}_d/U_\infty \approx -0.1$. For LB41 and LB131, stronger reverse flow ($\bar{u}_d/U_\infty \approx -0.2$ and $-0.12$, respectively) occurs at $L_{vc} \approx 1.5D$, which indicates that the application of LB cases in the boundary layer and separated shear layers, respectively, moves the vortex cores farther downstream. In contrast, LB90 pulls the vortex cores slightly upstream by approximately $0.05D$ relative to the baseline case.

The $\bar{u}/U_\infty$ profile can also be used to estimate $L_r$ as a streamwise location where $\bar{u}/U_\infty = 0$ (He, Li & Wang 2014), corresponding to the end of the recirculation region. For the baseline, $L_r$ levels out at a value of approximately $1.2D$ in the upper end of the subcritical regime (Norberg 1987), which is consistent with the findings of the present experimental study, as shown in table 3. The $L_r$ values clearly show that the recirculation bubbles for each LB except LB90 are more extended along the streamwise direction in comparison with the baseline. The results show while both LB41 and LB131 present vortex cores at $L_{vc} \approx 1.5D$, LB41 has larger recirculation bubbles compared with LB131.

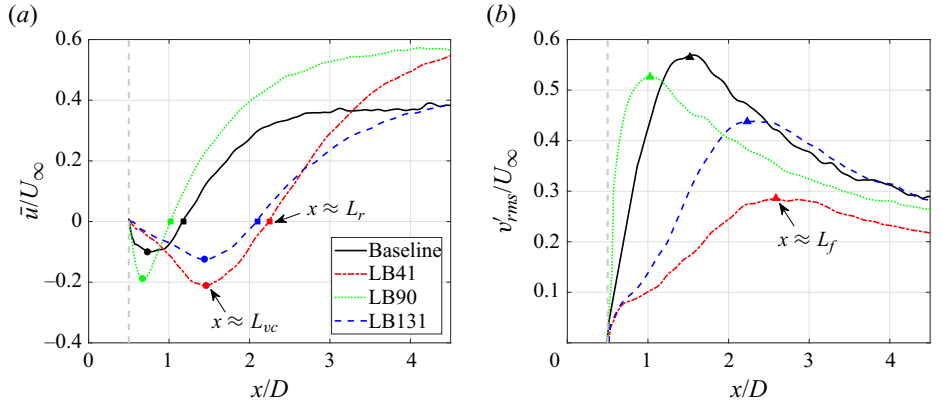


Figure 9. (*a*) Normalised time-averaged streamwise velocity, $\bar{u}/U_\infty$, and (*b*) the root-mean-square (r.m.s.) of the vertical velocity fluctuations, $v'_{rms}/U_\infty$, along the centreline ($y/D = 0$). The solid circle, square and triangle symbols represent $x \approx L_{vc}$, $L_r$ and $L_f$, respectively. The vertical dashed grey lines indicate the base of the cylinder at $x/D = 0.5$.

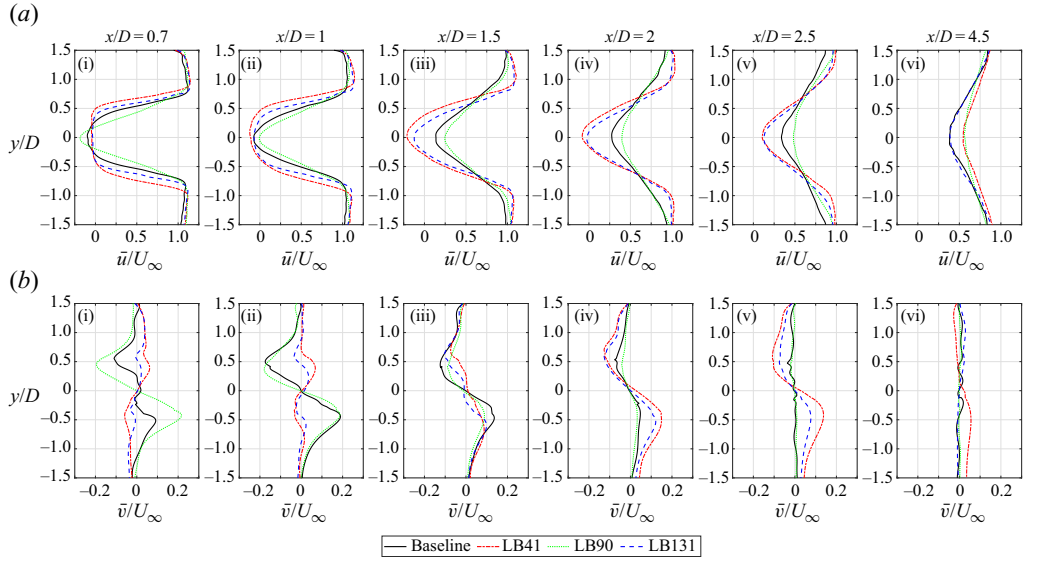


Figure 10. Normalised time-averaged $x$- and $y$-components of velocity, (*a*i–vi) $\bar{u}/U_\infty$ and (*b*i–vi) $\bar{v}/U_\infty$, respectively. The selected stations correspond to $x \approx L_{vc}$, $L_r$ and $L_f$ of the baseline and LB cases as shown in figure 9.

| Cases | $L_{vc}/D$ | $L_r/D$ | $L_f/D$ | $\bar{u}_d/U_\infty$ |
|---|---|---|---|---|
| Baseline | 0.75 | 1.2 | 1.5 | −0.10 |
| LB41 | 1.50 | 2.3 | 2.6 | −0.20 |
| LB90 | 0.70 | 1.0 | 1.1 | −0.19 |
| LB131 | 1.50 | 2.1 | 2.2 | −0.12 |

Table 3. The vortex core length, $x \approx L_{vc}$, the length of the recirculation region, $x \approx L_r$, the length of the vortex-formation region, $x \approx L_f$, and maximum centreline velocity deficit, $\bar{u}_d/U_\infty$, for the baseline and LB cases. The results are extracted from figure 9.

The recirculation bubbles are observed within $0.5 \lessapprox x/D \lessapprox 2.3$ and $0.7 \lessapprox x/D \lessapprox 2.1$ in the cases of LB41 and LB131, respectively, as depicted in figure 8. The discrepancy in the recirculation patterns between LB131 and LB41 can potentially be attributed to a reduction in reverse flow observed in the case of LB131 (see figure 9*a*). This mechanism will be further discussed and elaborated on in the upcoming detailed analysis in § 5.4.

The length $L_f$ is defined as the distance between the cylinder centre and the end of the vortex formation region, where the maximum r.m.s. of the vertical velocity fluctuations are obtained along $y/D = 0$ (see figure 9*b*). Bevilaqua (1973) demonstrated that an increase in $v'_{rms}/U_\infty$ is associated with the presence of large swirling turbulent structures, i.e. the formation of vortex shedding, and a highly anisotropic flow. As shown in figure 9(*b*), LB90 exhibits the maximum $v'_{rms}/U_\infty$ at $L_f \approx 1D$, which is approximately $0.5D$ closer to the cylinder than the baseline case. As a result, LB90 generates a more energetic and turbulent flow field in the vicinity of the cylinder when compared with the baseline case. At $x/D \gtrapprox 1$, however, LB90 shows a reduction in $v'_{rms}/U_\infty$ from that of the baseline. As anticipated, other LB cases yield greater $L_f$ values relative to the baseline and are consistent with a reduction in $v'_{rms}/U_\infty$ magnitude close to the cylinder. The LB41 reveals that the vortex-formation region ends at $L_f \approx 2.6D$, which is the maximum length among all LB cases (see table 3). Furthermore, LB41 demonstrates a notable reduction in vertical velocity fluctuations across the wake region.

Figure 10 presents the profiles of $\bar{u}/U_\infty$ and $\bar{v}/U_\infty$ at different locations downstream of the cylinder, namely $x/D = 0.7$, 1, 1.5, 2, 2.5 and 4.5. For a typical cylinder, the $\bar{u}/U_\infty$ profile varies gradually from a 'top hat' to a Gaussian-type as $x/D$ increases, which is due to the entrainment of the high-velocity fluid from the outer region into the wake (Heidari 2016). The fluid entrainment also increases the streamwise velocity magnitude in the inner region as one moves downstream behind the cylinder, particularly along the axis of symmetry. The wake region corresponding to the 'top hat'-type profile initiates just behind the cylinder ($x/D = 0.5$) with a width of approximately $1D$ ($-0.5 \lessapprox y/D \lessapprox 0.5$) and ends at a downstream location where a transition to a Gaussian-type profile starts. In the 'top hat'-type profile, the inner region is characterised by a minimum constant velocity, indicating a laminar flow with minimal turbulence. At $x/D = 0.7$ as shown in figure 10(*a*i), the $\bar{u}/U_\infty$ profile of LB90 is a Gaussian-type yet other LB cases present a 'top hat'-type profile. Gaussian-type $\bar{u}/U_\infty$ profiles for other LB cases are observed away from the base of the cylinder at $x/D = 1.5$ (see figure 10*a*iii). The proximity of $x/D = 0.7$ and 1.5 to $L_{vc}$ for LB90 and other LB cases, respectively (as shown in table 3), suggests that (i) the wake region with a Gaussian-type profile originates from the vortex cores and (ii) LB90 exhibits a higher fluid entrainment compared with the other LB cases, as will be discussed in more detail in § 5.4.

From figure 10(*b*i–v), it is observed that the significant variation of $\bar{v}/U_\infty$ in the wake of each case within $-0.5 \lessapprox y/D \lessapprox 0.5$ occurs between the values of $L_{vc}$ and $L_r$ or $L_f$ for each case. The observed variation can be ascribed to the intricate interaction between shear layers as part of the fluid entrainment process in the wake. This occurs when high-momentum fluid from the free stream penetrates the wake, leading to a region of diminished vertical velocity near the wake centreline. However, as the flow progresses away from the centreline towards the edges of the separated shear layers ($y/D \approx \pm 0.5$), the velocity experiences an increase. It is observed that a very rapid vertical flow movement occurs within $0.7 \leq x/D \leq 1$ for LB90 (see figure 10*b*i,ii) or within $1.5 \leq x/D \leq 2.5$ for LB41 (see figure 10*b*iii,v). While some LB cases exhibit similar $\bar{u}_d/U_\infty$ values (such as LB41 and LB90, as shown in table 3), the significant variation in $\bar{v}/U_\infty$ within the range of $L_{vc} \lessapprox x \lessapprox L_r$–$L_f$ is more pronounced for LB90. For LB90, the variation range

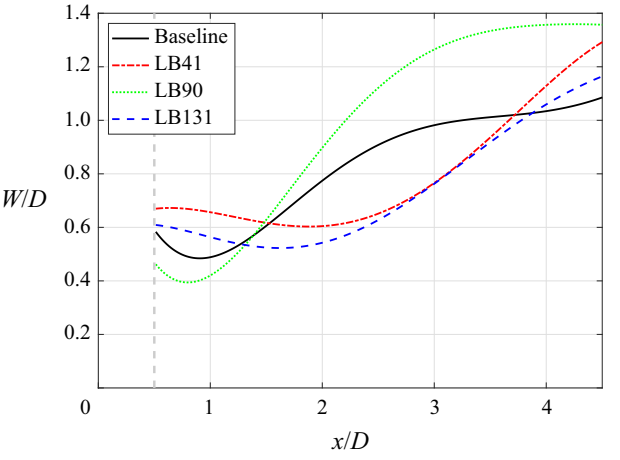


Figure 11. Variation of the normalised wake width, $W/D$, with respect to $x/D$. Curves in this figure are fitted splines to the original data, and the vertical dashed grey line indicates the base of the cylinder at $x/D = 0.5$. The wake centreline corresponds to $W/D = 0$.

of $\bar{v}/U_\infty$ is approximately $-0.2 \leq \bar{v}/U_\infty \leq 0.2$, whereas for LB41 cases, it is around $-0.15 \leq \bar{v}/U_\infty \leq 0.15$. In the case of LB131, the $\bar{v}/U_\infty$ exhibits variations approximately between $-0.12$ and 0.12, as depicted in figure 10(*b*iii,iv).

Based on the analysis of near-field pressure, far-field noise and flow characteristics, it can be concluded that the vertical flow movement plays a significant role in the generation of vortex shedding noise. The observations in figure 8 indicate that all LB cases, except LB90, delay the vortex shedding and promote the farther-downstream roll-up of shear layers. This delay in vortex shedding is consistent with the observed base pressure recovery (Showkat Ali *et al.* 2018) and reduced momentum transfer near the cylinder. Consequently, the vertical movement of the flow near the cylinder is reduced, leading to the suppression of surface pressure fluctuations, lift fluctuations (see figures 6 and 7, respectively) and a reduction in vortex shedding noise (see figure 5). These findings align with the stabilisation of the near wake and the development of a more streamlined flow pattern, as evident from the flow visualisation in figure 8.

Figure 11 shows the normalised wake width, $W/D$, defined as where the velocity is restored to half of $\bar{u}_d/U_\infty$ (He *et al.* 2014; Duan & Wang 2021). The $W/D$ depends primarily on the scale of the Kármán vortices in the wake (Duan & Wang 2021). As the periodic entrainment of the shear layers causes them to move towards the centreline, the wake width decreases immediately behind the cylinder to reach a minimum within $x \approx L_{vc}$–$L_r$ for each case. The wake width then vertically expands for $x \gtrapprox L_{vc}$–$L_r$ as a result of turbulent mixing (He *et al.* 2014). As reported by Duan & Wang (2021), the occurrence of intense turbulent mixing within the wake is attributed to the simultaneous acceleration of wake vortices to the convective velocity and their mutual interaction. It is observed that LB90 displays a narrower wake compared with the baseline up to $x/D \approx 1.5$. However, beyond this point, the wake width of LB90 increases, suggesting the generation of larger coherent flow structures compared with the baseline. On the contrary, for other LB cases, particularly LB41, the opposite trend is observed compared with LB90. Up to $x/D \approx 2.6$, where the vortex-formation region ends in the case of the LB41, LB41 exhibits a wider wake in comparison with LB131. This observation further supports the notion of distinct recirculation regions and different vortex-shedding mechanisms between LB41 and LB131.

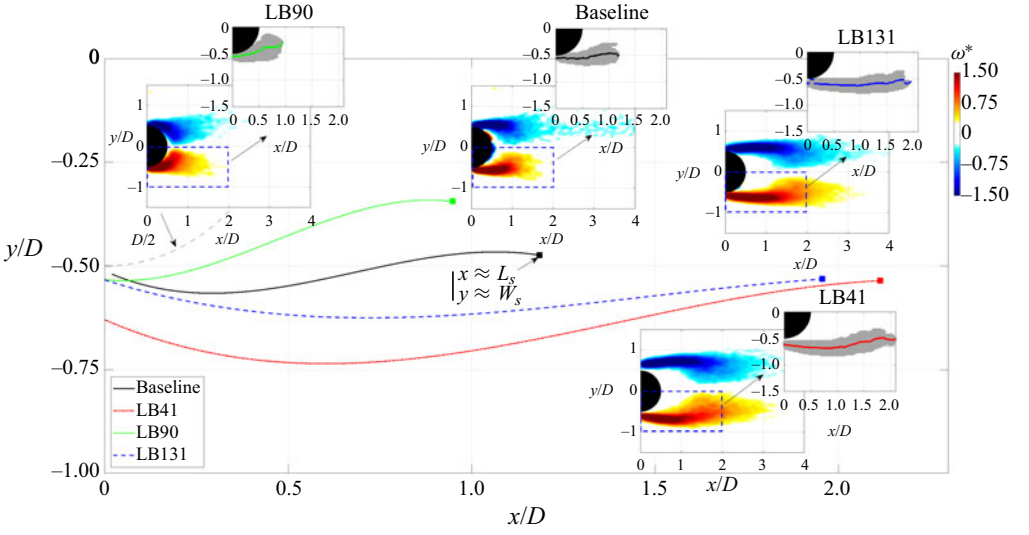


Figure 12. Shear layer trajectory from the bottom side of the cylinders. Contour plots represent the normalised time-averaged vorticity, $\omega^* = \bar{\omega}_z D/U_\infty$, and grey dots depict regions where $\omega^* \geq 0.75$. The square symbols indicate the end of the shear layer at $x \approx L_s$ and $y \approx W_s$. The curves in this figure are fitted splines to the original data.

### 4.2. *Shear layer trajectory*

The propagation of the shear layer into the wake, as a result of LB, is investigated here. The trajectory of the shear layer is estimated by taking the averaged $y$-coordinate of the normalised time-averaged vorticity field ($\omega^* = \bar{\omega}_z D/U_\infty \geq 0.75$), at each $x$-coordinate. The vorticity regions (identified as grey dots), and shear layer trajectories (as a coloured line that passes through these dots) are shown as subplots in figure 12 for each case.

For the baseline case, it is observed that the trajectory line comes to an end at approximately $x/D \approx 1.2$. This observation confirms that the length of the turbulent shear layer, $L_s$, is nearly equal to the recirculation length, i.e. $L_s \approx L_r$. At $x \approx L_s$, the trajectory of the shear layer is closest to the centreline, denoted as $y \approx W_s$, which is consistent with the minimum width of the wake depicted in figure 11. The strong interaction between the upper and lower shear layers, therefore, would tend to occur at this location, where Gerrard (1966) reported that the shear layer thickness or diffusion length, affects the vortex-shedding frequency.

For LB90, both $L_s$ and $W_s$ decrease compared with the baseline, indicating a more intense interaction between the shear layers that occurs farther upstream. This observation is consistent with (i) the increased turbulence in the oscillating near wake just behind the cylinder (refer to § 4.3) and (ii) the higher broadband energy content of vertical velocity fluctuations (refer to § 4.4). In contrast, the other LB cases show larger $L_s$ and $W_s$ compared with the baseline, with LB41 demonstrating a more pronounced effect in this regard.

### 4.3. *Production of energy and turbulence*

Figure 13 presents the normalised $x$- and $y$-components of Reynolds stress, $\overline{u'u'}/U_\infty^2$ and $\overline{v'v'}/U_\infty^2$, respectively, and shear stress $\overline{u'v'}/U_\infty^2$. The $\overline{u'u'}/U_\infty^2$ and $\overline{v'v'}/U_\infty^2$ represent the variation in turbulence kinetic energy (TKE) across the wake, while $\overline{u'v'}/U_\infty^2$ depicts the

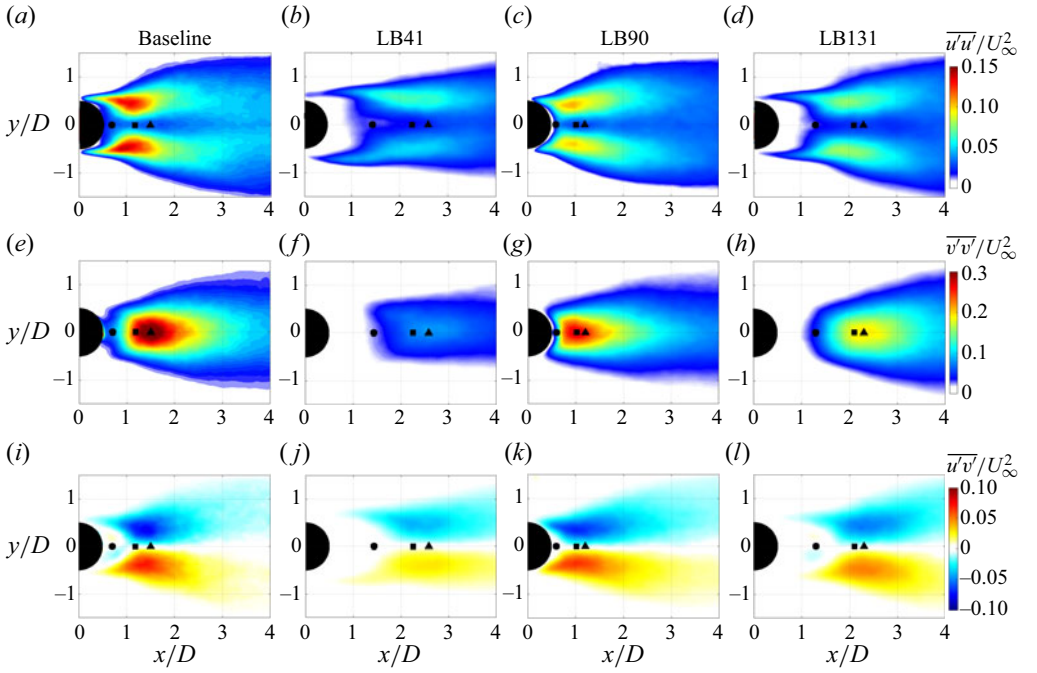


Figure 13. (*a–d*) Normalised time-averaged $x$-component of Reynolds stress, $\overline{u'u'}/U_\infty^2$, (*e–h*) normalised time-averaged $y$-component of Reynolds stress, $\overline{v'v'}/U_\infty^2$ and (*i–l*) normalised time-averaged shear stress, $\overline{u'v'}/U_\infty^2$. For each case, the solid circle, square and triangle symbols represent $x \approx L_{vc}$, $L_r$ and $L_f$, respectively, (see figure 9).

flux of momentum transported by turbulent fluctuations and is also relevant to the acoustic analysis (Ffowcs Williams & Hall 1970).

In the baseline case, the Reynolds stress $\overline{u'u'}/U_\infty^2$ exhibits dual peak regions. These peaks are observed at $y/D \approx \pm 0.5$ within the separated shear layers, and within the range of $0.75 \lessapprox x/D \lessapprox 1.2$–$1.5$ in the high-momentum transfer area between $L_{vc}$ and $L_r$–$L_f$. The dual peaks serve as indicators of the concentration of vortical structures within the shear layers and the enhanced turbulent fluctuations and momentum transfer within the high-momentum transfer region. These regions experience complex flow dynamics, with interactions between the separated flow and surrounding fluid leading to increased turbulence, vorticity and mixing. The maximum value of $\overline{v'v'}/U_\infty^2$, however, is observed at $y/D = 0$ and $x/D \approx 1.2$–$1.5$, suggesting that the momentum transfer beyond the vortex core centre ($x \approx 0.75$), which occurs in the vicinity of the centreline, contributes to an increase in the vertical periodic fluctuations. These fluctuations play a role in separating the vortices concentrated in the tails of the shear layers during the alternate shedding of the vortices at the end of the vortex-formation region. The interaction between the vortices and the surrounding flow in this region leads to enhanced turbulence and momentum exchange, resulting in the observed maximum $\overline{v'v'}/U_\infty^2$ on the centreline.

The results demonstrate that beyond $x \approx 0.75$, the magnitude of $\overline{v'v'}/U_\infty^2$ is higher than that of $\overline{u'u'}/U_\infty^2$, which can be attributed to two factors. Firstly, the streamwise velocity component aligns with the mean flow direction, resulting in a more organised and coherent flow structure. This alignment leads to relatively weaker turbulent fluctuations in the streamwise direction, causing a lower magnitude of $\overline{u'u'}/U_\infty^2$. Secondly, the shedding of

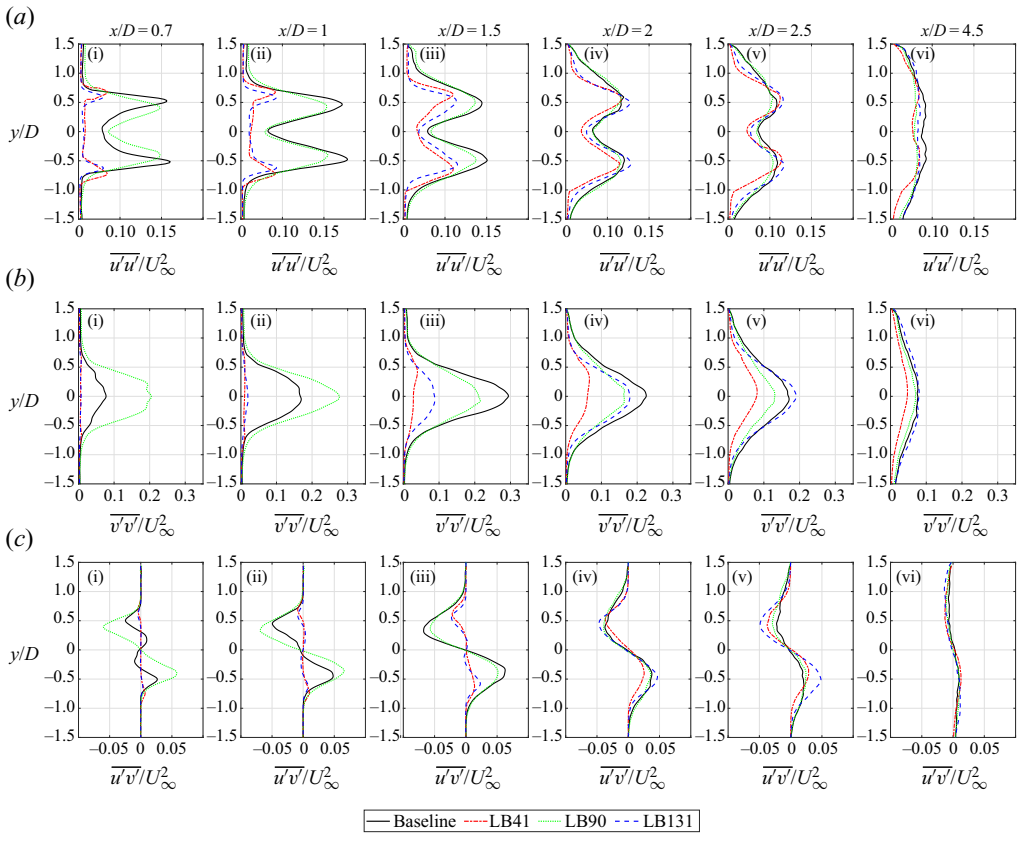


Figure 14. (*a*i–vi) Normalised time-averaged $x$-component of Reynolds stress, $\overline{u'u'}/U_\infty^2$, (*b*i–vi) normalised time-averaged $y$-component of Reynolds stress, $\overline{v'v'}/U_\infty^2$ and (*c*i–vi) normalised time-averaged shear stress, $\overline{u'v'}/U_\infty^2$, at different $x$-locations corresponding to $x \approx L_{vc}$, $L_r$ and $L_f$ for the baseline and LB cases as shown in figure 9.

vortices in the wake is primarily driven by the shear layers instabilities and the roll-up of the shear layers. These instabilities are more prominent in the vertical direction, leading to stronger vertical velocity fluctuations and a higher magnitude of $\overline{v'v'}/U_\infty^2$.

As shown in figure 13, the LB cases exhibit maximum values of $\overline{u'u'}/U_\infty^2$ and $\overline{v'v'}/U_\infty^2$ within the ranges of $L_{vc} \lessapprox x \lessapprox L_r$–$L_f$ and $x \approx L_r$–$L_f$, respectively, similar to the baseline. From figure 14(*a*i–vi), it can be observed that each LB case leads to a reduction in $\overline{u'u'}/U_\infty^2$, particularly in the dual peak regions up to their respective $L_{vc}$. The LB41 case exhibits a more significant reduction compared with the other LB cases. However, no significant decrease is observed for LB90, which could be attributed to the smaller size of the vortex-formation region in this case.

The quantity $\overline{v'v'}/U_\infty^2$ is also decreased by each LB, particularly along $y/D = 0$. However, the trends with respect to $x/D$ vary among the different LB cases, as shown in figure 14(*b*i–vi). This indicates that each LB affects the vortex shedding process through different mechanisms. The application of LB41 within the boundary layer causes the shear layers to stretch and roll up farther downstream, which results in a reduction in $\overline{v'v'}/U_\infty^2$ across the entire range of $x/D$, as observed in figure 9(*b*). In this case, the most significant performance is observed near the base of the cylinder, and the level of

reduction decreases as $x/D$ increases. In the case of LB90, where the blowing is applied perpendicular to the free stream at the cylinder shoulders just beyond the separation point, a substantial increase in $\overline{v'v'}/U_\infty^2$ is observed near the base of the cylinder, extending up to $x/D = 1$ ($x \approx L_r$ or $L_f$). This increase is attributed to the rapid vertical flow movement during rapid rolling up of the shear layer, which occurs farther upstream in this case (see figures 9*b* and 10*b*i–vi). While it is not significant, LB90 suppresses $\overline{v'v'}/U_\infty^2$ for $x/D > 1$. In the case of LB131, the separated shear layers are directly influenced by the blowing vortices, and their behaviour regarding $\overline{v'v'}/U_\infty^2$ is opposite to LB90. It should be noted that the transition point ($x \approx L_r$ or $L_f$) moves downstream for LB131, occurring at $x/D > 2$. From figure 14(*a*vi,*b*vi), it is evident that at $x/D = 4.5$ and $y/D = 0$, $\overline{u'u'}/U_\infty^2$ remains lower than $\overline{v'v'}/U_\infty^2$. This observation suggests that the flow in this region still exhibits anisotropic characteristics and has not fully transitioned to the far wake with a more isotropic state. However, LB41 shows a greater tendency to approach this isotropic state compared with the other cases. This is evident from the fact that $\overline{v'v'}/U_\infty^2$ for LB41 is approximately one and a half times as high as $\overline{u'u'}/U_\infty^2$, while in the other cases it is two and a half times higher. This suggests that LB41 exhibits a stronger development towards isotropy, with a more balanced distribution of turbulence intensity between the streamwise and vertical directions.

From figure 13(*i–l*), it can be observed that $\overline{u'v'}/U_\infty^2$ exhibits a significant variation within the range of $-0.5 \lessapprox y/D \lessapprox 0.5$, while $x$ varies approximately from $L_{vc}$ to $L_r$–$L_f$. This behaviour is similar to the observed variation of $\bar{v}/U_\infty$ in figure 8(*e–h*). The development and interaction of the shear layers with the surrounding flow result in intensified velocity gradients and vorticity. This intensification leads to enhanced turbulence and vorticity, causing increased flow fluctuations and the generation of shear stress. The concentration and interaction of vortices within the shear layers further amplify the turbulence and momentum transfer. These vortices create coherent structures and eddies that shed at the end of the vortex-formation region, thereby contributing to higher shear stress levels.

It is observed in figure 14(*c*i–vi) that the $x/D$-range where $\overline{u'v'}/U_\infty^2$ maximises in the cases of LB41 and LB90 is $1.5 \leq x/D \leq 2.5$ and $0.7 \leq x/D \leq 1$, respectively. These observations align with the patterns seen in figure 10(*b*i–vi) and indicate that the rapid vertical movements of the flow are driven by the momentum carried by the turbulent fluctuations. At a distance far away from the cylinder, specifically at $x/D = 4.5$, the profiles of $\overline{u'v'}/U_\infty^2$ appear relatively flat. This indicates that the flow fields in the wake tend to be nearly uniform, with little variation in the momentum flux. In this region, the turbulent fluctuations have dissipated, resulting in a more stable and less dynamic flow. By inspecting figure 14(*c*i–vi), it is clear that all LB cases, except for LB90, result in a reduction of $\overline{u'v'}/U_\infty^2$ compared with the baseline, but this reduction is only observed up to $x/D = 2$. However, it should not be assumed that an increase in $\overline{u'v'}/U_\infty^2$ by LB41 and LB131 at $x/D \geq 2$ would lead to an increase in tonal noise relative to the baseline. The proximity of the vortex-formation region to the cylinder plays a role in influencing the noise reduction achieved by LB techniques. In the case of LB90, vortex shedding occurs rapidly, resulting in a significant vertical variation of $\overline{u'v'}/U_\infty^2$ close to the cylinder. This variation promotes lift fluctuations and leads to increased far-field noise. On the other hand, other LB cases, particularly LB41, cause a delay in vortex shedding, resulting in a significant variation of $\overline{u'v'}/U_\infty^2$ farther downstream. This is consistent with the emergence of a weaker hydrodynamic field with lower energy content near the cylinder. The reduction of flow-induced noise by LB techniques is also influenced by factors such as TKE and the

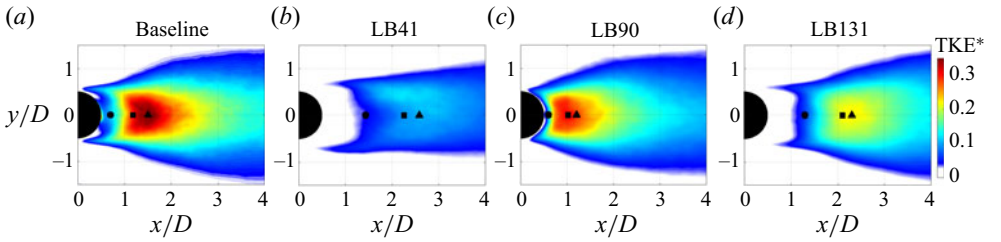


Figure 15. Normalised TKE, TKE*, for the baseline and LB cases. For each case, the solid circle, square and triangle symbols represent $x \approx L_{vc}$, $L_r$ and $L_f$, respectively (see figure 9).

scale of the most energetic fluctuations in the vicinity of the cylinder. These factors play a role in shaping the hydrodynamic field and the associated noise characteristics.

Figure 15 shows that the maximum TKE* $= (\overline{u'u'} + \overline{v'v'})/(2U_\infty^2)$ appears at $y/D = 0$ and $x \approx L_r$–$L_f$ for each case, which is consistent with the observations in figure 14(*b*i–vi). Since the maximum $\overline{v'v'}/U_\infty^2$ (see figure 14*b*i–vi) is significantly greater than that of $\overline{u'u'}/U_\infty^2$ (see figure 14*a*i–vi), TKE* is dominated by vertical fluctuations as demonstrated by others (Feng & Wang 2010; He *et al.* 2014; Octavianty & Asai 2016; Qu *et al.* 2017; Chauhan *et al.* 2018; Sharma & Dutta 2020). It is observed for the baseline that the intense TKE* region (TKE* $\gtrapprox 0.3$) is larger in vertical scale compared with that of $\overline{v'v'}/U_\infty^2$. This discrepancy can be related to the complex interactions between the shear layers and the entrained fluid, which generate significant shear and vorticity, promoting turbulence production. In addition, the energy cascade process allows for the generation of vortices and turbulent eddies, which contribute to the overall vertical scale of turbulence in the wake.

While the TKE* of LB90 is lower in magnitude compared with the baseline, which is consistent with the observation in figure 13(*e*,*g*), the rapid rolling up of the shear layers concentrates the vorticity near the cylinder (smaller vortex formation size), which facilitates their mutual interaction to increase TKE* in this region. For other LB cases a delay in vortex shedding elongates the shear layers and impedes their interaction, thus TKE* decreases close to the cylinder. Overall, the vortex formation length and the interaction between the shear layers determine the level of TKE*, which is a measure of turbulence mixing (Benard *et al.* 2008; Schäfer, Breuer & Durst 2009; Feng & Wang 2010).

### 4.4. *Velocity fluctuations power spectra in the wake*

Figures 16 and 17 present the PSD of the $x$- and $y$-components of velocity fluctuations, $\Phi_{uu}$ and $\Phi_{vv}$ (dB Hz$^{-1}$, ref: 1 m s$^{-1}$), respectively. Upon observing the figures, a distinct tonal peak at the frequency of $f_1$ is noticeable for each case. This peak aligns closely with the $f_1$-tone characteristics depicted in figures 5 and 6, which suggests that the pronounced far-field noise and near-field pressure, respectively, can be attributed to the periodic shedding of vortices. In the case of the baseline, the $f_1$-tone achieves its maximum magnitude at $x/D = 1$ and 1.5 in the $\Phi_{uu}$ and $\Phi_{vv}$ spectra, as illustrated in figures 16(*f*) and 17(*f*), respectively. It is noteworthy that in this scenario, the shear layers undergo roll-up at $L_r \approx 1$ and subsequently shed vortices at $L_f \approx 1.5$ (see figure 9).

It is observed from figure 16(*a*,*b*,*f*) that the $\Phi_{uu}$ spectra of the baseline are purely broadband at the $f_1$-tone frequency along the centreline. Away from $y/D = 0$, however, they include the $f_1$-tone, which increases in magnitude with $y/D$ to reach a maximum at $y/D \approx 0.5$, where in the separated shear layers. In contrast, the $\Phi_{vv}$ spectra present

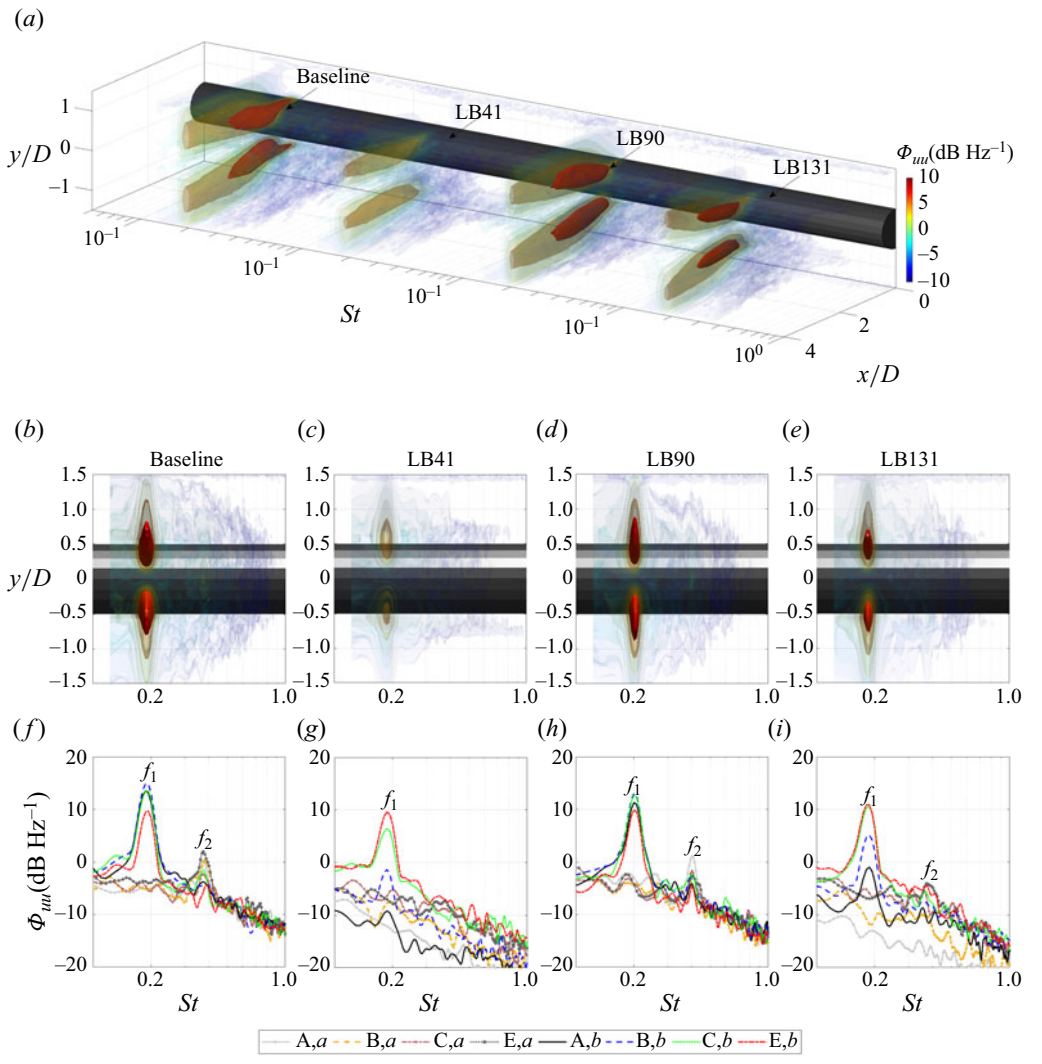


Figure 16. Streamwise velocity PSD, $\Phi_{uu} = 10\log_{10}\phi_{uu}$. (*a–e*) Isosurface of $\Phi_{uu}$ where transparency decreases with increasing $\Phi_{uu}$ and (*f–i*) the $\Phi_{uu}$ values along *a* ($y/D = 0$) and *b* ($y/D = 0.5$) for stations A ($x/D = 0.7$), B ($x/D = 1$), C ($x/D = 1.5$) and E ($x/D = 2.5$).

the $f_1$-tone at all measurement points across the wake yet decrease in magnitude within $y/D \approx 0$–$0.5$ as shown in figure 17(*a*,*b*,*f*). These findings indicate that the streamwise and vertical velocity fluctuations in the separated shear layers and along the centreline, respectively, contribute significantly to the vortex shedding, supporting the results of $\overline{u'u'}/U_\infty^2$ and $\overline{v'v'}/U_\infty^2$ (see figures 13 and 14) and their role in TKE production (see figure 15). However, the vertical velocity fluctuations exhibit a stronger influence on vortex shedding, as indicated by the larger magnitudes of the $f_1$-tone in the $\Phi_{vv}$ spectra compared with the $\Phi_{uu}$ spectra.

In addition to the $f_1$-tone, the first two harmonics are observed in figures 16(*f*) and 17(*f*), which indicate the footprint of velocity fluctuations in lift and drag oscillations of the cylinder. The $\Phi_{uu}$ spectra along $y/D = 0$ show non-negligible tonal peaks at the $f_2$-tone frequency in agreement with Showkat Ali *et al.* (2018), whereas these tonal peaks

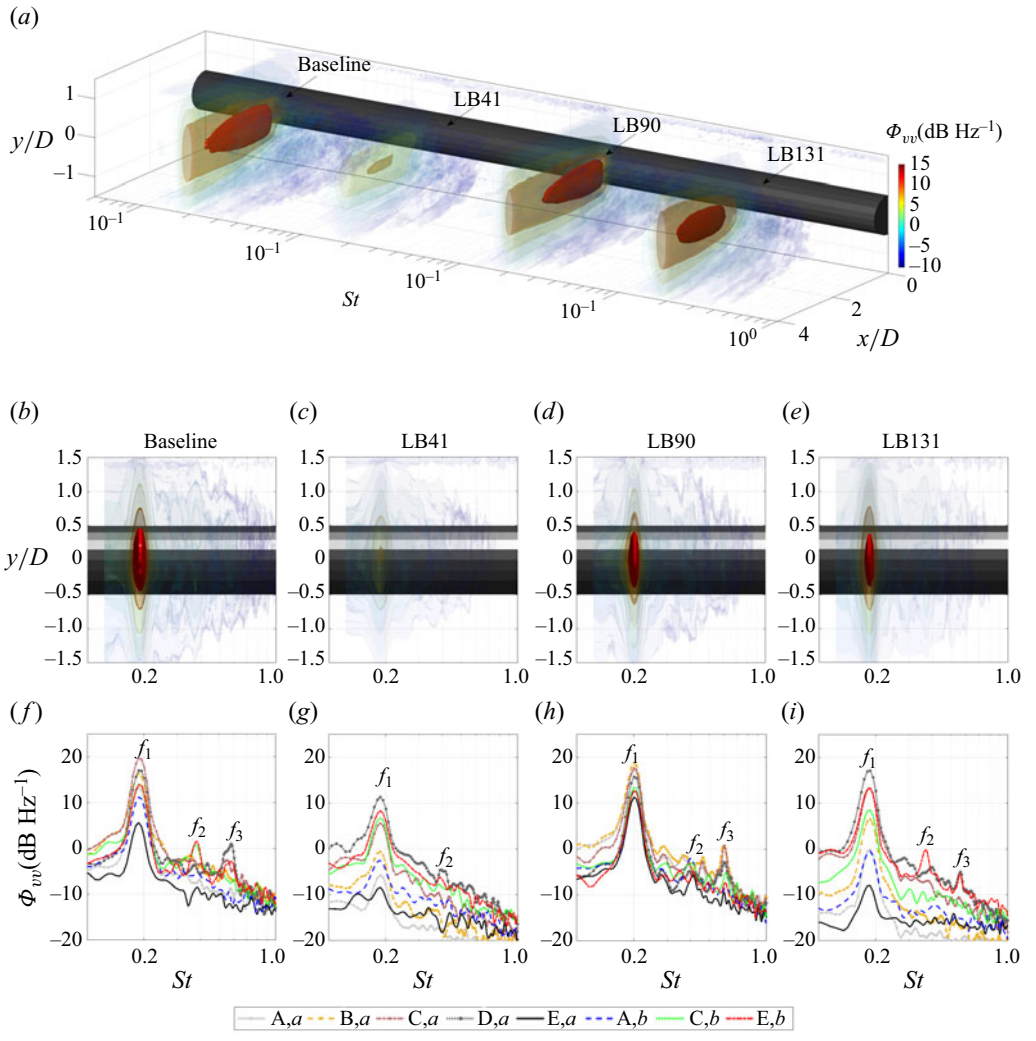


Figure 17. Vertical velocity PSD, $\Phi_{vv} = 10\log_{10}\phi_{vv}$. (*a–e*) Isosurface of $\Phi_{vv}$ where transparency decreases with increasing $\Phi_{vv}$ and (*f–i*) the $\Phi_{vv}$ values along *a* ($y/D = 0$) and *b* ($y/D = 0.5$) for stations A ($x/D = 0.7$), B ($x/D = 1$), C ($x/D = 1.5$), D ($x/D = 2$) and E ($x/D = 2.5$).

appear in the $\Phi_{vv}$ spectra along $y/D = 0.5$ beyond $x/D = 1.5$. It is observed that the $f_3$-tone tends to appear only in the $\Phi_{vv}$ spectra at $x/D = 1.5$. As mentioned in § 3.3, lift and drag oscillate in odd and even harmonics, respectively. In this context, vertical velocity fluctuations, particularly at $x \approx L_f$ and $y/D = 0$, play a significant role in generating lift fluctuations. This further supports the previous argument that high-momentum transfer, which affects the vertical flow movement, contributes to the fluctuations in lift.

From figure 16(*f–i*), it can be observed that each LB case, particularly LB41, is effective in reducing the magnitude of the $f_1$-tone in the $\Phi_{uu}$ spectra up to $x/D = 1.5$. Similarly, all LB cases lead to a decrease in the magnitude of the $f_1$-tone in the $\Phi_{vv}$ spectra across the range of $x/D$, as shown in figure 17(*f–i*). However, LB90 shows an increase in the magnitude of the $f_1$-tone in the $\Phi_{vv}$ spectra compared with the baseline, reaching up to $x/D = 1$. The observations of $\overline{v'v'}/U_\infty^2$ in figure 14(*b*i–vi) align with these findings and

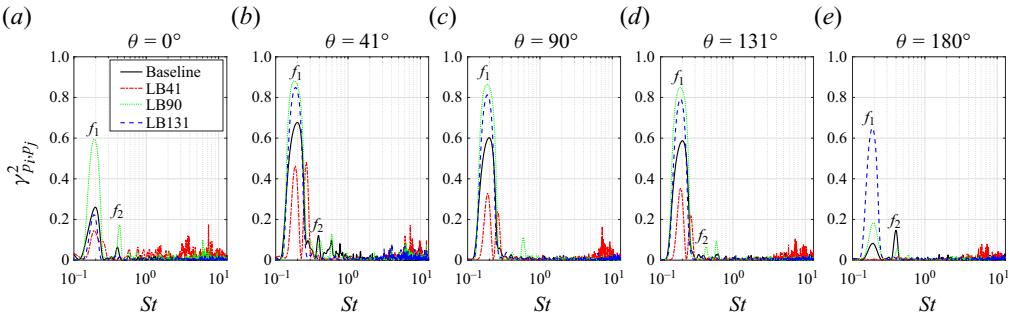


Figure 18. Coherence between the near-field pressure and far-field noise, $\gamma^2_{pp_s}$, in terms of $St$ for the pressure taps located at $\theta = 0°$, 41°, 90°, 131° and 180°. The labels $f_1$ and $f_2$ represent the fundamental vortex shedding tone (first harmonic) and second harmonic, respectively.

support the conclusion that reducing streamwise velocity fluctuations through LB does not necessarily lead to the suppression of dominant vortex structures.

### 4.5. *Near-field pressure to far-field noise coherence*

The emergence of a tonal peak at the $f_1$-tone frequency in both spectra of near-field pressure and far-field noise demonstrated the role of surface pressure fluctuations in the tonal noise generation mechanism. To gain a better understanding of the far-field propagation effects of the identified surface pressure fluctuations, the coherence between the near-field pressure and the far-field noise was calculated as

$$\gamma^2_{pp_s} = \frac{|\phi_{pp_s}(f)|^2}{\phi_{pp}(f)\phi_{p_sp_s}(f)}, \tag{4.1}$$

where $\phi_{pp_s}$ denotes the cross-spectrum between the acoustic and pressure signals, i.e. $p'$ and $p'_s$, respectively, and $\phi_{pp}$ and $\phi_{p_sp_s}$ are the autospectrum of each individual signal.

Figure 18 reveals that the baseline possesses high coherence at the $f_1$-tone frequency with broadband levels below 0.1. This finding provides support for the mechanism that tonal noise is primarily generated by the near-field pressure fluctuations caused by vortex shedding (Maryami *et al.* 2023*c*). In the baseline case, the $f_1$-tone magnitude is observed to be approximately 0.3 at $\theta = 0°$ and increases rapidly to around 0.65 at $\theta = 41°$. The magnitude then remains relatively constant within the range of $\theta = 41°$ to $\theta = 131°$ before dropping to zero at $\theta = 180°$. This trend highlights the significant contribution of surface pressure fluctuations, induced by vortex shedding in the preseparation and postseparation regions, to the generation of tonal noise (Maryami *et al.* 2023*c*). Previous studies have reported that surface pressure fluctuations near the flow separation point act as sound sources (Oguma *et al.* 2013) and strongly scatter sound in a region approximately from $\theta = 25°$ to 155° (Li, Rival & Wu 2021).

All LB cases exhibit approximately a trend analogous to that of the baseline concerning the variation of the $f_1$-tone magnitude in relation to peripheral angles. Within the preseparation and postseparation regions (i.e. $\theta = 41°$–131°), only LB41 exhibits a decrease in the magnitude of the $f_1$-tone compared with the baseline. This observation indicates that vortex shedding is effectively suppressed by LB41, leading to a dissipation of its energy content over a larger vortex-formation region (Suzuki & Colonius 2006). As a result, the vortex shedding does not generate a strong feedback signal to the cylinder,

thereby influencing the surface pressure fluctuations and propagating strong acoustic waves to the far field. Additionally, LB41 shows a dual tonal peak around the $f_1$-tone frequency, which is consistent with the far-field and near-field pressures observed in figures 5 and 6, respectively.

### 4.6. *Velocity-pressure coherence*

To investigate the impact of velocity fluctuations on the scattering of acoustic waves into the far field, the coherence relationship between the velocity fluctuation and sound pressure signals is computed using

$$\gamma_{up}^2 = \frac{|\phi_{up}(f)|^2}{\phi_{uu}(f)\phi_{pp}(f)}, \tag{4.2}$$

where $\phi_{up}(f)$ denotes the cross-PSD function between the velocity and sound pressure signals.

Figures 19 and 20 illustrate the coherence between the $x$- and $y$-components of velocity and far-field noise, represented by $\gamma_{up}^2$ and $\gamma_{vp}^2$, respectively. As expected, $\gamma_{up}^2$ and $\gamma_{vp}^2$ for the baseline present a strong tonal peak at the $f_1$-tone frequency, regardless of the measurement point in the wake. This confirms that velocity fluctuations responsible for vortex shedding are the primary mechanism of tonal noise. At the $f_1$-tone frequency along the centreline of the baseline, $\gamma_{up}^2$ remains below 0.1. However, within the separated shear layers, up to $x \approx L_r$–$L_f$, $\gamma_{up}^2$ reaches a maximum value of approximately 0.6–0.65, as indicated in figure 19$(b,f)$. Additionally, the maximum value of $\gamma_{up}^2$ is observed at $y/D \gtrapprox 0.5$. The maximum $\gamma_{up}^2$ follows the shear layer trajectory and ends at $x/D \approx 1.5$, indicating that the vortices within the shear layer are fed by the streamwise velocity fluctuations to shed into a vortex and scatter noise. In contrast, $\gamma_{vp}^2$ exhibits a consistent presence at the $f_1$-tone frequency with magnitudes ranging from approximately 0.63 to 0.7 at all measurement points, particularly along the centreline as shown in figure 20$(b,f)$. It is noted that the maximum values of $\gamma_{vp}^2$ are slightly higher than those of $\gamma_{up}^2$. Although this difference is not substantial, it implies that vertical velocity fluctuations are more likely to scatter acoustic waves to the far field from any position within the wake region. These observations support previous explanations regarding the influence of rapid vertical flow movement on tonal noise generation.

This interpretation holds true for all LB cases, with the exception of certain measurement points in the wake where some deviations from the observed trend may occur. From figures 19 and 20, it is evident that LB41 exhibits a greater potential than other LB cases to reduce the magnitude of the $f_1$-tone in the $\gamma_{up}^2$ and $\gamma_{vp}^2$ spectra compared with the baseline. While there is some reduction in the $f_1$-tone magnitudes from that of the baseline in the case of LB131 at certain measurement points, particularly outside of the separated shear layers, it is not as significant as in LB41. On the other hand, LB90 shows a similar magnitude of the $f_1$-tone compared with the baseline, and in some measurement points, it even surpasses the baseline's magnitude. The delayed vortex shedding caused by LB cases, particularly LB41, and the subsequent depletion of energy in the coherent flow structures can be considered as mechanisms contributing to the reduction in coherence level between velocity fluctuations and acoustic pressure fluctuations in the far field. A delay in vortex shedding depletes the momentum transfer in the region of vortex formation, resulting in a reduction of the energy content of the coherent flow structures. As a consequence, the hydrodynamic pressure field generated by velocity fluctuations may not have enough energy to produce strong acoustic waves that can propagate to the far field.

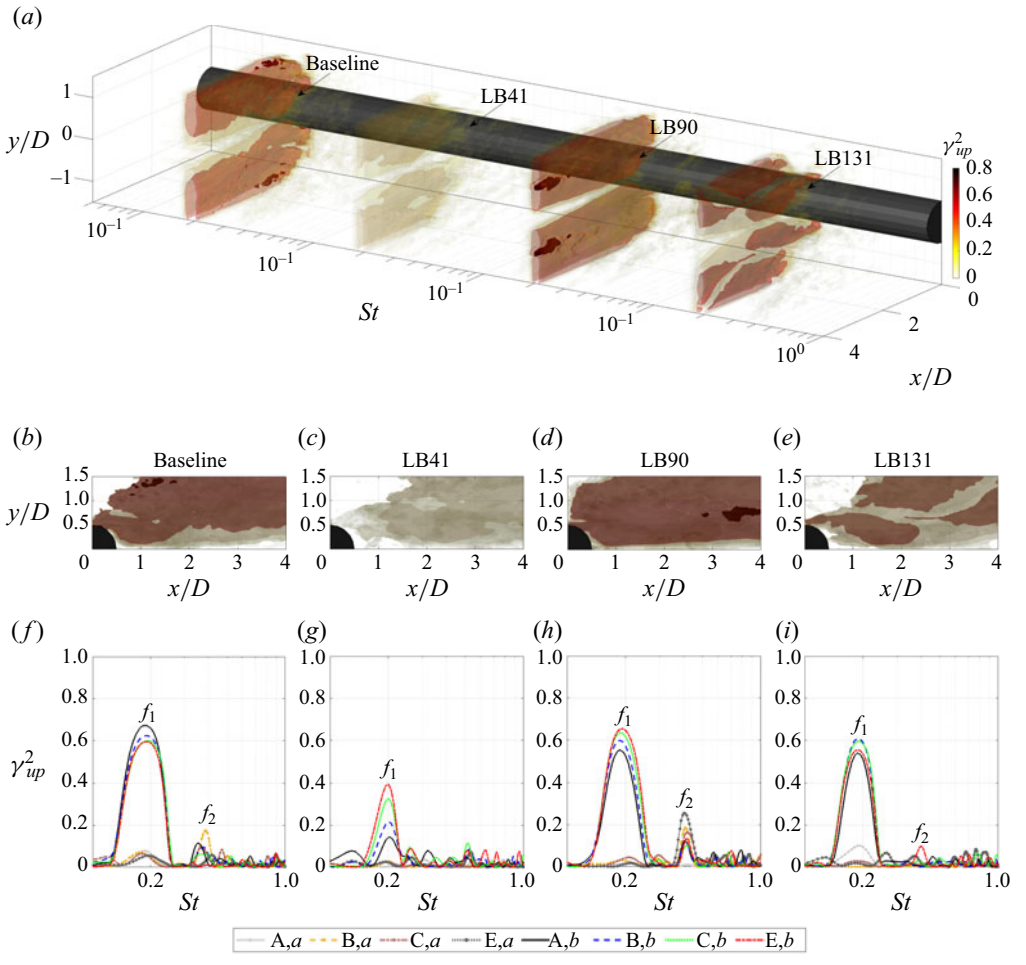


Figure 19. Streamwise velocity to far-field noise coherence ($\gamma^2_{up}$). (*a*) Isosurface of $\gamma^2_{up}$ where transparency decreases with increasing $\gamma^2_{up}$. (*b–e*) The values of $\gamma^2_{up}$ recorded in the *xy*-plane and (*f–i*) the values of $\gamma^2_{up}$ along *a* ($y/D = 0$) and *b* ($y/D = 0.5$) for stations A ($x/D = 0.7$), B ($x/D = 1$), C ($x/D = 1.5$) and E ($x/D = 2.5$).

Figures 21 and 22 show the coherence between the *x*- and *y*-components of velocity and the near-field pressure measured around the cylinder circumference, $\gamma^2_{up_s}$ and $\gamma^2_{vp_s}$, respectively. For brevity, the results are only presented for surface pressure fluctuations at angular locations $\theta = 0°$, 41°, 90°, 131° and 180°.

The results from each case demonstrate that both $\gamma^2_{up_s}$ and $\gamma^2_{vp_s}$ exhibit high values at the $f_1$-tone frequency. This behaviour is observed in various sections of the cylinder circumference, particularly in the region within $\theta = 41°$–131°, suggesting that during intermittent vortex shedding, the cylinder shoulders experience significant pressure fluctuations. It was already shown in figure 18 that $\gamma^2_{pp_s}$ is maximised at the $f_1$-tone frequency in the preseparation and postseparation regions. Therefore, the results in figures 21 and 22 confirm that the pressure fluctuations induced by vortex shedding at the shoulders of the cylinder generate strong acoustic waves that propagate to the far field. This aligns with the viewpoint of Inoue & Hatakeyama (2002) who demonstrated that

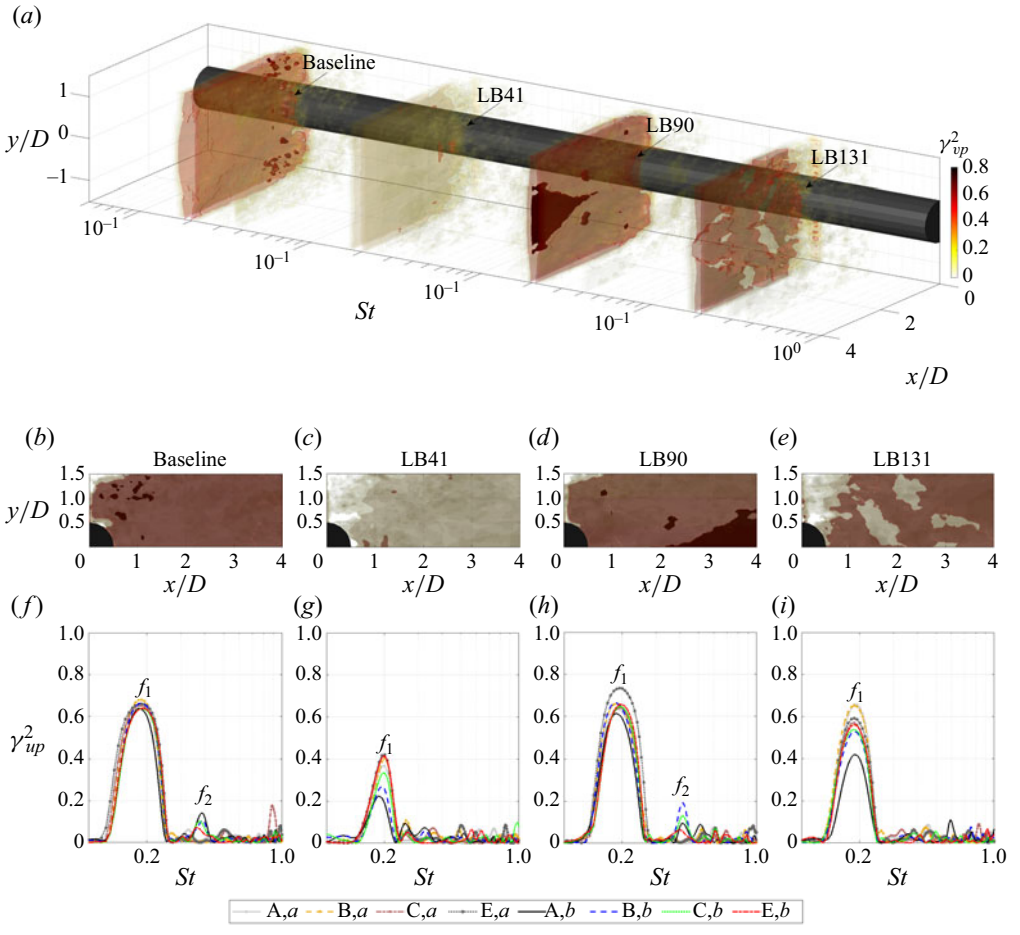


Figure 20. Vertical velocity to far-field noise coherence ($\gamma^2_{vp}$). (*a*) Isosurface of $\gamma^2_{vp}$ where transparency decreases with increasing $\gamma^2_{vp}$. (*b–e*) The values of $\gamma^2_{vp}$ recorded in the *xy*-plane and (*f–i*) the values of $\gamma^2_{vp}$ along *a* ($y/D = 0$) and *b* ($y/D = 0.5$) for stations A ($x/D = 0.7$), B ($x/D = 1$), C ($x/D = 1.5$) and E ($x/D = 2.5$).

pressure waves are produced by the alternating pressure pulses generated on both sides of the cylinder during vortex shedding.

The spatial distributions of $\gamma^2_{up_s}$ and $\gamma^2_{vp_s}$ at the $f_1$-tone frequency in the wake of each cylinder resemble those of $\gamma^2_{up}$ and $\gamma^2_{vp}$, respectively. This correspondence further supports the notion that surface pressure fluctuations and far-field noise are generated through the same underlying mechanism. Nevertheless, the magnitudes of the tonal peaks in $\gamma^2_{up_s}$ and $\gamma^2_{vp_s}$ are higher compared with those in $\gamma^2_{up}$ and $\gamma^2_{vp}$. This discrepancy can be attributed to the difference in the measurement point spacing. In the case of $\gamma^2_{up_s}$ and $\gamma^2_{vp_s}$, the maximum distance between measurement points is approximately $4.5D$, whereas it reaches approximately $23D$ for $\gamma^2_{up}$ and $\gamma^2_{vp}$. As a result, the localised measurements in the vicinity of the cylinder yield higher tonal peak levels. Figures 21 and 22 illustrate that $\gamma^2_{vp_s} \gtrapprox \gamma^2_{up_s}$ at the $f_1$-tone frequency for most measurement points, which is consistent with the observations of $\gamma^2_{vp} \gtrapprox \gamma^2_{up}$ in figures 19 and 20. This finding further supports the notion

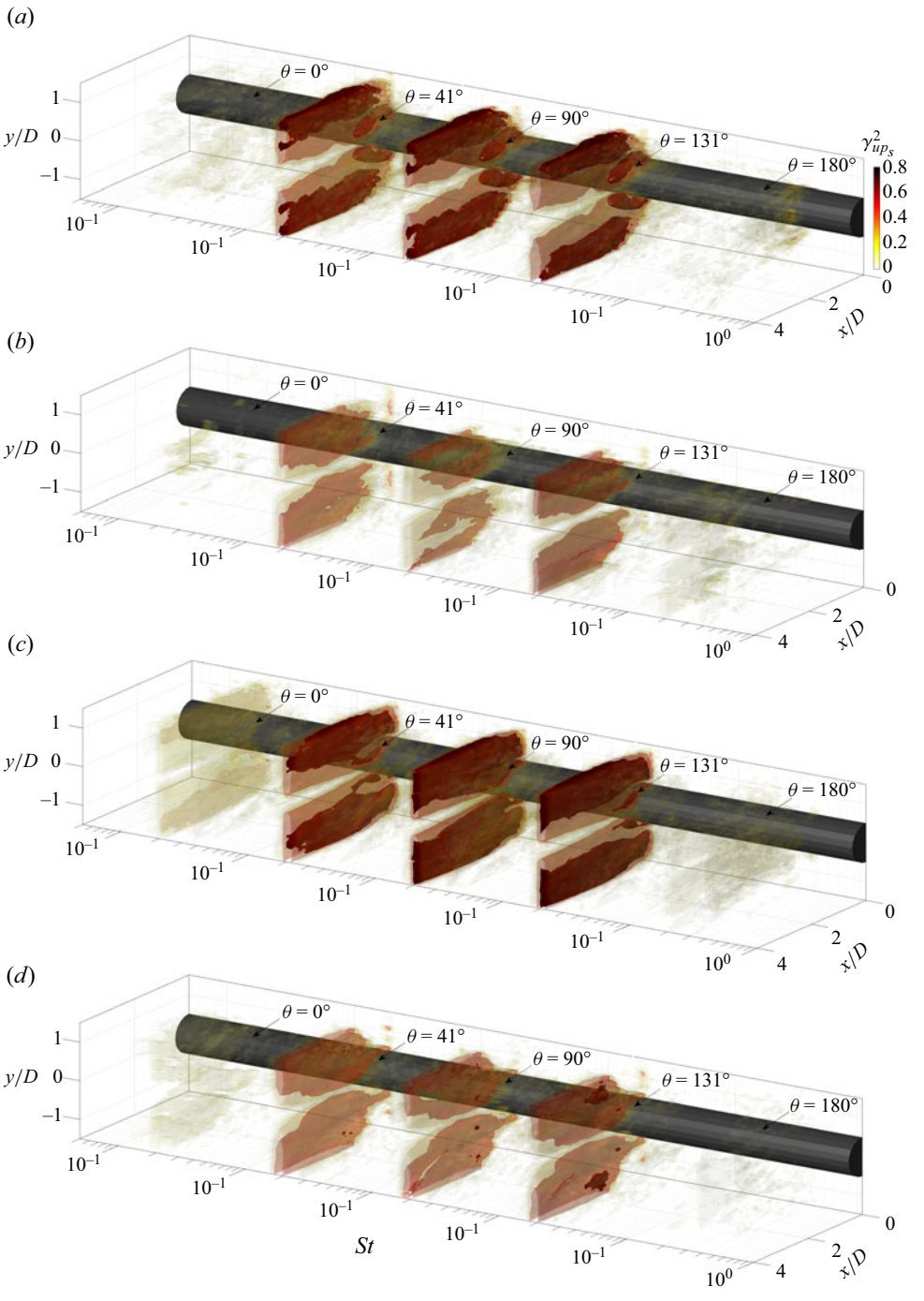


Figure 21. Isosurface of coherence between the $x$-component of velocity and near-field pressure, $\gamma^2_{up_s}$, where transparency decreases with increasing $\gamma^2_{up_s}$: (*a*) baseline; (*b*) LB41; (*c*) LB90; (*d*) LB131.

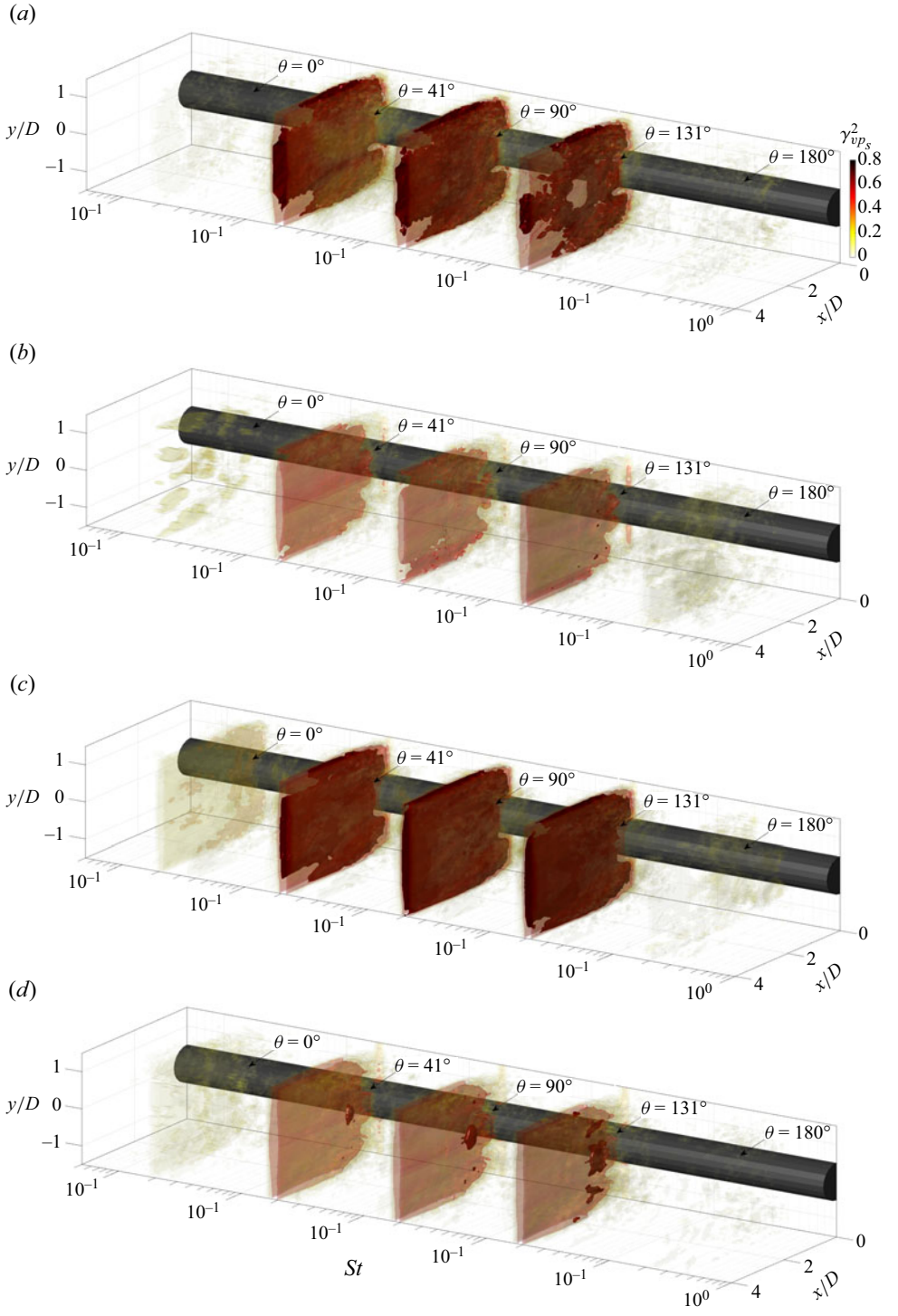


Figure 22. Isosurface of coherence between the $y$-component of velocity and near-field pressure, $\gamma^2_{vp_s}$, where transparency decreases with increasing $\gamma^2_{vp_s}$: (*a*) baseline; (*b*) LB41; (*c*) LB90; (*d*) LB131.

that vertical velocity fluctuations in the wake play a prominent role in influencing both the near-field pressure and far- field noise.

The effect of LB cases in suppressing vortex shedding manifests itself at the level of $\gamma^2_{up_s}$ and $\gamma^2_{vp_s}$ in a behaviour similar to that observed for $\gamma^2_{up}$ and $\gamma^2_{vp}$, respectively. However, at the front and rear stagnation points, especially $\theta = 0^\circ$, the $\gamma^2_{up_s}$ and $\gamma^2_{vp_s}$ of LB cases are slightly higher than those of the baseline. It is unclear, yet it can be ascribed to the effect of feedback signal on the disturbance in the shear layers on the cylinder surface which modulates the boundary layer and affects pressure fluctuations at the stagnation point to correlate with the hydrodynamic field in the wake region.

The measurements of $\gamma^2_{pp_s}$, $\gamma^2_{up_s}$, $\gamma^2_{vp_s}$, $\gamma^2_{up}$ and $\gamma^2_{vp}$ provide valuable insights into the mechanisms involved in tonal noise generation. It can be inferred that vortex shedding contributes to tonal noise through two distinct mechanisms: surface pressure fluctuations at the cylinder shoulders and the hydrodynamic field in the wake. Both mechanisms generate sound waves that can propagate to the far field, albeit with varying intensities of scattering. These findings highlight the complex nature of tonal noise generation and the role played by different components of the flow field. Comparing the results of $\gamma^2_{pp_s}$ and $\gamma^2_{vp}$ at the $f_1$-tone frequency (see figures 18 and 20), it is observed that $\gamma^2_{pp_s}$ is approximately equal to $\gamma^2_{vp}$ for the baseline case. However, for the LB cases and to some extent LB41, there is a difference where $\gamma^2_{pp_s}$ is greater than $\gamma^2_{vp}$. This indicates that the acoustic waves resulting from surface pressure fluctuations are more likely to radiate to the far field compared with those originating from the hydrodynamic field. The findings are consistent with the study conducted by Li *et al.* (2021), which emphasised that the shoulder of the cylinder plays a more significant role in sound emission than the oscillating near wake just behind the cylinder.

## 5. Proper orthogonal decomposition

### 5.1. *Proper orthogonal decomposition modes*

Proper orthogonal decomposition (POD) is employed to analyse the coherent structures in the flow and determine the most energetic fluctuations, as well as their contributions to the dominant tonal peaks in the acoustic and velocity spectra. The orthogonal basis functions constructed using POD are optimal to identify dominant coherent structures and to construct reduced-order flow models that capture the largest amount of energy with the smallest number of modes (Sirovich 1987). The POD analysis was conducted using all 5289 snapshots, following the procedure outlined by Chen *et al.* (2013). Figure 23(*a*,*b*) present the energy fraction, $\lambda_n/\Sigma\lambda_n$, and cumulative energy, $\Sigma_1^n\lambda_n/\Sigma\lambda_n$, respectively, for the first 100 modes, where $\lambda_n$ represents the eigenvalue associated with mode $n$. In all cases, the contribution of these modes to the total TKE ranges from 40 % to 60 %, as depicted in figure 23(*b*). In line with previous POD analyses conducted on wake flows with synthetic jet control (Feng, Wang & Pan 2011) and jet flows (Kirby, Boris & Sirovich 1990), the initial modes of the POD analysis capture a significant amount of energy for all cases. However, the energy contribution decreases gradually for the higher modes, ultimately approaching zero, as depicted in figure 23(*a*). Previous studies conducted by Dipankar, Sengupta & Talla (2007) and Perrin *et al.* (2007) have shown that the dominant features in the flow field are captured by the first few modes of the POD analysis, representing large-scale coherent structures. In contrast, the higher modes of the POD analysis are associated with smaller-scale turbulent structures.

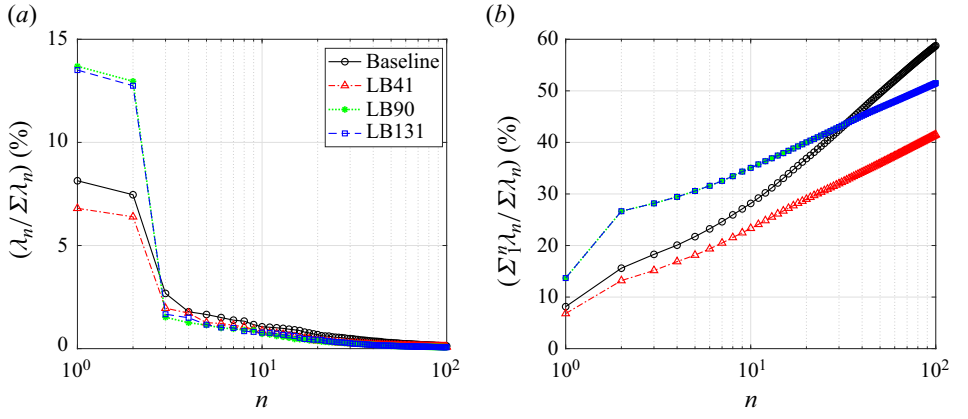


Figure 23. (*a*) Energy fraction, $\lambda_n/\Sigma\lambda_n$, and (*b*) cumulative energy, $\Sigma_1^n\lambda_n/\Sigma\lambda_n$, of the POD modes as a function of mode number, $n$, for the baseline and LB cases.

The measurement data contain temporal information that can be retrieved by the time coefficient, $c_n$, and projecting each snapshot onto the basis functions. The time coefficient indicates the correlation between the $n$th basis POD spatial mode and the instantaneous flow field. To delve deeper into the analysis of the dominant coherent structures, the energy spectra of the time coefficients, denoted as $\Phi_{cc}$ (dB Hz$^{-1}$, ref : 1 m s$^{-1}$), for the first 100 POD modes are shown in figure 24. It is observed that the spectral shapes of the first two modes exhibit remarkable similarities across all cases. In addition, a prominent tonal peak is evident at the frequency corresponding to the $f_1$-tone, which confirms that the dominant coherent structures generated during vortex shedding, specifically the large-scale Kármán vortices, capture the majority of the energy (Dipankar *et al.* 2007; Epps & Techet 2010). Based on the characteristics of the far-field noise spectra depicted in figure 5, it can be inferred that the dominant coherent structures represented by modes 1 and 2 play a significant role in the generation of far-field noise. As the mode number increases, the energy content of the turbulent structures diminishes, indicating the presence of smaller-scale turbulent structures. These structures generally exhibit a broadband behaviour in the time coefficient spectra (see figure 24*e–h*) yet for certain modes, weak but discernible tonal peaks emerge at the $f_2$- and $f_3$-tone frequencies.

From figure 24(*e–h*), it is evident that LB41 reduces the magnitude of the $f_1$-tone by approximately 6 dB compared with the baseline, while LB90 and LB131 exhibit an $f_1$-tone magnitude similar to that of the baseline ($\Phi_{cc} \approx 56$ dB). These observations seem to contradict the findings in figure 5 and indicate that the energy content of the dominant coherent structures alone is not sufficient to evaluate their contribution to far-field noise. As discussed in §§ 4.5 and 4.6, the radiating acoustic waves resulting from surface pressure fluctuations strongly outweigh those from the hydrodynamic field in the cases of LB90 and LB131. This emphasises that the role of dominant coherent structures in far-field noise generation should be assessed based on their ability to induce surface pressure fluctuations, which is influenced by the size of the vortex-formation region as discussed in § 3.2. It is important to note that the hydrodynamic field experiences rapid attenuation with distance, as demonstrated by Suzuki & Colonius (2006). This results in a weak feedback signal that has limited influence on the boundary layer modulation and disturbances in the shear layer, leading to a reduction in the energy content of surface pressure fluctuations, particularly at the $f_1$-tone frequency (refer to § 3.2). Therefore, regardless of the energy content of the dominant coherent structures, in the case of LB90, the reconstructed coherent structures of

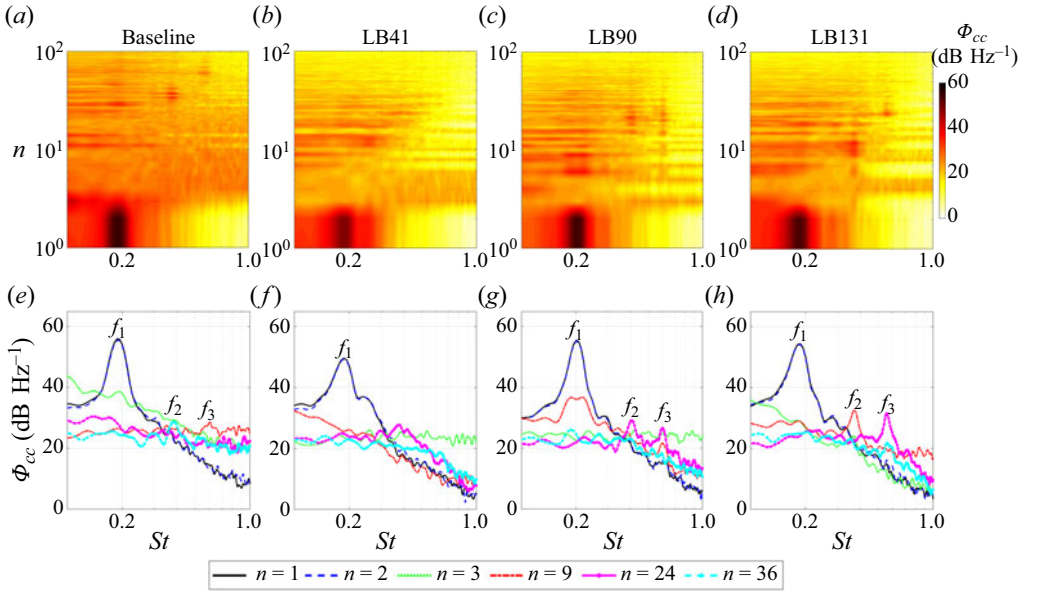


Figure 24. The PSD of the mode time coefficient, $\Phi_{cc} = 10 \log_{10} \phi_{cc}$, as a function of $St$ and mode number ($n$). The labels $f_1$, $f_2$ and $f_3$ represent the first harmonic (fundamental vortex shedding tone), second and third harmonics, respectively.

modes 1 and 2 appear near the cylinder and generate strong surface pressure fluctuations. However, for LB131, these coherent structures shed farther downstream, resulting in minimal impact on surface pressure fluctuations.

The high-frequency broadband noise observed in figure 5 may be influenced by the small-scale high-frequency fluctuations of mode 3. The energy source for these fluctuations is the large-scale coherent structures (Portela, Papadakis & Vassilicos 2020), which convect in the turbulent wake and dissipate energy. While the energy contents of the coherent and small-scale structures are of comparable magnitudes, the dissipation mechanisms for each type of motion are significantly different. Specifically, small-scale structures contribute more to energy dissipation compared with the coherent structures (Hussain 1983; Portela, Papadakis & Vassilicos 2018). In the case of LB131, where LB is applied within the separated shear layers, the small-scale structures of mode 3 convect rapidly and cause more intense energy dissipation within $St \approx 0.3$–2, which can be a mechanism for reducing high-frequency broadband noise (see figure 5). On the other hand, LB41 and LB90 are applied outside of the separated shear layers and do not stimulate the turbulent structures of mode 3 to dissipate energy effectively.

To gain a deeper understanding of the influence of coherent flow structures on near-field and far-field pressures, detailed autocorrelation and a wavelet transform are presented in figure 25. The autocorrelation determines the dominant time scales and is calculated as

$$R_{pp}(\tau) = \frac{\overline{p'(t+\tau)p'(t)}}{p_{rms}^2}, \tag{5.1}$$

where $\tau$ is the time delay and the time average is represented by the overbar.

To investigate the amplitude modulation mechanism related to the coherent flow structures generated by vortex shedding, a wavelet transform was applied to the time coefficient of mode 1, denoted as $c_1$. This analysis allows us to analyse the modulation

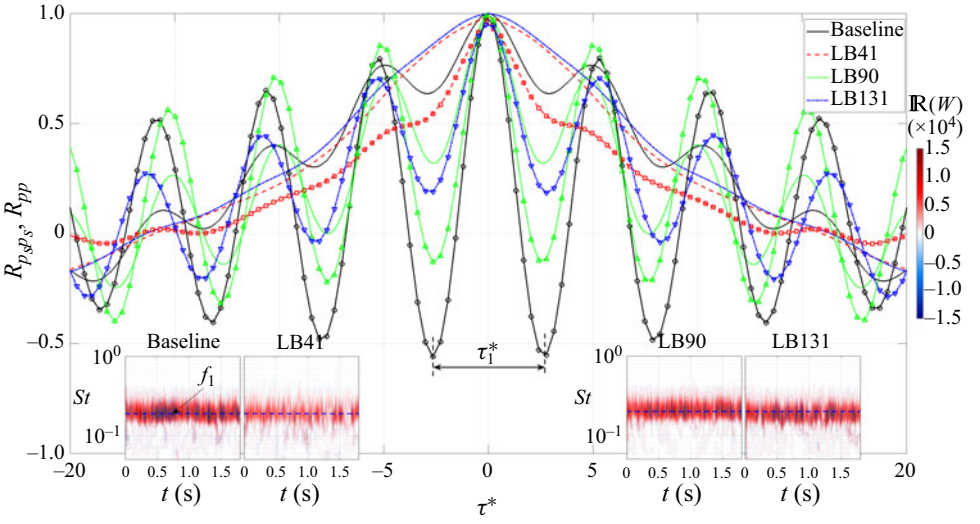


Figure 25. Autocorrelation of near-field pressure at $\theta = 90^\circ$, $R_{p_sp_s}$, and far-field pressure, $R_{pp}$, with respect to normalised time delay, $\tau^* = \tau U_\infty/D$, depicted by lines with and without symbols, respectively. The subplots present the real part of the wavelet coefficient, $\mathbb{R}(W)$, applied to the time coefficient of mode 1 ($c_1$).

of amplitudes in both the time and frequency domains simultaneously. The continuous wavelet transform, denoted as $W(a, \tau)$, was utilised in this study, with the Morlet wavelet serving as the mother wavelet (Farge 1992; Li & Nozaki 1995; Mallat 1999; Maryami *et al.* 2022*a*, 2023*c*; Maryami & Ali 2023). The wavelet transform is defined as follows:

$$W(a, \tau) = \frac{1}{\sqrt{C_\psi}} \int_{-\infty}^{+\infty} c_1(t) \psi^*_{a,\tau}\left(\frac{t-\tau}{a}\right) \mathrm{d}t, \tag{5.2}$$

where $a$ is the scale dilation parameter corresponding to the wavelet width, $\psi(t)$ is the mother wavelet, $\psi^*((t-\tau)/a)$ is the complex conjugate of the dilated and translated $\psi(t)$, and $C_\psi^{-0.5}$ is a constant that takes the mean value of $\psi(t)$.

Figure 25 presents the autocorrelation of the near-field pressure measured at $\theta = 90^\circ$ and far-field pressure, i.e. $R_{p_sp_s}$ and $R_{pp}$, respectively, as a function of normalised time delay, $\tau^* = \tau U_\infty/D$, along with time-frequency characteristics of $c_1$ extracted from the real part of the wavelet coefficient, $\mathbb{R}(W)$. For the baseline, both $R_{p_sp_s}$ and $R_{pp}$ reveal oscillations within $-20 < \tau^* < 20$ with a time delay $\tau_1^* \approx 5.2$, which is associated with the $f_1$-tone frequency of $St \approx 0.19$. In this case, $\mathbb{R}(W)$ exhibits amplitude modulation in time with multiple repetitive patches around the $f_1$-tone frequency, which indicates that the turbulent field is a superposition of coherent flow structures (Farge 1992). It is observed that $R_{p_sp_s}$ presents a strong oscillation with a weak decay rate (slow decrease of peak and trough amplitudes with respect to $\tau^*$) in comparison with $R_{pp}$, revealing the attenuation of sound pressure over a long distance before reaching the far field.

For LB90, while $\mathbb{R}(W)$ exhibits the amplitude modulation at almost the same energy level as the baseline, the periodic behaviour of $R_{p_sp_s}$ and $R_{pp}$ presents a strong oscillation with a decay rate slower than that of the baseline. This confirms that the proximity of the vortex shedding to the cylinder contributes more to strong surface pressure fluctuations and sound radiation compared with the energy content of dominant coherent flow structures. This interpretation receives further evidence by investigating $R_{p_sp_s}$, $R_{pp}$ and $\mathbb{R}(W)$ in the case of LB131. The $\mathbb{R}(W)$ for LB131 except in ranges of $t \approx 0.2$–$0.5$, $0.6$–$0.8$ and $1$–$1.3$ s

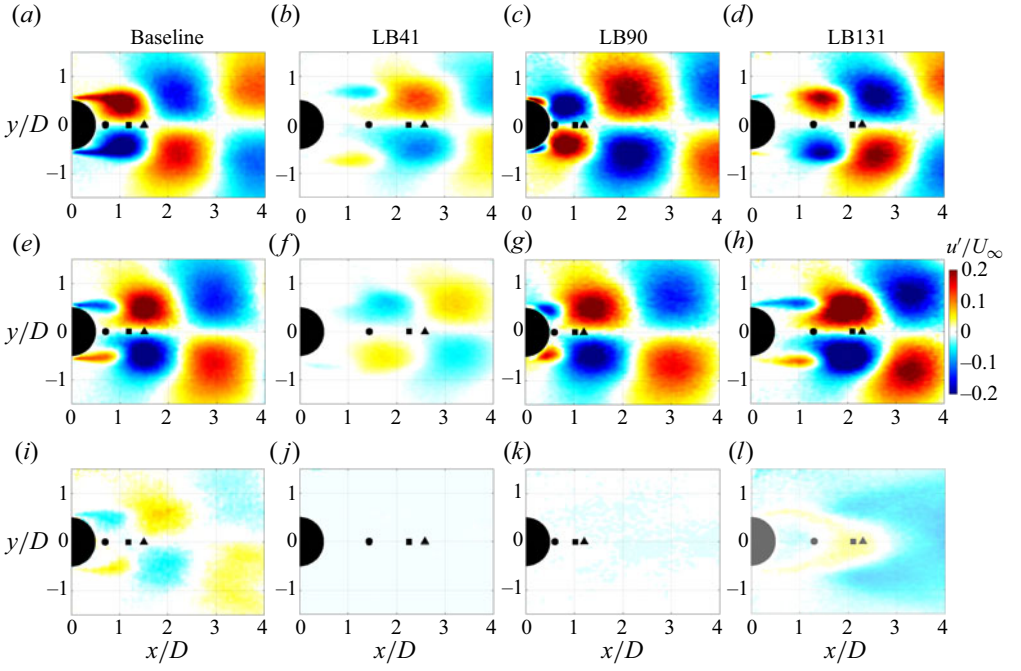


Figure 26. Flow structures corresponding to the first three POD modes ($n = 1$–3) of the $x$-component of the velocity fluctuations ($u'/U_\infty$): (*a–d*) $n = 1$; (*e–h*) $n = 2$; (*i–l*) $n = 3$. The solid circle, square and triangle symbols represent $x \approx L_{vc}$, $L_r$ and $L_f$, respectively, for each case (see figure 9).

reveals amplitude modulation with energy level similar to the baseline, but $R_{p_s p_s}$ and $R_{pp}$ are much weaker in oscillation and decay faster compared with the baseline, which is ascribed to a delay in vortex shedding (larger vortex formation size).

### 5.2. *Flow field: contributions from the POD modes*

The spatial scale of the dominant coherent structures in the wake, such as Kármán vortices, provides an indication of the overall intensity of the wake fluctuations. These coherent structures can be characterised by their size, which corresponds to the width of the wake (Qu *et al.* 2017; Duan & Wang 2021). Consistent with previous findings (van Oudheusden *et al.* 2005; Duan & Wang 2021), the first two POD modes for all cases exhibit an orthogonal relationship, as depicted in figures 26 and 27. This characteristic is evident by the coherent structures appearing with a phase shift of $\pi/2$ relative to the convection behaviour. Mode 3 exhibits turbulent structures; however, the fluctuation content is weaker compared with modes 1 and 2. The size of the coherent structures gradually expands both laterally and longitudinally as they move downstream, which is in line with the widening of the wake width (refer to figure 11) and the increased convection velocity of the vortices (Zhou & Antonia 1992).

The strength of the coherent structures diminishes and their energy dissipates in the direction of the mean flow, aligning with the decrease in TKE* observed in figure 15. This behaviour is consistent with the findings of Portela *et al.* (2020) and Hussain (1983), who demonstrated that these structures dominate the TKE in the near wake and their contribution decreases at a faster rate than the TKE associated with small-scale turbulent structures in the flow regions farther downstream. It is observed that LB41 exhibits

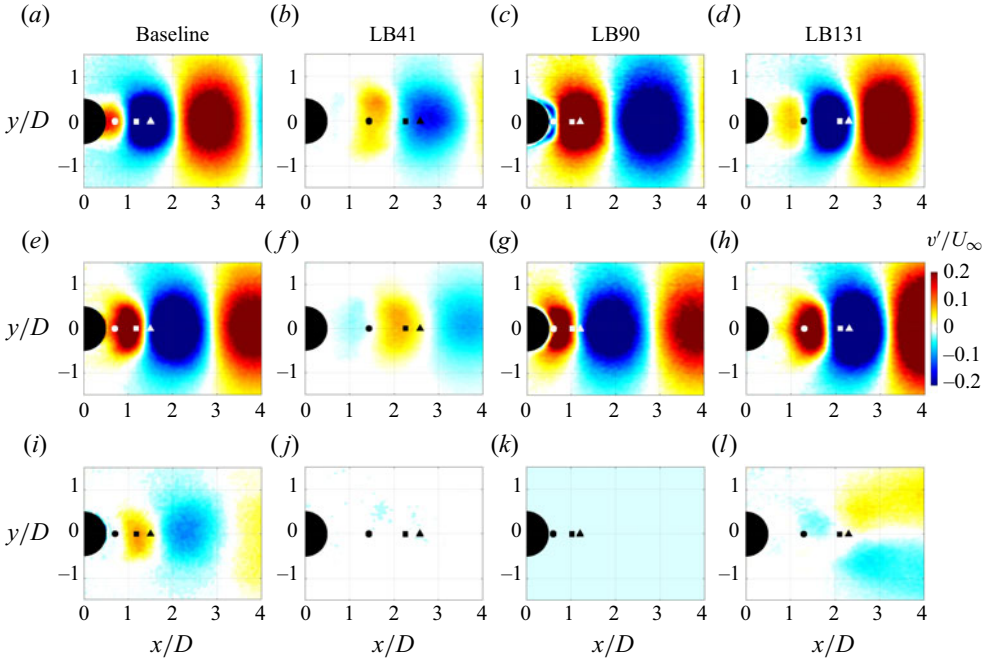


Figure 27. Flow structures corresponding to the first three POD modes ($n = 1$–3) of the $y$-component of the velocity fluctuations ($v'/U_\infty$): (*a–d*) $n = 1$; (*e–h*) $n = 2$; (*i–l*) $n = 3$. The solid circle, square and triangle symbols represent $x \approx L_{vc}$, $L_r$ and $L_f$, respectively, for each case (see figure 9).

significantly lower energy content in its coherent structures compared with the baseline, which can be attributed to its larger vortex formation size. Consequently, these structures do not contribute much to the TKE near the cylinder, consistent with the observations in figure 15(*b*). On the other hand, for LB90, the coherent structures have a similar energy content to the baseline but appear closer to the cylinder due to the accelerated rolling up of the shear layers. In the case of LB131, the energy level of the coherent structures is also comparable to the baseline, but due to the stretching of the shear layers, these structures are pushed farther downstream. These observations provide further evidence that the proximity of vortex shedding to the cylinder or the size of the vortex-formation region plays a crucial role in attenuating TKE near the cylinder, as well as near-field pressure and acoustic noise. Furthermore, it is evident that each LB case undergoes a specific vortex-shedding mechanism. This is particularly apparent when comparing LB41 and LB131, where both cases result in a larger vortex formation region compared with the baseline, but the energy content of the coherent structures differs significantly.

### 5.3. *Instantaneous flow field: contributions from the POD modes*

The time history of the first POD mode time coefficient, $c_1$, of the baseline normalised using its corresponding eigenvalue, $\lambda_1$, is presented in figure 28(*a*) in terms of the normalised time, $t^* = tU_\infty/D$, to investigate the contributions of coherent flow structures to vortex shedding. The time history is characterised by oscillation at the $f_1$-tone frequency with small-amplitude modulation. The $t_0^* - t_8^*$ labels indicate the instants of two sets of consecutive vortex shedding. The peak-to-peak distance between two successive minima

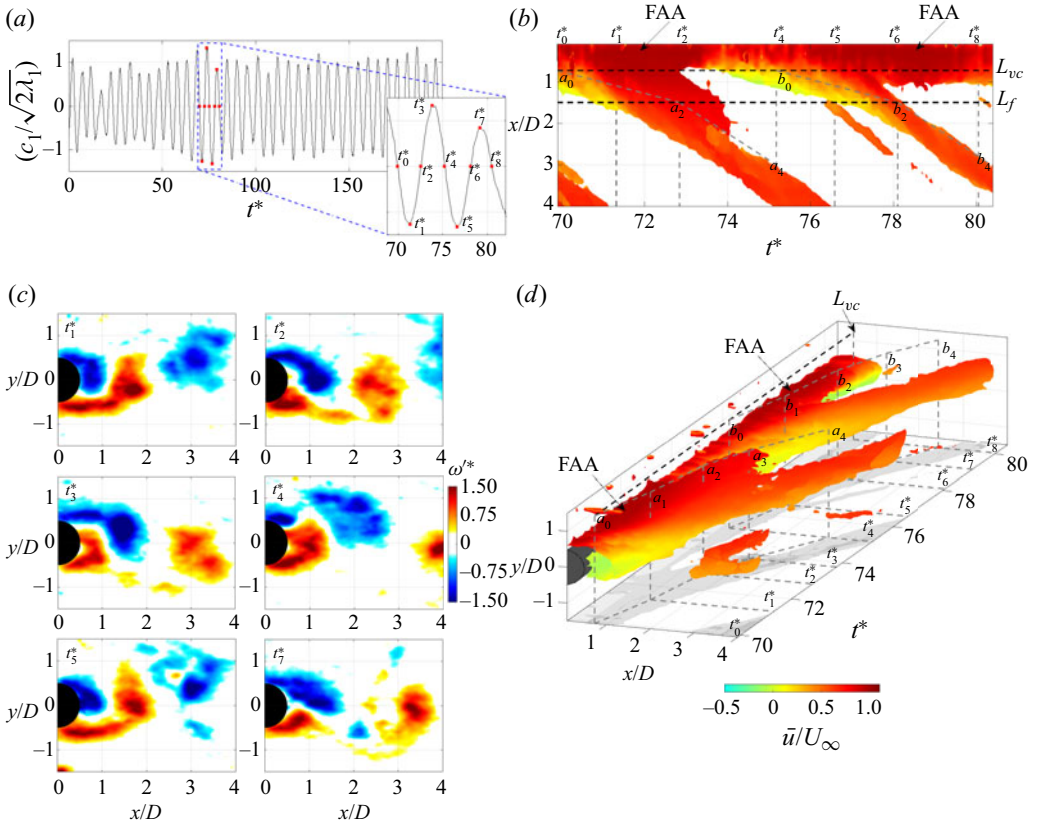


Figure 28. (*a*) Time history of the first POD mode time coefficient, $c_1$, of the baseline, normalised using its corresponding eigenvalue, $\lambda_1$. The red square markers superimposed on the $c_1/\sqrt{2\lambda_1}$-curve correspond to the instances of two sets of consecutive vortex shedding. The instants are presented using the normalised time, $t^* = tU_\infty/D$, from $t_0^*$ to $t_8^*$. (*b*,*d*) Isosurface of normalised instantaneous vorticity, $\omega'^* = -0.7$, coloured by $\bar{u}/U_\infty$. The black dashed lines represent $x \approx L_{vc}$ and $L_f$, and the dashed grey lines illustrate the movement trajectory of the vortices within $a_0$–$a_4$ and $b_0$–$b_4$. (*c*) Flow fields of $\omega'^*$ for consecutive instants within $t_1^*$–$t_7^*$. The $x$-positions of the vortices at each instant of the first and second sets of shedding are denoted by $a_0$–$a_4$ and $b_0$–$b_4$, respectively. These positions are extracted from (*c*) and figure 9 or table 3.

or maxima of the turbulent fluctuation of $c_1/\sqrt{2\lambda_1}$ within $t_0^*$–$t_8^*$ relates to the $f_1$-tone frequency.

The normalised instantaneous vorticity, $\omega'^* = \omega_z' D/U_\infty$, in the instant range of $t_1^*$–$t_7^*$ is displayed in figure 28(*c*), where the shear layers are visible on both sides of the cylinder and roll up into vortices in the wake. At $t_1^* \approx 71$, the shear layer coming from the top side of the cylinder entrains into the growing shear layer of the other side of the cylinder. This entrainment process continues for a quarter of the main tone period up to $t_2^* \approx 72.5$, corresponding to $c_1/\sqrt{2\lambda_1} = 0$. While not shown in figure 28(*c*) for brevity, the entrainment process actually begins at $t_0^* \approx 70$ and becomes strong within $t_1^*$–$t_2^*$. At the beginning of the second quarter ($t_2^*$), the concentrated vortices in the tail of the longer shear layer separate from the shear layer and convect downstream into a vortex. During the second quarter up to instant $t_3^* \approx 74$, a vortex with vorticity of opposite sign subsequently develops by circulation from the shear layer on the top side of the cylinder until it becomes

strong enough to draw the fluid from the other shear layer across the wake. The entrainment of the shear layer coming from the bottom side of the cylinder continues up to $t_4^* \approx 75$, when the third quarter ends, and then the vortex detaches from the shear layer to facilitate the vortex growth in the fourth quarter for the next vortex shedding. The corresponding flow field at instant $t_5^*$ appears similar to instant $t_1^*$ in terms of the vortex shedding process. At instant $t_7^*$, the shed vortex continues travelling downstream in a behaviour similar to that at instant $t_3^*$.

The instantaneous flow field in figure 28(*c*) clearly shows that the first POD mode is ascribed to the periodic vortex shedding at the $f_1$-tone frequency. Furthermore, the vortex with high energy content is being shed from the cylinder at the stage, when the entrainment of fluid-bearing vorticity from the other shear layer cuts off the further supply of circulation to the vortex, which then ceases to increase in strength. In line with the findings in figures 26 and 27 and the results presented by Portela *et al.* (2020), this implies that the vortex becomes weaker in terms of the energy content after shedding. It is observed in figure 28(*c*) that the vortex tends to separate from the shear layer at $x \approx L_f$.

The time–space evolution of the vortices with a negative vorticity sign fed by circulation from the shear layer on the top side of the cylinder in the instant range of $t_0^*$–$t_8^*$ is presented in figure 28(*b*,*d*). The vorticity is coloured by $\bar{u}/U_\infty$. The location of vortices corresponding to each instant is approximately marked by $a_0$–$a_4$ and $b_0$–$b_4$ for the first and second sets of vortex shedding, respectively. The travelling trajectory of the vortices between these locations is presented by dashed grey lines and their slope can be an estimate of the convective velocity of the vortices ($U_c$). Interestingly, the velocity magnitude $U_c$ in the vortex-formation region between $a_0$ ($x/D \approx 0.75$, $t^* \approx 70$) and $a_2$ ($x/D \approx 1.5$, $t^* \approx 72.8$) is approximately four tenths of that outside the vortex-formation region between $a_2$ and $a_4$ ($x/D \approx 3$, $t^* \approx 75$), with values of $U_c \approx 0.27U_\infty$ and $0.68U_\infty$, respectively. This confirms that the entrainment process decreases the $U_c$ of the vortices and the opposite takes place after shedding, which is consistent with Zhou & Antonia (1992). From figure 28(*b*,*d*), it can be seen that the evolution of vorticity in the shear layer is accompanied by the development of the FAA up to $x \approx L_{vc}$, which is consistent with the observations in figure 8(*a*).

The evolution of the vortices with a negative vorticity sign in time–space domains for the LB cases is presented in figure 29. It is observed for each LB case except LB90 that the circulation from the shear layer originating from the flow separation on the top side of the cylinder continues to shed vortices farther downstream in comparison with the baseline. This is confirmed by the time–space evolution of $\omega'^*$ within $t_1^*$–$t_4^*$ as presented in figure 30. It is evident that, for LB41 and LB90, initially, the shear layer from the bottom side of the cylinder is entrained by the one coming from the top side of the cylinder within this time range. This behaviour is opposite to that observed for the baseline (see figure 28*c*) and LB131. This indicates that vortex shedding in LB41 and LB90 occurs with a noticeable phase shift compared with LB131.

### 5.4. *Discussion on flow and noise control mechanism*

Vertical velocity fluctuations significantly contribute to vortex shedding (see figure 17), generating large-scale coherent flow structures with high energy content as depicted in figure 27. Both Reynolds stress and TKE are primarily governed by these vertical velocity fluctuations (see figures 13 and 15, respectively). They play a crucial role in directly scattering acoustic waves to the far field (quadrupole source) (see figure 20) and, notably, in imposing pressure fluctuations on the cylinder surface, specifically at the shoulders of the cylinder, as depicted in figure 22. These surface pressure fluctuations have a more

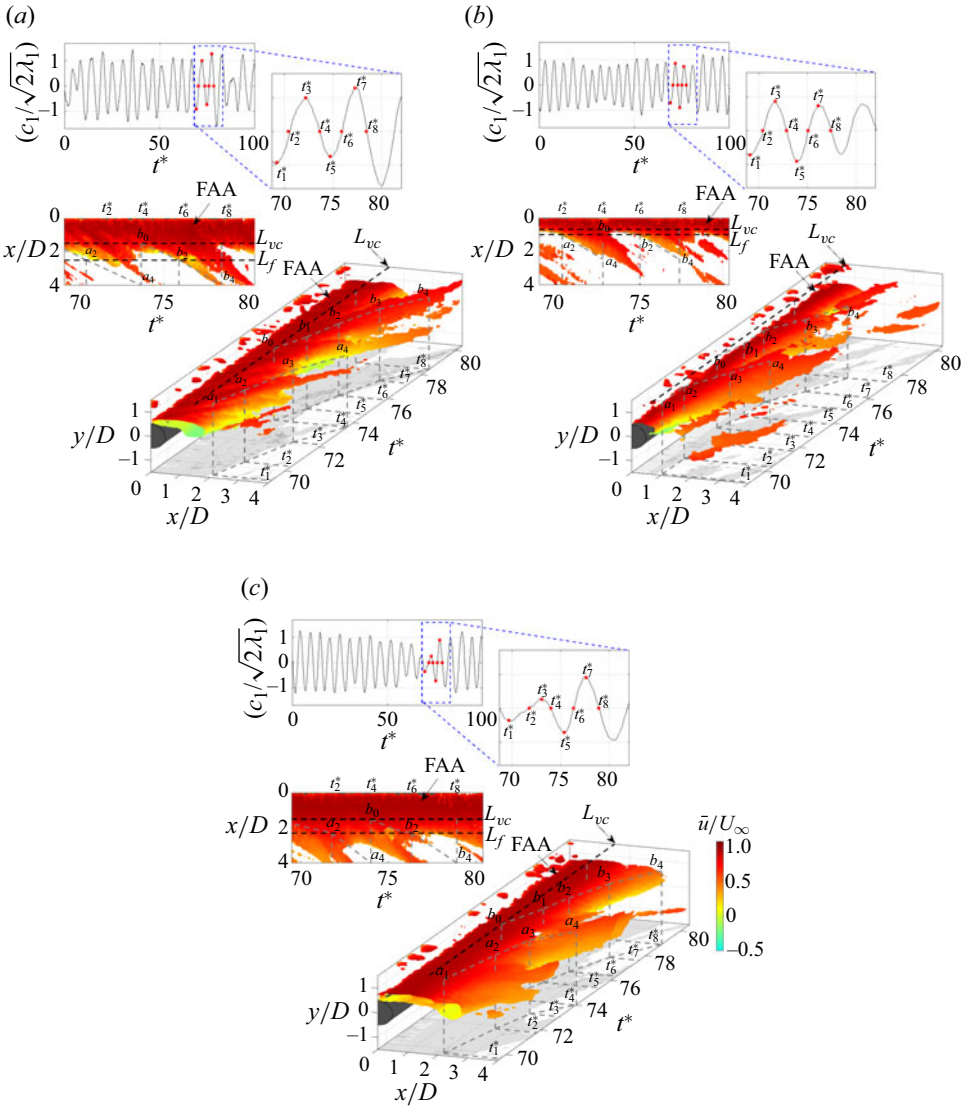


Figure 29. Time history of the first POD mode time coefficient normalised by its eigenvalue, $c_1/\sqrt{2\lambda_1}$, and isosurface of $\omega'^* = -0.7$ coloured by $\bar{u}/U_\infty$. The red square markers superimposed on the $c_1/\sqrt{2\lambda_1}$-curve correspond to the instances of two sets of consecutive vortex shedding from $t_1^*$ to $t_8^*$. The $x$-positions of the vortices at each instant of the first and second shedding sets are denoted by $a_1$–$a_4$ and $b_0$–$b_4$, respectively. These positions are extracted from figure 9 or table 3. The black dashed lines represent $x \approx L_{vc}$ and $L_f$, and the dashed grey lines depict the movement trajectory of the vortices within $a_1$–$a_4$ and $b_0$–$b_4$. Here (*a*) LB41; (*b*) LB90; (*c*) LB131.

pronounced impact on far-field noise (dipole source) (see figure 18), outweighing the influence of the velocity field as shown in figure 20. Taking these insights into account, it becomes evident that the size of the vortex-formation region, especially along the streamwise direction, stands as the primary mechanism influencing vortex-induced noise in a circular cylinder. Delaying vortex shedding through the application of LB techniques, such as LB41 and LB131, leads to the elongation of shear layers before they roll up into vortices. This elongation results in an expansion of the vortex formation region farther

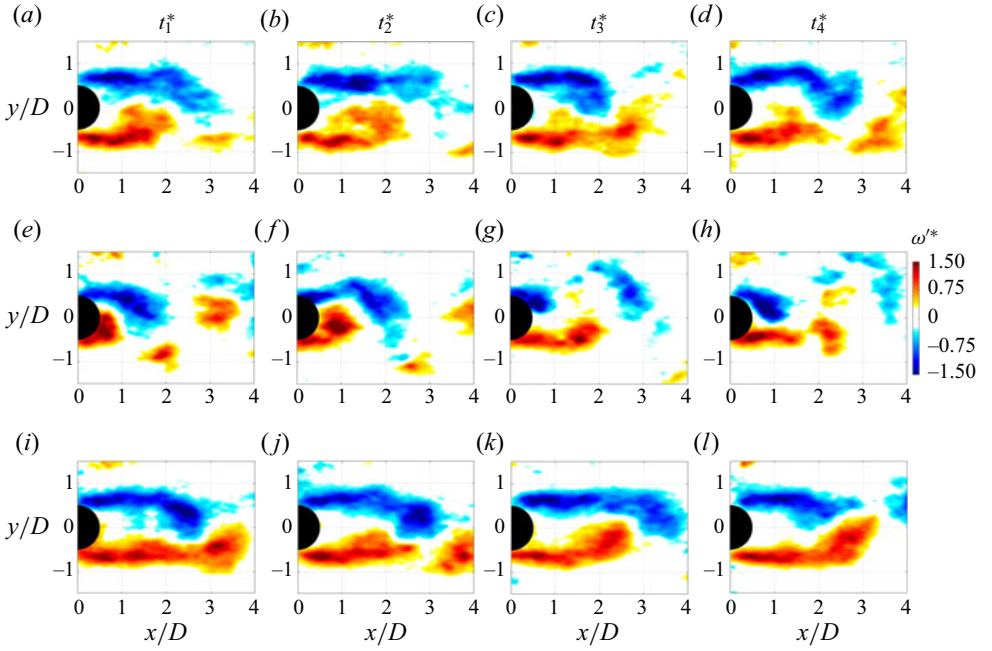


Figure 30. Flow fields of $\omega'^*$ at consecutive instants within $t_1^*$–$t_4^*$ extracted from the time history of the first POD mode time coefficient (see figure 29): (*a–d*) LB41; (*e–h*) LB90; (*i–l*) LB131.

downstream (see figures 8 and 12, or 28–30) and a wider region close to the cylinder, as illustrated in figure 11. Consequently, the vertical flow movement near the cylinder slows down (see figures 10 and 14), resulting in dissipation of TKE (see figure 15) and suppression of pressure fluctuations at the shoulders of the cylinder as shown in figure 6. This, in turn, leads to weaker scattering of acoustic waves to the far field (see figure 5).

As the approach of opposite-signed vorticity in sufficient concentration detaches the vortex from the shear layer as shown in figure 30, it can be deduced that the entrainment into the shear layer can be a basic mechanism determining the size of the vortex-formation region. This is consistent with the findings of Gerrard (1966), who reported that an increase of turbulence in the shear layers results in their being more diffused in the region of interaction. When the shear layers are diffused, it takes longer for a sufficient concentration of vorticity to be carried across the wake and initiate shedding. The greater diffusion of vorticity will result in less entrainment into the shear layer, and hence a larger vortex-formation region. In this case, there will be an effective cancellation of circulation in the interior of the formation region, which is consistent with the suppression of TKE and Reynolds stress. Gerrard (1966) also demonstrated that the fluid drawn across the wake by the action of the growing vortex on the other side is partly entrained by the growing vortex and partly by the shear layer upstream of the growing vortex. The reverse flow is some part of this fluid-bearing opposite-signed vorticity which will find its way into the interior of the formation region. The size of the formation region is determined by the balance between entrainment into the shear layer upstream of the growing vortex and the replenishing of fluid by the induced reverse flow. Hence, when the shear layers become longer and less entrainment occurs, it is typically associated with an increase in reverse flow. In § 3.2, the role of wake vorticity dynamics in modulating the boundary layer through self-excitation cycles was emphasised. Initial disturbances provided by these dynamics amplify spatially

within separated shear layers, eventually forming fully developed vortices in the wake. As a result, a weak feedback signal delays disturbance amplification to a saturation level, leading to an enlargement of the vortex-formation region.

It is anticipated that each LB case, except for LB90, has the potential to increase turbulence in the shear layers and promote their diffusion. We distinguish between two stages of the shear layer: the turbulent spreading stage and the fully developed turbulent stage. During the turbulent spreading stage, the shear layer expands due to turbulent diffusion driven by turbulent eddies and fluctuations. This initial stage is characterised by high turbulence intensity and Reynolds stresses as turbulent mixing processes dominate. In contrast, the fully developed turbulent shear layer represents a quasisteady state where the turbulent mixing processes have reached a balance. At this stage, statistical properties such as turbulence intensity and Reynolds stresses become effectively averaged over time as shown in figure 13. The fully developed turbulent shear layer exhibits a more stable and controlled turbulent structure with well-defined statistical properties. Therefore, it is possible that certain LB techniques boost turbulence in the shear layer during the turbulent spreading stage, which leads to a reduction in the averaged statistical properties of the fully developed turbulent flow.

In the case of LB41, where blowing is applied approximately within the boundary layer, the external perturbations generated by the blowing amplify the boundary layer instabilities, leading to a delayed separation compared with the baseline. Since all vorticity must be generated at solid boundaries after separation and then transported to the flow domain by diffusion and convection, any delay in separation by LB41 increases vorticity flux specifically at the top and bottom sides of the cylinder. As a result, the turbulence in the separated shear layers increases, causing them to become more diffused. This is supported by the convection velocity of $U_c \approx 0.45U_\infty$ between $b_0$ and $b_2$, as depicted in figure 29(*a*), which exceeds the corresponding value of the baseline. The increased turbulence and diffusion in the shear layers result in reduced entrainment and a delay in vortex shedding as depicted in figure 30(*a–d*). While it is difficult to precisely determine the specific contributions of fluid entrainment by the growing vortex and the shear layer upstream of the growing vortex to the overall fluid entrainment, it can be speculated that there is a notable decrease in the latter, as indicated by an increase in reverse flow observed in figure 9. In the case of LB41, the presence of a larger vortex formation region leads to a weaker feedback signal being transmitted to the cylinder. This is in line with a relatively weak boundary layer modulation and a delay in the amplification of disturbances within the shear layer and fully formed vortices.

In the case of LB90, where blowing is applied perpendicular to the free stream, the uplift momentum is enhanced on the top and bottom sides of the cylinder. This leads to a stronger counterflow and displaces the disturbances in the shear layers on the cylinder to higher surface-normal positions compared with the baseline. This enhanced counterflow can effectively prevent the boundary layer from separating and delay the separation point farther downstream even compared with LB41. This, however, leads to decreased turbulence and diffusion in the shear layers, causing them to come closer together and facilitating their interaction as illustrated in figure 30(*e–h*). This is accompanied by a convection velocity of $U_c \approx 0.14U_\infty$ within $b_0$–$b_2$ (see figure 29*b*), which is notably smaller than that of the baseline. As a result, the size of the vortex formation region is decreased to balance the high fluid entrainment. The observations in figure 9, however, indicate that there is an increase in reverse flow in the case of LB90 compared with the baseline, which suggests that there is also a decrease in entrainment into the shear layer upstream of the growing vortex. To explain this discrepancy, it can be hypothesised that

LB90 experiences a notable increase in fluid entrainment by the growing vortex, which in turn has an impact on the overall entrainment process. For LB90, the close rolling up of the vortices to the cylinder generates a strong feedback signal that influences the cylinder. This leads to boundary layer modulation and the spatial amplification of disturbances in the separated shear layers. As a result, there is an acceleration in the formation and shedding of vortices.

By inspecting figure 29(*c*), it can be observed that the convection velocity of LB131 within $b_0$–$b_2$ is $U_c \approx 0.34U_\infty$, which is slightly higher than that of the baseline. Furthermore, figure 9 shows that the reverse flow in this LB case is similar to the value observed for the baseline. These results suggest that the shear layers may not exhibit significant turbulence and diffusion, and the entrainment into the shear layers upstream of the growing vortex is likely similar to that of the baseline. However, similar to LB41, LB131 demonstrates vortex shedding that occurs farther downstream compared with the baseline (see figure 30*i–l*). This discrepancy provides further confirmation of the existence of a distinct vortex-shedding mechanism when blowing is applied on the windward and leeward sides of the cylinder. Assuming that the flow discharge into the shear layers in the case of LB131 resembles a vortex-shedding mechanism commonly observed in porous materials, it can be inferred that the boundary layer separation is delayed compared with the baseline but not significantly deviated from it. As a result, the shear layers are likely to exhibit turbulence and diffusion levels similar to those of the baseline, particularly just upstream of the growing vortex. However, the direct interaction between the blowing vortices and the disturbances in the separated shear layers promotes turbulence and diffusion within the growing vortex. Therefore, the fluid entrainment by the shear layer upstream of the growing vortex is expected to be similar to that of the baseline, which balances with less entrainment by the growing vortex, resulting in a farther downstream shift in vortex shedding. The larger vortex-formation region produces a relatively weak feedback signal to the cylinder, leading to a weak boundary layer modulation and a delay in the amplification of disturbances in the separated shear layers. Unlike LB41, the entrainment process in the case of LB131 appears to be more complex, resulting in the generation of recirculation bubbles that do not exhibit strong attachment between their forehead and rear side of the cylinder, as depicted in figure 8. The unique vortex dynamics observed in LB131 significantly impact far-field noise, resulting in a reduction in broadband spectral content compared with LB41.

## 6. Summary and conclusions

Active control of the flow-induced noise of a circular cylinder using LB was investigated experimentally in an anechoic wind tunnel. The LB was applied using a series of specially designed chambers along the $7D$ span of the cylinder at three peripheral angles of $\theta_b = \pm 41^\circ$ (LB41), $\pm 90^\circ$ (LB90) and $\pm 131^\circ$ (LB131) to manipulate the boundary layer, the region near the separation point of the boundary layer and separated shear layers, respectively. Hence, these symmetrically arranged LB cases, operating at a relatively high Reynolds number of $Re = 7 \times 10^4$, allowed for the manipulation of 3-D flow structures over a considerable spanwise length, filling the gaps in the existing literature. A highly instrumented cylinder with several pressure taps at different peripheral locations was used to measure surface pressure fluctuations in synchronisation with far-field noise and flow velocity for the first time. To gain qualitative insights into the flow field behaviour in the wake of the cylinder under the influence of LB cases, planar PIV was employed. A detailed summary of the findings in this study follows the schematic diagram presented in figure 31.

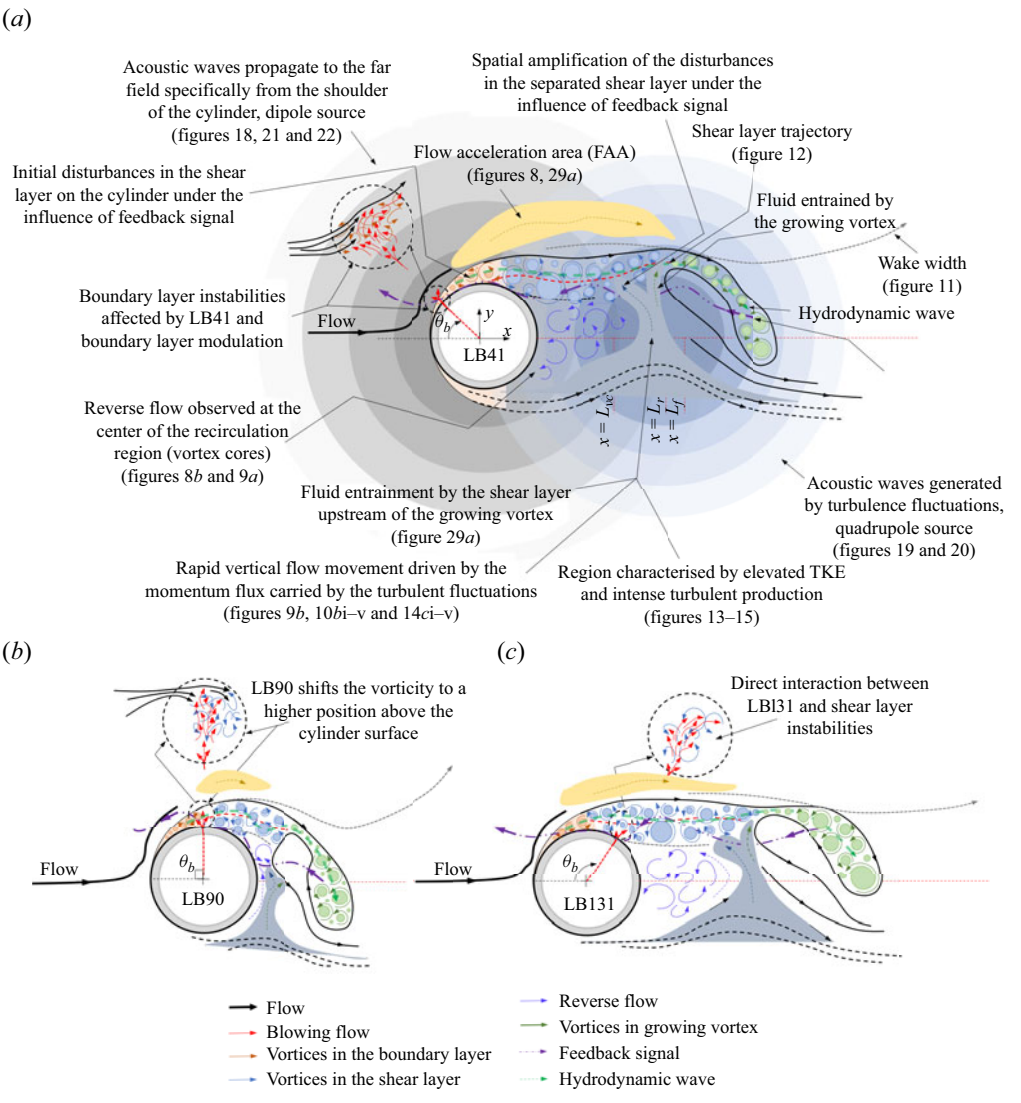


Figure 31. Schematic diagram illustrating the key flow characteristics influenced by the LB cases.

The emergence of tonal noise at the $f_1$-tone frequency ($St \approx 0.19$) was clearly observed for each LB case, and therefore none of the LB techniques investigated here can fully suppress the vortex shedding noise generation. Despite this, a superior $f_1$-tone reduction of approximately 19 dB was observed when LB is applied at $\theta_b = \pm 41^\circ$, i.e. in the boundary layer. In contrast, the application of LB at $\theta_b = \pm 90^\circ$, i.e. downstream from the point of boundary layer separation, increased the $f_1$-tone magnitude by approximately 3 dB from the baseline. These observations were further supported by the near-field pressure taken around the circumference of the cylinders, specifically in the preseparation and postseparation regions. Analysis of the near- to far-field coherence demonstrated that the pressure fluctuations in these regions significantly contributed to the tonal noise. Therefore, any change in the $f_1$-tone provided by LB cases was attributed to variations in surface pressure fluctuations.

Time-average flow fields revealed a significant vertical flow movement within $L_{vc} \lessapprox x \lessapprox L_r$–$L_f$ for each case, which is due to the interaction between the shear layers when the high-momentum fluid enters the wake from the free stream. The rapid vertical flow movement plays a significant role in the process of fluid entrainment for vortex shedding, as well as in the generation of TKE and shear stress. The coherence between velocity and near-field pressure revealed that this flow movement is particularly influential in generating alternating pressure pulses on both sides of the cylinder surface specifically at the shoulders, which are the source of lift fluctuations and acoustic waves. It was demonstrated that the vortex must grow in the shear layer under the influence of streamwise velocity fluctuations to shed as it draws the fluid from the other shear layer across the wake. However, the hydrodynamic field responsible for generating the $f_1$-tone derives a substantial portion of its energy from vertical velocity fluctuations. The coherence between velocity and far-field noise underscored that these fluctuations play a significant role in the generation and propagation of acoustic waves, allowing the energy associated with the $f_1$-tone to propagate into the far field from any location within the wake. However, the near-field pressure fluctuations at the shoulders of the cylinder were found to have a more pronounced impact on the acoustic waves radiated to the far field compared with the hydrodynamic field.

The instantaneous flow fields extracted from POD analysis showed that most of the energy is concentrated in the dominant coherent structures produced during vortex shedding at the $f_1$-tone frequency. Furthermore, the shedding of the vortex with high energy content occurs at the stage when the entrainment of fluid-bearing vorticity from the other shear layer cuts off the further supply of circulation to the vortex (see figure 31), which then ceases to increase in strength. Hence, the size of the vortex-formation region is primarily determined by a balance between the entrainment into the growing vortex, the shear layer upstream of the growing vortex and the replenishment of the interior of the formation region by reverse flow. When the vortex shedding occurs, a feedback signal causes disturbances in the shear layer on the cylinder which modulates the boundary layer. It then follows with spatial amplification of the disturbances in the separated shear layers for fully formed vortices and starts a new vortex-shedding cycle.

The analysis of POD revealed that all LB cases, except LB90, have the ability to expand the vortex-formation region through distinct mechanisms as shown in figure 31. These LB cases demonstrated the potential to enhance turbulence in the shear layers by increasing the convective velocity, thereby causing greater diffusion of the flow. As a consequence, the increased diffusion leads to reduced overall fluid entrainment, resulting in a larger vortex-formation region. In this scenario, the region of high-momentum transfer extends towards the downstream region, leading to an effective cancellation of circulation within the interior of the vortex-formation region. This cancellation aligns with the observed suppression of TKE, Reynolds stress and surface pressure fluctuations, which are the primary mechanisms contributing to tonal noise generation. It was argued that the boundary layer instabilities will delay the separation when LB41 manipulates the boundary layer (see figure 31*a*). As vorticity is primarily generated at solid boundaries after separation and subsequently transported into the flow domain through diffusion and convection, the delay of separation induced by LB41 results in an increased vorticity flux, particularly at the top and bottom sides of the cylinder. Consequently, the separated shear layers become more diffused and elongated along the flow direction, which leads to the shedding of vortices farther downstream. Due to the perpendicular application of LB90 to the free stream as depicted in figure 31(*b*), it was found that this LB technique has the potential to displace the instabilities in the shear layer on the cylinder to a higher position

above the cylinder surface. As a result, the shear layers exhibit reduced turbulence and diffusion, and they come closer to each other, promoting their interaction. In order to balance the entrainment flows, the size of the formation region decreases, causing the vortices to roll up closer to the cylinder. In the case of LB131 as depicted in figure 31(*c*), it was inferred that the direct interaction between the LB vortices and the instabilities in the separated shear layers plays a crucial role in increasing the turbulence and diffusion within the shear layers. This mechanism can be likened to the bleeding of internal flow from a porous layer into the near-wake region, effectively pushing the vorticity region farther downstream.

Incorporating spanwise analysis is crucial for a comprehensive understanding of the 3-D nature of the flow field surrounding a circular cylinder. Future studies should prioritise spanwise analysis to explore how the spanwise coherence length varies under different conditions, including cases with and without blowing. Additionally, investigating the interaction between adjacent vortices in the spanwise direction will provide valuable insights into the characteristics of near-field pressure and far-field noise.

**Funding.** This research was supported by the National Natural Science Foundation of China (grant nos. 12111530102 and 12272163), Department of Science and Technology of Guangdong Province (grant no. 2023B1212060001) and the Natural Science Foundation of Shenzhen Municipality (Stable Support Plan Program, grant no. 20220814230752003).

**Declaration of interests.** The authors report no conflict of interest.

**Author ORCIDs.**
Reza Maryami https://orcid.org/0000-0003-1201-5595;
Elias J.G. Arcondoulis https://orcid.org/0000-0002-3791-395X;
Yu Liu https://orcid.org/0000-0003-1112-1863.

## References

ACHENBACH, E. 1968 Distribution of local pressure and skin friction around a circular cylinder in cross-flow up to $Re = 5 \times 10^6$. *J. Fluid Mech.* **34** (4), 625–639.

ANGLAND, D., ZHANG, X. & GOODYER, M. 2012 Use of blowing flow control to reduce bluff body interaction noise. *AIAA J.* **50** (8), 1670–1684.

BEARMAN, P.W. 1967 The effect of base bleed on the flow behind a two-dimensional model with a blunt trailing edge. *Aeronaut. Q.* **18** (3), 207–224.

BENARD, N., BALCON, N., TOUCHARD, G. & MOREAU, E. 2008 Control of diffuser jet flow: turbulent kinetic energy and jet spreading enhancements assisted by a non-thermal plasma discharge. *Exp. Fluids* **45** (2), 333–355.

BEVILAQUA, P.M. 1973 *Intermittency, The Entrainment Problem*. Purdue University.

BOUAK, F. & LEMAY, J. 1998 Passive control of the aerodynamic forces acting on a circular cylinder. *Expl Therm. Fluid Sci.* **16** (1–2), 112–121.

CASALINO, D. & JACOB, M. 2003 Prediction of aerodynamic sound from circular rods via spanwise statistical modelling. *J. Sound Vib.* **262** (4), 815–844.

CHAUHAN, M.K., DUTTA, S., MORE, B.S. & GANDHI, B.K. 2018 Experimental investigation of flow over a square cylinder with an attached splitter plate at intermediate Reynolds number. *J. Fluids Struct.* **76**, 319–335.

CHEN, H., REUSS, D.L., HUNG, D.L.S. & SICK, V. 2013 A practical guide for using proper orthogonal decomposition in engine research. *Intl J. Engine Res.* **14** (4), 307–319.

CHEN, W.-L., HUANG, Y., CHEN, C., YU, H. & GAO, D. 2022 Review of active control of circular cylinder flow. *Ocean Engng* **258**, 111840.

CHEN, W.-L., LI, H. & HU, H. 2014 An experimental study on a suction flow control method to reduce the unsteadiness of the wind loads acting on a circular cylinder. *Exp. Fluids* **55** (4), 1–20.

CHOI, H., JEON, W.-P. & KIM, J. 2008 Control of flow over a bluff body. *Annu. Rev. Fluid Mech.* **40**, 113–139.

CHOMAZ, J.M., HUERRE, P. & REDEKOPP, L.G. 1988 Bifurcations to local and global modes in spatially developing flows. *Phys. Rev. Lett.* **60** (1), 25.

CURLE, N. 1955 The influence of solid boundaries upon aerodynamic sound. *Proc. R. Soc. Lond.* A **231** (1187), 505–514.

DELAUNAY, Y. & KAIKTSIS, L. 2001 Control of circular cylinder wakes using base mass transpiration. *Phys. Fluids* **13** (11), 3285–3302.

DENG, Z., GAO, D., CHEN, G. & CHEN, W.-L. 2021 Active wake control of flow past a circular cylinder with slot jet. *J. Aerosp. Engng* **34** (4), 04021033.

DIPANKAR, A., SENGUPTA, T.K. & TALLA, S.B. 2007 Suppression of vortex shedding behind a circular cylinder by another control cylinder at low Reynolds numbers. *J. Fluid Mech.* **573**, 171–190.

DONG, S., TRIANTAFYLLOU, G.S. & KARNIADAKIS, G.E. 2008 Elimination of vortex streets in bluff-body flows. *Phys. Rev. Lett.* **100** (20), 204501.

DOOLAN, C.J. 2009 Aeroacoustic simulation of bluff body noise using a hybrid statistical method. In *Proc. of ACOUSTICS*. Australian Acoustical Society.

DUAN, F. & WANG, J. 2021 Fluid–structure–sound interaction in noise reduction of a circular cylinder with flexible splitter plate. *J. Fluid Mech.* **920**, A6.

EPPS, B.P. & TECHET, A.H. 2010 An error threshold criterion for singular value decomposition modes extracted from PIV data. *Exp. Fluids* **48** (2), 355–367.

ETKIN, B., KORBACHER, G.K. & KEEFE, R.T. 1956 Acoustic radiation from a stationary cylinder in a fluid stream. *J. Acoust. Soc. Am.* **28** (4), 776–776.

ETKIN, B., KORBACHER, G.K. & KEEFE, R.T. 1957 Acoustic radiation from a stationary cylinder in a fluid stream (Aeolian tones). *J. Acoust. Soc. Am.* **29** (1), 30–36.

FAGE, A. & FALKNER, V.M. 1931 Further experiments on the flow around a circular cylinder. *Tech. Rep.* HM Stationery Office.

FARGE, M. 1992 Wavelet transforms and their applications to turbulence. *Annu. Rev. Fluid Mech.* **24** (1), 395–458.

FENG, L.H. & WANG, J.J. 2010 Circular cylinder vortex-synchronization control with a synthetic jet positioned at the rear stagnation point. *J. Fluid Mech.* **662**, 232–259.

FENG, L.-H., WANG, J.-J. & PAN, C. 2011 Proper orthogonal decomposition analysis of vortex dynamics of a circular cylinder under synthetic jet control. *Phys. Fluids* **23** (1), 014106.

FERGUSON, N. & PARKINSON, G.V. 1967 Surface and wake flow phenomena of the vortex-excited oscillation of a circular cylinder. *J. Eng. Ind.* **89** 831–838.

FFOWCS WILLIAMS, J.E. & HALL, L.H. 1970 Aerodynamic sound generation by turbulent flow in the vicinity of a scattering half plane. *J. Fluid Mech.* **40** (4), 657–670.

FRANSSON, J.H.M., KONIECZNY, P. & ALFREDSSON, P.H. 2004 Flow around a porous cylinder subject to continuous suction or blowing. *J. Fluids Struct.* **19** (8), 1031–1048.

GAO, D., CHEN, G., CHEN, W., HUANG, Y. & LI, H. 2019 Active control of circular cylinder flow with windward suction and leeward blowing. *Exp. Fluids* **60** (2), 26.

GAO, D., MENG, H., HUANG, Y., CHEN, G. & CHEN, W.-L. 2021 Active flow control of the dynamic wake behind a square cylinder using combined jets at the front and rear stagnation points. *Phys. Fluids* **33** (4), 047101.

GARCIA-SAGRADO, A. & HYNES, T. 2011 Stochastic estimation of flow near the trailing edge of a NACA0012 airfoil. *Exp. Fluids* **51** (4), 1057–1071.

GERRARD, J.H. 1955 Measurements of the sound from circular cylinders in an air stream. *Proc. Phys. Soc.* B **68** (7), 453.

GERRARD, J.H. 1961 An experimental investigation of the oscillating lift and drag of a circular cylinder shedding turbulent vortices. *J. Fluid Mech.* **11** (2), 244–256.

GERRARD, J.H. 1966 The mechanics of the formation region of vortices behind bluff bodies. *J. Fluid Mech.* **25** (2), 401–413.

GRECO, C.S., PAOLILLO, G., ASTARITA, T. & CARDONE, G. 2020 The von Kármán street behind a circular cylinder: flow control through synthetic jet placed at the rear stagnation point. *J. Fluid Mech.* **901**, A39.

GRUBER, M. 2012 Airfoil noise reduction by edge treatments. PhD thesis, University of Southampton.

GUO, J., MARYAMI, R., YANG, C., YANG, Y., WANG, X. & LIU, Y. 2023 Aerodynamic noise reduction of a blunt flat plate by trailing-edge blowing. *Phys. Fluids* **35** (6), 065116.

GUO, M., WANG, Z., YU, H. & GAO, D. 2022 Wake control of a bluff-body via distributed jets over its surface. *AIP Adv.* **12** (6), 065025.

HARTWICH, P.M., DICKEY, E.D., SCLAFANI, A.J., CAMACHO, P., GONZALES, A.B., LAWSON, E.L., MAIRS, R.Y. & SHMILOVICH, A. 2014 *AFC-Enabled Simplified High-Lift System Integration Study*. National Aeronautics and Space Administration, Langley Research Center.

HE, G.S., LI, N. & WANG, J.J. 2014 Drag reduction of square cylinders with cut-corners at the front edges. *Exp. Fluids* **55**, 1–11.

HEIDARI, M. 2016 Wake characteristics of single and tandem emergent cylinders in shallow open channel flow. PhD thesis, University of Windsor (Canada).

HENNING, A., KAEPERNICK, K., EHRENFRIED, K., KOOP, L. & DILLMANN, A. 2008 Investigation of aeroacoustic noise generation by simultaneous particle image velocimetry and microphone measurements. *Exp. Fluids* **45** (6), 1073.

HUSSAIN, A.K.M.F. 1983 Coherent structures—reality and myth. *Phys. Fluids* **26** (10), 2816–2850.

INOUE, O. & HATAKEYAMA, N. 2002 Sound generation by a two-dimensional circular cylinder in a uniform flow. *J. Fluid Mech.* **471**, 285–314.

VON KÁRMÁN, T. 1912 Uber den mechanismus des flussigkeits-und luftwiderstandes. *Phys. Z.*, 49–59.

KIM, J. & CHOI, H. 2005 Distributed forcing of flow over a circular cylinder. *Phys. Fluids* **17** (3), 033103.

KIRBY, M., BORIS, J. & SIROVICH, L. 1990 An eigenfunction analysis of axisymmetric jet flow. *J. Comput. Phys.* **90** (1), 98–122.

LI, H. & NOZAKI, T. 1995 Wavelet analysis for the plane turbulent jet: analysis of large eddy structure. *JSME Intl J.* B **38** (4), 525–531.

LI, S., RIVAL, D.E. & WU, X. 2021 Sound source and pseudo-sound in the near field of a circular cylinder in subsonic conditions. *J. Fluid Mech.* **919**, A43.

LIN, J.C., TOWFIGHI, J. & ROCKWELL, D. 1995 Near-wake of a circular cylinder: control, by steady and unsteady surface injection. *J. Fluids Struct.* **9** (6), 659–669.

MALLAT, S. 1999 *A Wavelet Tour of Signal Processing*. Elsevier.

MARYAMI, R. & ALI, S.A.S. 2023 Near-field pressure and wake velocity coherence of a circular cylinder. *Phys. Fluids* **35** (11), 115140.

MARYAMI, R., ALI, S.A.S., AZARPEYVAND, M., DEHGHAN, A.A. & AFSHARI, A. 2022*a* The influence of cylinders in tandem arrangement on unsteady aerodynamic loads. *Expl Therm. Fluid Sci.* **139**, 110709.

MARYAMI, R., ARCONDOULIS, E. & LIU, Y. 2023*a* Aeroacoustic investigation of active base blowing applied to a structured porous cylinder. In *AIAA AVIATION 2023 Forum*, p. 3741. AIAA.

MARYAMI, R., ARCONDOULIS, E. & LIU, Y. 2023*b* Experimental investigation of local blowing for noise and flow control of a circular cylinder. In *AIAA AVIATION 2023 Forum*, p. 3742. AIAA.

MARYAMI, R., ARCONDOULIS, E.J.G., LIU, Q. & LIU, Y. 2023*c* Experimental near-field analysis for flow induced noise of a structured porous-coated cylinder. *J. Sound Vib.* **551**, 117611.

MARYAMI, R., ARCONDOULIS, E.J.G., YANG, C. & LIU, Y. 2023*d* Relationship between vortex shedding noise and remotely-sensed surface pressure fluctuations of a structured porous-coated cylinder. In *INTER-NOISE and NOISE-CON Congress and Conference Proceedings*, vol. 265, pp. 515–526. Institute of Noise Control Engineering.

MARYAMI, R., ARCONDOULIS, E., YANG, C., SZOKE, M., XIANG, Z., GUO, J., WEI, R. & LIU, Y. 2022*b* Application of local blowing to a structured porous-coated cylinder for flow and noise control. In *28th AIAA/CEAS Aeroacoustics 2022 Conference*, p. 2921. AIAA.

MARYAMI, R., AZARPEYVAND, M., DEHGHAN, A.A. & AFSHARI, A. 2019 An experimental investigation of the surface pressure fluctuations for round cylinders. *Trans. ASME J. Fluids Engng* **141** (6), 061203.

MARYAMI, R., SHOWKAT ALI, S.A., AZARPEYVAND, M. & AFSHARI, A. 2020 Turbulent flow interaction with a circular cylinder. *Phys. Fluids* **32** (1), 015105.

MATHELIN, L., BATAILLE, F. & LALLEMAND, A. 2002 The effect of uniform blowing on the flow past a circular cylinder. *Trans. ASME J. Fluids Engng* **124** (2), 452–464.

MISH, P.F. 2001 Mean loading and turbulence scale effects on the surface pressure fluctuations occurring on a NACA 0015 airfoil immersed in grid generated turbulence. PhD thesis, Virginia Tech.

NISHIOKA, M. & SATO, H. 1978 Mechanism of determination of the shedding frequency of vortices behind a cylinder at low Reynolds numbers. *J. Fluid Mech.* **89** (1), 49–60.

NORBERG, C. 1986 Interaction between freestream turbulence and vortex shedding for a single tube in cross-flow. *J. Wind Engng Ind. Aerodyn.* **23**, 501–514.

NORBERG, C. 1987 Effects of Reynolds number and a low-intensity freestream turbulence on the flow around a circular cylinder. Thesis, Chalmers University, Goteborg, Sweden, *Technological Publications* **87** (2), 1–55.

NORBERG, C. 2003 Fluctuating lift on a circular cylinder: review and new measurements. *J. Fluids Struct.* **17** (1), 57–96.

OCTAVIANTY, R. & ASAI, M. 2016 Effects of short splitter plates on vortex shedding and sound generation in flow past two side-by-side square cylinders. *Exp. Fluids* **57**, 1–13.

OGUMA, Y., YAMAGATA, T. & FUJISAWA, N. 2013 Measurement of sound source distribution around a circular cylinder in a uniform flow by combined particle image velocimetry and microphone technique. *J. Wind Engng Ind. Aerodyn.* **118**, 1–11.

VAN OUDHEUSDEN, B.W., SCARANO, F., VAN HINSBERG, N.P. & WATT, D.W. 2005 Phase-resolved characterization of vortex shedding in the near wake of a square-section cylinder at incidence. *Exp. Fluids* **39**, 86–98.

PARK, D.S., LADD, D.M. & HENDRICKS, E.W. 1994 Feedback control of von Kármán vortex shedding behind a circular cylinder at low Reynolds numbers. *Phys. Fluids* **6** (7), 2390–2405.

PERRIN, R., BRAZA, M., CID, E., CAZIN, S., BARTHET, A., SEVRAIN, A., MOCKETT, C. & THIELE, F. 2007 Obtaining phase averaged turbulence properties in the near wake of a circular cylinder at high Reynolds number using pod. *Exp. Fluids* **43**, 341–355.

PORTELA, F.A., PAPADAKIS, G. & VASSILICOS, J.C. 2018 Turbulence dissipation and the role of coherent structures in the near wake of a square prism. *Phys. Rev. Fluids* **3** (12), 124609.

PORTELA, F.A., PAPADAKIS, G. & VASSILICOS, J.C. 2020 The role of coherent structures and inhomogeneity in near-field interscale turbulent energy transfers. *J. Fluid Mech.* **896**, A16.

POSDZIECH, O. & GRUNDMANN, R. 2007 A systematic approach to the numerical calculation of fundamental quantities of the two-dimensional flow over a circular cylinder. *J. Fluids Struct.* **23** (3), 479–499.

PROVANSAL, M., MATHIS, C. & BOYER, L. 1987 Bénard-von Kármán instability: transient and forced regimes. *J. Fluid Mech.* **182**, 1–22.

QIN, L. 2004 Development of reduced-order models for lift and drag on oscillating cylinders with higher-order spectral moments. PhD thesis, Virginia Tech.

QU, Y., WANG, J., SUN, M., FENG, L., PAN, C., GAO, Q. & HE, G. 2017 Wake vortex evolution of square cylinder with a slot synthetic jet positioned at the rear surface. *J. Fluid Mech.* **812**, 940–965.

RASHIDI, S., HAYATDAVOODI, M. & ESFAHANI, J.A. 2016 Vortex shedding suppression and wake control: a review. *Ocean Engng* **126**, 57–80.

ROSHKO, A. 1955 On the wake and drag of bluff bodies. *J. Aeronaut. Sci.* **22** (2), 124–132.

SADEH, W.Z. & SAHARON, D.B. 1982 Turbulence effect on crossflow around a circular cylinder at subcritical Reynolds numbers. *Tech. Rep.* NASA.

SCHÄFER, F., BREUER, M. & DURST, F. 2009 The dynamics of the transitional flow over a backward-facing step. *J. Fluid Mech.* **623**, 85–119.

SCHLICHTING, H. & GERSTEN, K. 2003 *Boundary-Layer Theory*. Springer Science & Business Media.

SHARMA, K.R. & DUTTA, S. 2020 Flow control over a square cylinder using attached rigid and flexible splitter plate at intermediate flow regime. *Phys. Fluids* **32** (1), 014104.

SHOWKAT ALI, S.A., MAHDI, A. & DA SILVA, C.R.I. 2018 Trailing-edge flow and noise control using porous treatments. *J. Fluid Mech.* **850**, 83–119.

SHOWKAT ALI, S.A., MAHDI, A. & DA SILVA, C.R.I. 2020 Trailing edge bluntness noise reduction using porous treatments. *J. Sound Vib.* **474**, 115257.

SIROVICH, L. 1987 Turbulence and the dynamics of coherent structures. Parts I, II and III. *Q. Appl. Maths* **45**, 561–590.

SREENIVASAN, K.R., STRYKOWSKI, P.J. & OLINGER, D.J. 1987 Hopf bifurcation, Landau equation, and vortex shedding behind circular cylinders. In *Forum on Unsteady Flow Separation*, vol. 1, pp. 1–13. ASME.

STROUHAL, V. 1878 *Über eine besondere Art der Tonerregung*. Stahel.

SUEKI, T., TAKAISHI, T., IKEDA, M. & ARAI, N. 2010 Application of porous material to reduce aerodynamic sound from bluff bodies. *Fluid Dyn. Res.* **42** (1), 015004.

SUZUKI, T. & COLONIUS, T. 2006 Instability waves in a subsonic round jet detected using a near-field phased microphone array. *J. Fluid Mech.* **565**, 197–226.

UNAL, M.F. & ROCKWELL, D. 1988 On vortex formation from a cylinder. Part 1. The initial instability. *J. Fluid Mech.* **190**, 491–512.

VEMURI, S.H.S., LIU, X., ZANG, B. & AZARPEYVAND, M. 2020 On the use of leading-edge serrations for noise control in a tandem airfoil configuration. *Phys. Fluids* **32** (7), 077102.

WILLIAMS, D.R. & AMATO, C.W. 1989 Unsteady pulsing of cylinder wakes. In *Frontiers in Experimental Fluid Mechanics*, pp. 337–364. Springer.

WILLIAMS, D.R., MANSY, H. & AMATO, C. 1992 The response and symmetry properties of a cylinder wake subjected to localized surface excitation. *J. Fluid Mech.* **234**, 71–96.

WILLIAMSON, C.H.K. 1996 Vortex dynamics in the cylinder wake. *Annu. Rev. Fluid Mech.* **28** (1), 477–539.

WONG, H.Y. 1985 Wake flow stabilization by the action of base bleed. *J. Fluids Eng.* **107** (3), 378–384.

WOOD, C.J. 1964 The effect of base bleed on a periodic wake. *Aeronaut. J.* **68** (643), 477–482.

WOOD, C.J. 1967 Visualization of an incompressible wake with base bleed. *J. Fluid Mech.* **29** (2), 259–272.

WU, Z. & CHOI, H. 2021 Modification of flow behind a circular cylinder by steady and time-periodic blowing. *Phys. Fluids* **33** (11), 115126.

YANG, Y., LIU, Y., LIU, R., SHEN, C., ZHANG, P., WEI, R., LIU, X. & XU, P. 2021 Design, validation, and benchmark tests of the aeroacoustic wind tunnel in sustech. *Appl. Acoust.* **175**, 107847.

ZDRAVKOVICH, M.M. 1981 Review and classification of various aerodynamic and hydrodynamic means for suppressing vortex shedding. *J. Wind Engng Ind. Aerodyn.* **7** (2), 145–189.

ZHOU, Y. & ANTONIA, R.A. 1992 Convection velocity measurements in a cylinder wake. *Exp. Fluids* **13** (1), 63–70.